EXPERIMENTAL AND MODELING INVESTIGATION OF MEMBRANE REACTOR SYSTEMS FOR PROPANE DEHYDROGENATION

A Thesis
Presented to
The Academic Faculty

by

Seung-Won Choi

In Partial Fulfillment
of the Requirements for the Degree
Doctor of Philosophy in Chemical Engineering
in the School of Chemical & Biomolecular Engineering

Georgia Institute of Technology
August 2016

EXPERIMENTAL AND MODELING INVESTIGATION OF MEMBRANE REACTOR SYSTEMS FOR PROPANE DEHYDROGENATION

Approved by:

Dr. Sankar Nair, Advisor
School of Chemical & Biomolecular Engineering
Georgia Institute of Technology

Dr. Christopher W. Jones, Co-Advisor
School of Chemical & Biomolecular Engineering
Georgia Institute of Technology

Dr. David S. Sholl, Co-Advisor
School of Chemical & Biomolecular Engineering
Georgia Institute of Technology

Dr. Yoshiaki Kawajiri
School of Chemical & Biomolecular Engineering
Georgia Institute of Technology

Dr. Andrei G. Fedorov
School of Mechanical Engineering
Georgia Institute of Technology

Date Approved: April 29th , 2016

To my lovely wife, Jungmin

ACKNOWLEDGEMENTS

I would like to express my special appreciation and thanks to my advisor Prof. Sankar Nair for the continuous support of my PhD study and related research, for his patience, motivation, and immense knowledge. I also would like to express my sincere gratitude to my co-advisors Prof. Christopher Jones and David Sholl. Their guidance helped me in all the time of research and writing of this thesis, which incented me to widen my research from various perspectives. I could not have imagined having better advisors and mentors for my PhD study. Besides my advisor, I would like to thank the thesis committee Prof. Andrei Fedorov and Prof. Yoshiaki Kawajiri for their insightful comments and encouragement

I want to thank all of the previous and current group members in the three research groups, for the stimulating discussions, for the project we were working together. I am also very grateful to the many friends in the ChBE Korean Student Association and for all the fun we have had in the last five years.

My sincere thanks also go to my family. Words cannot express how grateful I am to my parents and parents-in-law for all of the supports that they have made on my behalf. I would also like to thank all of my friends who supported me in writing, and incented me to strive towards my goal.

At the end I would like express appreciation to my beloved wife Jungmin for her love, understanding and standing beside me throughout my PhD study.

TABLE OF CONTENTS

LIST OF TABLES

LIST OF FIGURES

SUMMARY

The intensification of paraffin dehydrogenation processes is of increasing importance in the production of olefins, which are important petrochemical feedstocks. In this thesis, I conduct a detailed investigation of membrane reactors for propane dehydrogenation (PDH). PDH is an equilibrium limited endothermic reaction, requiring a high energy supply to the reactor as well as energy-intensive downstream separations of propylene from propane. The membrane reactor is an integrated unit operation combining reactions and membrane permeation, which leads to overcoming the thermodynamic limitations that exist in a conventional PDH reactor. The overall goal is the development and detailed study of PDH reactions in membrane reactor system from both modeling and experimental approaches, which ultimately allows high propane conversion and propylene selectivity for PDH application. I built a detailed model of the packed bed membrane reactor (PBMR) which allowed us to explore the useful operating condition windows for the PBMR and assess the effects of different physical and chemical parameters on PDH conversion and selectivity. These investigations enable us to pursue integration of our experimental data on PDH catalyst kinetics and zeolite membrane transport with our detailed PBMR model incorporating downstream separation.

Chapter 1 presents an introductory discussion of key issues in the development of membrane reactors for PDH, which set the stage for this work. In Chapter 2, the concept of packed bed membrane reactors (PBMRs) using zeolite membranes is studied. Among

several different types of membrane reactors, the PBMR configuration is determined to be the most effective configuration for the PDH process considering the feasibility of membrane fabrication. I carried out modeling studies of PBMR using a 1D isothermal assumption for a lab scale reactor with a range of physically realistic values for the fundamental transport and reaction parameters of the membrane and the catalyst. For the use of accurate kinetic and transport parameters in the model, membrane permeance data and kinetic parameters for a commercially available catalyst (Cr_2O_3 on Al_2O_3 support) were obtained. I apply several kinetic models, based on different rate determining step assumptions in the PDH reaction mechanism on the catalytic surface. The kinetic parameters for thermal cracking reactions were also obtained and used to see their contribution in PBMR operation. The modeling results were validated using membrane reactor experimental data.

A modeling-based approach to understand physically realistic and technologically interesting material properties and operating configurations of PBMRs for PDH is then presented in Chapter 3. I consider PBMRs composed of microporous or mesoporous membranes combined with a PDH catalyst. The influence of reaction and membrane transport parameters is investigated, as well as operating parameters such as sweep flow rates, countercurrent vs cocurrent sweep gas operation, and shell-side catalyst placement, to determine desired 'operating windows' for isothermal and non-isothermal operation. Higher Damköhler (*Da*) and lower Péclet (*Pe*) numbers are generally helpful, but are much more beneficial with highly H_2-selective membranes rather than higher-flux, lower-selectivity membranes. The required ranges of PBMR operating conditions, and the MR

performance, vary depending on the type of membrane. Although small-pore membranes (hydrogen selective) lead to the best performance, the H_2-selective membranes show a plateau region of conversion. Therefore H_2-selective PBMRs will greatly benefit from the fabrication of thin (~1 μm or less) membranes for a large membrane permeance. The medium-pore zeolite and Knudsen selective membranes show a limited ranged of useful operating conditions since they allow propane (reactant) permeation, thus unfavorably shifting equilibrium to the reactant side. The use of low selectivity membranes show a complex trade-off between kinetics and permeation, and are effective only in a limited window. The operating windows in non-isothermal conditions show a shift of conversion to lower values, however, the general trends of PBMR performance remain the same.

In Chapter 4, I describe a detailed ASPEN-FORTRAN simulation based on a 2D non-isothermal model for design of a PDH plant. This model included detailed PBMR operating configurations such as use of multiple membrane tubes and inter-stage heaters for both non-recycled and recycled system. In order to find better PBMR operating configurations, the required number of membrane tubes and operating conditions are considered for a target propylene production capacity. I consider hollow fiber membranes in the PBMR configuration and compare PDH performance with the use of conventional ceramic supports and PBR configurations. Total PBMR volumes are calculated based on the packing density of membranes for a target propylene production rate. The required energy for the C_3 splitter and sweep gas separation is then investigated. The study includes comparison of two recycling configurations; simple recycling of feed and sweep gas streams and product removal at each reactor stage. Considering the trade-off between

enhanced PBMR performance and additional energy from sweep gas stream, the model suggests that an ideal PBMR sweep/feed ratio should exist for lower energy consumption.

The remaining objective of this thesis is to provide some new insights into the catalysts used in PDH. Towards this end, the behavior of gallosilicate MFI catalysts synthesized in the presence of 3-mercaptopropyl-trimethoxysilane (MPS) functional silane is investigated in Chapter 5. The Si species in MPS is expected to be incorporated into the zeolite framework by hydrolysis of the trimethoxy group while the thiol group interacts with metallic ions in the zeolite synthesis solution, thereby facilitating the metal sites incorporating into the zeolite pores. Therefore MPS addition to the zeolite synthesis gel results in gallosilicate molecular sieves with reduced Brønsted acidity and enhanced Lewis acidity, as evinced by combined NH_3 temperature-programmed desorption (TPD), isopropylamine (IPA) TPD and IR analysis of pyridine-loaded catalysts. In particular, the gallosilicate MFI catalysts prepared using MPS provide a significant concentration of strong Lewis acid sites, which are important in controlling the selectivity of PDH. Enhanced PDH performance with high propylene selectivities at elevated conversions with concomitant high propane conversion rates with limited cracking and aromatization products are obtained from the catalysts synthesized with MPS. The gallosilicate MFI materials prepared using MPS are compared with the benchmark chromia-alumina catalyst, and the gallosilicate materials show less deactivation but slightly lower propylene selectivity. Chapter 6 presents the main conclusions from this work and discusses avenues for further research that advances the PBMR concept in dehydrogenation processes.

CHAPTER 1: INTRODUCTION

1.1. Propane dehydrogenation

Propylene is an important feedstock in the petrochemical industry for the production of chemical products such as poly(propylene), acrylonitrile, and 2-propanol. Although propylene can be produced from steam cracking of naphtha, there is a growing attention paid to propane dehydrogenation (PDH) [1-5], especially in North America and the Middle East due to their abundant supply of propane. The production of propylene from catalytic dehydrogenation of propane (PDH) has been commercially applied using two well-known processes, namely the Catofin process from CB&I Lummus [6-11] and the Oleflex process from UOP [12-18]. The Catofin process uses a Cr-based catalyst in multiple parallel fixed bed reactors, while the Oleflex process is based on a Pt-based catalyst in a fluidized bed reactor [19, 20].

In current industrial processes, the PDH catalyst undergoes rapid deactivation due to coke formation on the catalytic surface, and there are now renewed efforts being made at discovering new PDH catalysts or improving the stability, activity, and selectivity of known PDH catalysts. The time on stream data of PDH conversion in **Fig. 1-1** was obtained in a fixed bed reactor using Cr_2O_3 catalyst on Al_2O_3 support, which displays typical deactivation behavior, and the coke deposit was observed after PDH reaction. The coke should be removed before the catalyst becomes more deactivated, generally by oxidation of the coke, which requires the regeneration process runs very short cycle. For

example, the Catofin process applies a cycle of 12 min of dehydrogenation, 3 min of inert gas purging, and 12 min of regeneration in the multiple parallel fixed bed reactors [6]. The Oleflex process runs a continuous catalyst regeneration unit (CCR) for burning off the coke and reducing the Pt catalyst in moving bed catalyst circulating the PDH reactors and regenerator [13]. PDH itself is also very energy intensive due to its highly endothermic nature, and the conversion is thermodynamically limited. The temperature dependent equilibrium conversion of PDH and adiabatic operating line are shown in **Fig. 1-2**. The equilibrium conversion is estimated via an empirical equation in Li et al [21]. The endothermic PDH reaction causes significant temperature drop and therefore the temperature drop should be compensated by reheating the outlet streams at inter-stage heaters as described in dashed line in **Fig. 1-2**. However, the equilibrium limited nature of PDH does not allow achieving the conversion above the thermodynamic equilibrium line in **Fig. 1-2**. Furthermore, the downstream separation of propylene from its equilibrium mixture with propane is also highly energy intensive because of the small relative volatility between the two. The separation is currently accomplished in cryogenic or high-pressure distillation columns with more than 100 trays [22-24].

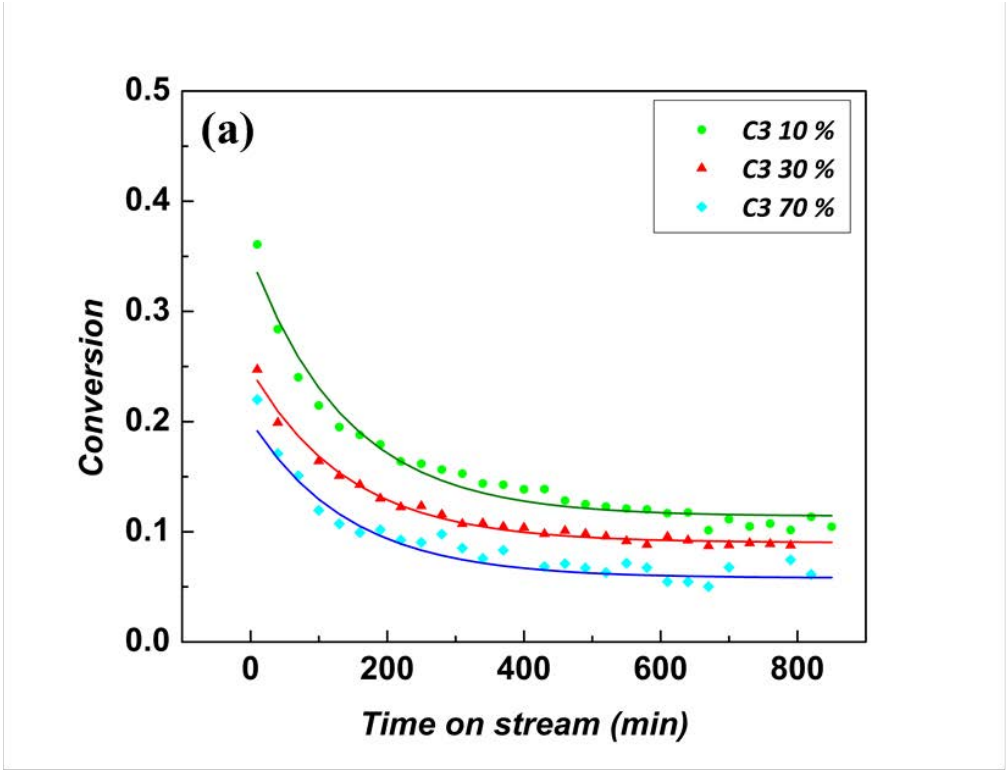

(b)

Fig. 1-1. (a) Example of time on stream data of PDH conversion. Schematic of a PDH PBMR. (b) coke deposition before (left) and after (right) PDH reaction. The PDH experiments were conducted at 600 °C and 1 atm (W/F = 0.3 g.s.cm^{-3}).

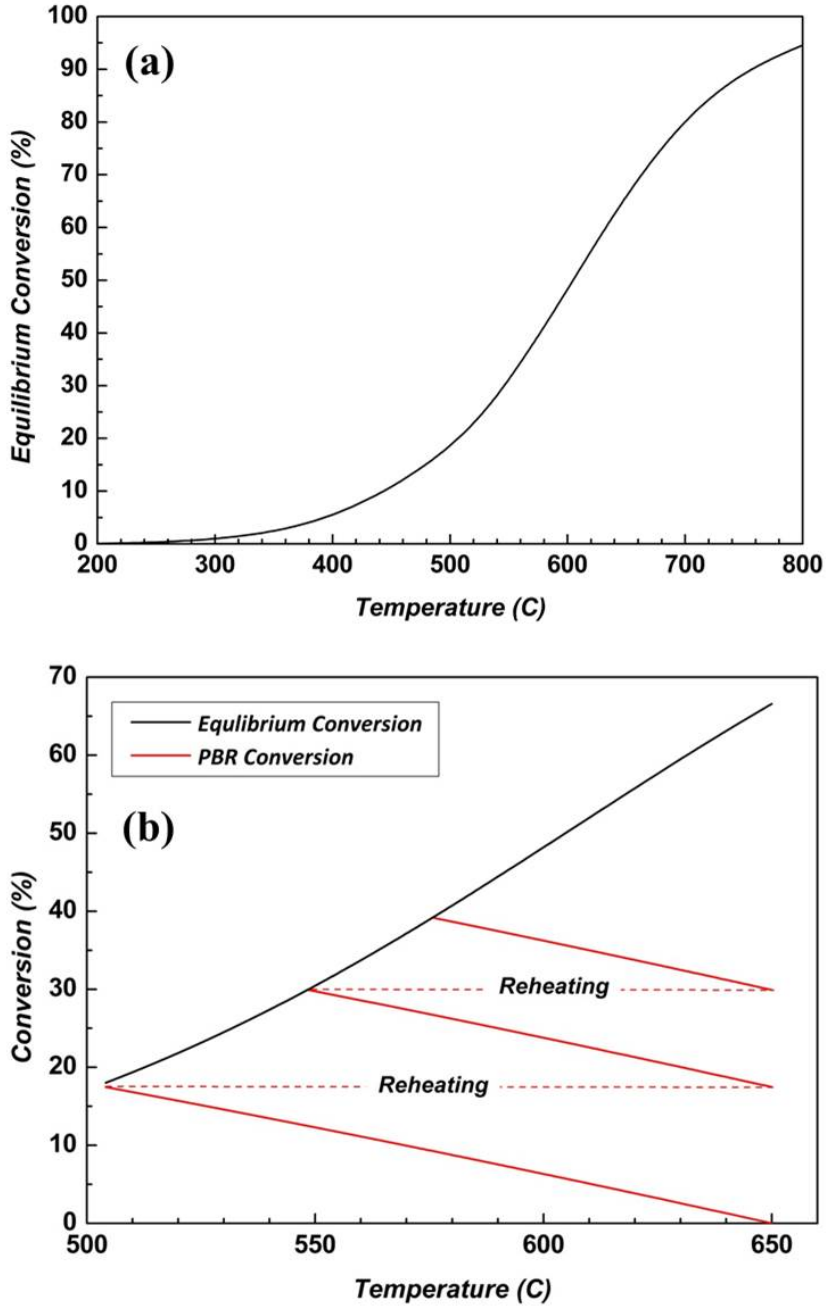

Fig. 1-2. (a) Equilibrium conversion of PDH with respect to temperature at 1 atm (b) adiabatic PDH operating line in packed bed reactor (PBR).

1.2. Membrane reactors and zeolite membranes

1.2.1. Concept of membrane reactors

One way to overcome the equilibrium limitations of reactions such as PDH is to intensify them *via* membrane reactors [25-27]. Different types of membrane reactors have been suggested based on the role of membranes such as contactor or distributor of reactants and product removal [27]. Catalytic membrane reactors (CMR) or integrated catalytic membrane reactors (ICMR) use a catalytic membrane which consists of catalytic active sites and perm-selective layer where it intensifies the process by combining reaction and separation. The catalytic active sites can be impregnated using post synthesis methods [28], the active layer can be coated on the membrane surface [29-32], or the membrane can be an inherently catalytic material [33]. A catalytic non-permselective membrane reactor (CNMR, or catalytic membrane contactor) applies catalytic membrane in the same configuration as ICMR, but the catalytic membrane acts as a contact layer for reactants ensuring stoichiometric feed rates from two different sides. Also, non-permselective membrane reactors (NPMR) were suggested, where the membrane does not have catalytic active layer nor permselectivity, but it acts as distributor of reactants [34].

Among different possible membrane reactor configurations, the packed bed membrane reactor (PBMR) has been most widely studied. It consists of packed bed catalysts in a conventional packed bed reactor (PBR) and a tubular membrane surrounding the catalysts as depicted in **Fig. 1-3**. The permselective membrane permeates one or more of the reaction products, thereby shifting the equilibrium to the product side. The enhancement of PDH conversion in PBMR configuration can also reduce the

separation cost of the downstream separation by increasing propylene production.

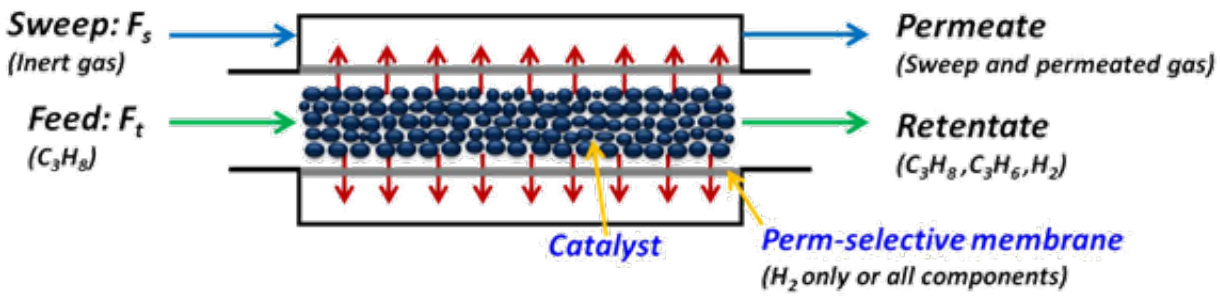

Fig. 1-3. Schematic of a PDH PBMR. The red arrows denote permeation through the membrane surrounding the packed bed.

The concept of membrane reactor has been applied by many research groups for the last two decades such as water gas shift (WGS) reaction[35-40] and alkane dehydrogenations [41-44]. The studies generally focus on making more H_2 selective membranes with large permeability to increase conversion. Kim et al. carried out experimental studies of zeolite MFI membrane reactors on high temperature WGS with various experimental conditions [35-37]. Recently Chein et al. investigated the effect of various sweep gas condition of membrane reactor for WGS [40]. The use of membrane reactors has been also extensively studied for dehydrogenation reactions. Studies on ethane dehydrogenation in membrane reactors were performed by Champagnie et al. using Pt-impregnated alumina ceramic membranes [41]. Kong et al. used pure-silica MFI zeolite membranes for dehydrogenation of ethyl benzene and investigated the effect of sweep gas on conversion enhancement [45]. Recently Van der Bergh et al. investigated

isobutene dehydrogenation in a DDR zeolite membrane reactor with both modeling and experimental approaches [44]. Steam reforming reactions in membrane reactor have been reported by many research groups in an effort to increase H_2 production [46-52]. Along with other dehydrogenation reaction, attention has been paid for the use of membrane reactors for PDH [53-62]. In early studies, Ziaka et al. applied ceramic membranes to enhance the PDH conversion and selectivity in a membrane reactor [53, 54]. Collins et al. also observed moderate improvements in PDH performance using hydrogen-selective palladium and silica membranes [55]. Other experimental approaches on PBMR for PDH were studied using silica [56, 57] and metallic Pd membranes [55, 61] while modeling studies with a various range of operating and membrane conditions were also reported [59, 60, 62].

In addition to experimental work, mathematical modeling of PBMRs has also been performed. Wu et al. built a model for dehydrogenation of ethyl benzene using a ceramic membrane with performance based on Knudsen diffusion [63]. Kumar et al. studied a membrane reactor for dehydrogenation of cyclohexane using FAU zeolite membranes for which the permeances were described by empirical equations as a function of temperature [64]. A relationship between membrane permeation and kinetic reaction rates has been suggested by Harold et al., who reported an optimal range of membrane permeation rates for different membrane selectivities to achieve maximum conversion in cyclohexane dehydrogenation [65]. Gokhale et al. have used dimensional analysis to study the effects of residence time and membrane selectivity for isobutane dehydrogenation [66]. More detailed 2D models and non-isothermal models have also been developed. Tsai et al. carried out non-isothermal modeling for partial oxidation of

methane and studied temperature profiles in adiabatic operating conditions [67]. Shelepova et al. developed a model of combined oxidation of hydrogen (exothermic) in the shell side with propane dehydrogenation (endothermic) in the tube [68]. Modeling studies along with experimental work for counter current sweep gas configuration were reported [40, 62, 69-73]. Although the counter current operation may increase the driving force for the product permeation, Choi et al. concluded that counter current operations are beneficial only in limited operating condition with low WHSV range [62].

1.2.2. Membranes for membrane reactors

The materials for membrane reactors ideally would have high permeability, selectivity, and high temperature stability. For the application of PDH in membrane reactors, mesoporous membranes having large pores (2 ~ 50 nm) with Knudsen selectivity may not be suitable due to large permeation of the reactant. Conventional polymeric membranes were reported for olefin/paraffin separation [74-76]. Despite their good processibility and low cost, their performance is limited due to poor chemical and mechanical stability, especially for high temperature operation. In order to overcome this limitation, inorganic membranes have been developed such as ceramic, metal and zeolite membranes [77].

Various types of ceramic membranes for propylene or hydrogen selective separation were reported using amorphous silica [78-81]. Stoitsas et al. prepared porous silica membranes modified with Ag^{+} impregnation for propane and propylene separation [79]. Tsuru et al. also reported Co-doped silica membranes and compared permeances between H_2 and water vapor at high temperature [80]. Khatib and Oyama reviewed silica membranes

supported on Vycor glass and alumina materials made by chemical vapor deposition method for H_2 separation [81]. However, the lack of hydrothermal stability at high temperature and low reproducibility are the main drawback of silica membranes and make the membranes less attractive in industrial application [77, 82]. Dense metal membranes have been reported, dominantly using Pd-based material for selective H_2 permeation [83-85] although the membranes have an issue with surface poisoning. In dense metal membranes the transport occurs via solution-diffusion mechanism where the H_2 is dissociated on the metal surface and hydrogen atom is adsorbed and diffused through the metallic layer, followed by reformation and desorption of H_2 molecules on the other side [77]. In many case, Pd alloy can be more attractive than pure Pd in terms of hydrogen permeability and thermal stability, e.g. Pd-Ag membranes [85].

One of the promising candidates is zeolite membranes, which have well defined crystal pore structures and for which membrane fabrication processes are now available. The use of hydrogen-selective [37, 38] and propylene-selective zeolite membranes [86-89] were studied, and these can be considered to be applied in membrane reactors for propane dehydrogenation. Zeolite membranes can be prepared by synthesizing zeolite layers on a support [90]. The support materials should be mechanically stable such as ceramic, glass or metal whereas the zeolite layer provides selective properties for intended molecules. Two types of membranes can be considered for PDH PBMR, namely small-pore zeolite membranes and medium-pore zeolite membranes. Small-pore zeolite membranes are assumed to have negligible permeances of the olefin and paraffin. The silicoaluminophosphate zeolite SAPO-34 (~0.38 nm pore size) is one example of a material with these properties [27]. Medium-pore zeolite membranes also allow propane

and propylene to permeate, and are exemplified by MFI (~0.55 nm pore size) membranes [27].

MFI type membranes can be considered as a catalytic membrane for an ICMR. The structure of MFI is shown in **Fig. 1-4a**. It allows a membrane with wide range of Si/Al ratios and has a possibility of introduction of heteroatom sites such as Ga and In into its framework, thus is amenable to modification by catalytic sites [91-93]. However, when it comes to a PBMR type membrane reactor, which requires highly propylene or hydrogen selective membranes, MFI will not be the best selection for PDH because it also permeates the reactant. In other words, the pores of MFI are relatively large and may not be able to offer propylene selective property. Another candidate material is SAPO-34, which has the chabazite (CHA) framework type depicted in **Fig. 1-4b** with a small pore size (~0.38 nm). It was studied for the use of hydrogen purification such that it separates CO_2 from CO_2/H_2 mixtures and removes H_2 from CH_4/H_2 mixtures [94, 95]. Agrawal et al. showed that SAPO-34 has potential for propane and propylene separation [96], but their experiments were carried out at relatively low temperature (50 °C) where different adsorption properties can be used. At lower temperature, adsorption of propylene on zeolite channel can be more than propane, and thus leading to more surface diffusion of propylene [97-101]. On the other hand, at high temperature like 600 °C, the molecular sieve is a dominant factor. Considering the similar size of propane and propylene, both propane and propylene permeations are expected to be lower. Hence SAPO-34 can be considered as a H_2 selective membrane rather than a propylene selective one. It is a strong candidate material since it only allows small amount of propane reactant compared with MFI type membranes.

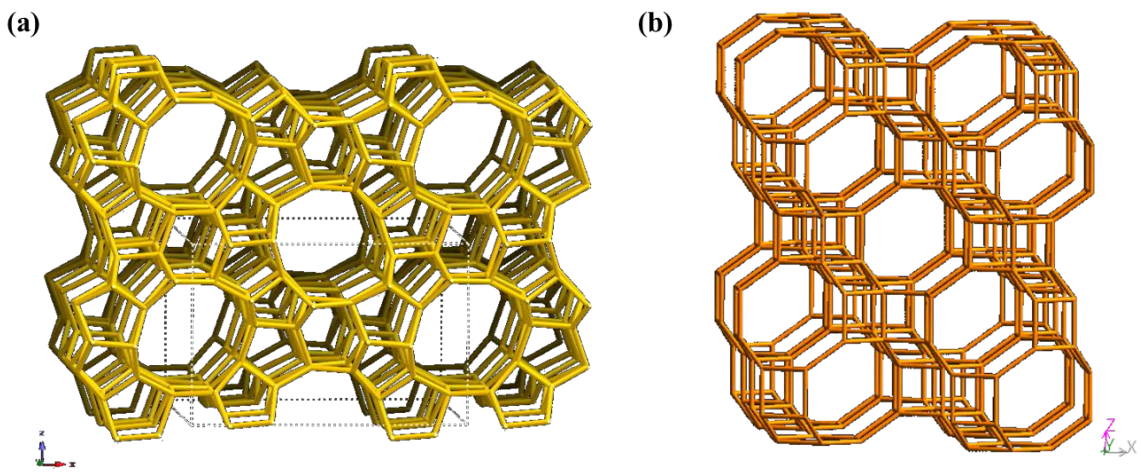

Fig. 1-4. Zeolite structures of (a) MFI and (b) CHA (SAPO-34) [102].

1.2.3. Transport in zeolite membranes

Depending on the membrane pore size, one of the three specific types of diffusion mechanisms - bulk, Knudsen or surface diffusion - describes diffusion in membrane pores [103]. Bulk and Knudsen diffusion usually occur together in membranes with larger pore sizes (about 50-200 nm), wherein both molecule-molecule and molecule-wall collisions are significant. Surface diffusion occurs by the adsorption and diffusion (hopping) of molecules from one site to another in micropores. The driving force for such mass transfer in surface diffusion is the surface coverage gradient of adsorbed molecules [104]. Therefore when the surface diffusion mechanism is considered, adsorption behavior of gas on the pore surface should be taken into a consideration as well as its diffusivity in order to understand permeation through a micoporous membrane.

There is very limited experimental permeation data that can be used to estimate transport in zeolite membranes for PBMRs and ICMRs [64, 105], and the use of detailed models can provide much better predictions. A full description of multicomponent mass transfer can be given based on the Maxwell-Stefan equations and the Langmuir adsorption model [103]. Krishna et al. employed the Maxwell-Stefan equations to model transport processes in membranes [106]. The generalized Maxwell-Stefan equations are

$$(J) = -\rho\left[q_{sat}\right]\left[B\right]^{-1}\left[\Gamma\right]\frac{\partial(\theta)}{\partial x} \tag{1-1}$$

$$\left[\begin{array}{l} B_{ii} = \dfrac{1}{Đ_i} + \sum_{\substack{j=1 \\ j\neq i}}^{n} \dfrac{\theta_j}{Đ_{ij}},\ B_{ij} = -\dfrac{\theta_i}{Đ_{ij}} \\ \\ \Gamma_{ij} = \theta_i \dfrac{\partial \ln p_i}{\partial \theta_j} = \delta_{ij} + \dfrac{\theta_i}{1-\sum \theta_i},\ Đ_{ij} = Đ_i^{\frac{\theta_i}{\theta_i+\theta_j}} Đ_j^{\frac{\theta_j}{\theta_i+\theta_j}} \end{array}\right] \tag{1-2}$$

Here, the terms in square brackets represent $n \times n$ matrices for a mixture of n components. The transport behavior is affected by both diffusivity ($Đ$) and surface coverage (θ, affected by adsorption) as considered in the form of [B] and [Γ] matrices. Multicomponent effects are reflected in non-zero off-diagonal terms in the matrices. Based on the generalized Maxwell-Stefan equations and experimental observations, Krishna and Kapteijn elucidated interesting differences between single and binary diffusion of hydrocarbons in MFI membranes [107-109]. For example, in single component permeation, hydrogen (which has larger diffusivity) permeates faster than *n*-butane, but *n*-butane shows faster binary permeation compared to hydrogen. Initially hydrogen diffuses faster, but as more strongly adsorbed *n*-butane molecules occupy the

adsorption sites, they block the permeation of hydrogen molecules [109].

The Maxwell-Stefan equation is a generalized form that can be applied for both single and multicomponent permeation. For single component (*n*=1), Eq. (1-1) can be reduced to

$$J_i = \frac{\rho q_{i,sat} Đ_i}{\delta} \ln \frac{1 + K_i P_{i,f}}{1 + K_i P_{i,p}} \tag{1-3}$$

Here, the zeolite density ρ (g.m^{-3}), saturation loading q (mol.g^{-1}), membrane thickness δ (m), Maxwell-Stefan diffusivity $Đ$ (m^2.s^{-1}), Langmuir parameter K (Pa^{-1}) and feed and permeate pressures (Pa) are used. This single Maxwell-Stefan equation can have further reduced forms, depending on the loading conditions of adsorbed molecules. At low loading conditions, which are observed for weakly adsorbed molecules or at high temperature, the permeated mole flux increases linearly with pressure. Then the flux becomes the same form as Fickian approach as a limiting case of Maxwell-Stefan equation (1-3):

$$J_i = \frac{\rho q_{i,sat} Đ_i}{\delta} K_i \Delta P \tag{1-4}$$

At high loading conditions such as low temperature, high pressure or strongly adsorbed molecules, the adsorption of the gas approaches its saturation level and the flux does not increase with pressure:

$$J_i = \frac{\rho q_{i,sat} Đ_i}{\delta} \Delta \ln P \tag{1-5}$$

As previously mentioned, surface diffusion is affected by the combined effects of adsorption and diffusivity. The effect of high temperature operation on transport in membranes should be considered in the PDH process, which is carried out at ~600°C. Since temperature affects both parameters, the temperature dependent permeation behavior can be predicted using the heat of adsorption and diffusion activation energy. The Kapteijn group carried out experiments and simulations to investigate temperature effects on MFI membrane permeation [110, 111]. At high loading, the temperature increase does not much decrease the loading, but increases the diffusivity. Hence at this condition, the permeation flux increases with increasing temperature due to increase in diffusivity. At low loading, on the other hand, the flux decreases with increasing temperature due to decrease in coverage, which is more significant than diffusivity increase [108, 110, 112]. In multi-component diffusion, both diffusivity and adsorption determine the selectivity. At low temperature, more strongly adsorbed component blocks the permeation of weakly adsorbed one. Kapteijn et al. reported the permeation flux of a mixture of hydrogen and n-butane through silicalite-1 membrane as a function of temperature [107]. In their work, weakly adsorbed hydrogen shows less permeation flux at low temperature but as temperature increases hydrogen which has higher diffusivity permeates more than n-butane. As temperature increases, all the components are more weakly adsorbed and eventually diffusion dominates the system, where the selectivity can be controlled by molecular sieving [107, 113]. In this regards, it is expected that the multicomponent diffusion and competitive adsorption effects become weak at high temperature operation of PDH in PBMR, and hence use of Fickian approach from single-gas permeances would provide a good estimate for the multicomponent permeation. In

particular for small pore zeolite such as SAPO-34 where H_2 permeation is dominant, this assumption is more valid.

1.3 Catalysts for propane dehydrogenation

1.3.1. Metal oxide catalysts

The main challenge in propane dehydrogenation catalysis is to reduce side products and coke formation, thus increasing the propylene selectivity. Many studies have focused on Pt-based catalysts [4, 5, 14, 15, 21, 114], which are already applied in Oleflex process. However, the deactivation/coking rate of Pt based catalysts is fast [16]. It is known that the presence of hydrogen [115, 116] or incorporation of alkali metals or modifying Pt with Sn are helpful to reduce coke formation [117]. Zhang et al. investigated the effect of Sn addition on Pt catalyst supported on ZSM-5 [14]. Li et al. carried out kinetic experiments and coke characterization using Pt-Sn/Al_2O_3 catalysts and reported a kinetic model [21]. Sun et al. also prepared Pt dispersed on an In containing hydrotalcite-like support (Pt/Mg(In)(Al)O) and reported that formation of Pt-In alloy reduced the coke deposition [17]. A few papers reported the use of In-based catalysts [72, 118]. Chen et al. examined In_2O_3/MO_x (M=Al,Si,Zr) for propane dehydrogenation in the presence of CO_2 and found that an alumina support provides the best dispersion of In_2O_3. Recently, Tan et al. prepared mixed In-Ga oxide and In-Ga-Al oxide and evaluated them as a new family of PDH catalysts [19, 119].

Cr-based catalysts were also reported and commercially used in Catofin process [2, 3, 7, 120]. Derossi et al. suggested that Cr^{3+} species are the active sites for dehydrogenation [3]. Gascon et al. provided a kinetic model for a Cr_2O_3/Al_2O_3 catalyst [7, 120]. The PDH reaction mechanism on Cr_2O_3 catalyst was already suggested and generally accepted [7, 121]. Based on the Langmuir-Hinshelwood mechanism as illustrated in **Fig. 1-5**, adsorption of a propane molecule on the catalytic surface is the first step, followed by dissociation of the propane molecule into intermediate C_3H_7 and H species. Then the intermediate species undergo further surface reaction, and the converted C_3H_6 and H_2 are desorbed. The possible rate determining step can be either the adsorption of propane on the surface or the surface reaction step. After neglecting the surface coverage of intermediate species (C_3H_7 and H), several kinetic models can be suggested based on the rate determining step. In order to determine the kinetic model, catalytic measurements should be conducted and kinetic parameters can be obtained by fitting the experimental data in each kinetic model, which will be more discussed in Chapter 2.

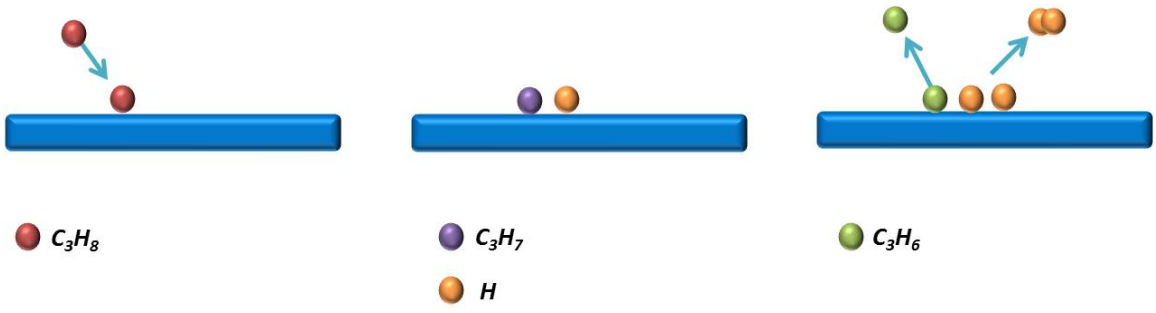

Fig. 1-5. Surface reaction mechanism of the PDH on Cr_2O_3 catalyst.

1.3.2. Propane conversion in Ga-containing MFI zeolite catalysts

Propane feedstocks can be also used in propane aromatization processes to produce benzene, toluene, and xylene. Ga-modified MFI zeolite catalysts have been commercialized and used in the UOP/BP Cyclar process for dehydrocyclization catalysis [122-128]. Ga containing zeolites synthesized by impregnation or ion-exchange into traditional, aluminum-containing HZSM-5 have been extensively studied [126-137]. Since Ga can be easily incorporated in the MFI framework, gallosilicate MFI can also be obtained by isomorphous substitution of Ga in the MFI zeolite framework [91, 92]. In an early report, Bayense et al. reported that the specific synthesis method used for Ga incorporation into HZSM-5 did not have much effect on the propane conversion, but incorporation of Ga increased the aromatic selectivity [130]. Also, the authors suggested that Ga loaded HZSM-5 was better for propane aromatization than the pure gallosilicate. However, other studies have reported that H-gallosilicate showed better performance than Ga ion-exchanged/impregnated HZSM-5 for propane aromatization [138-140].

Ga-containing zeolites can be prepared by impregnation or ion-exchange into HZSM-5 or isomorphous substitution of Ga in the MFI framework. In both cases, extra-framework Ga species are considered to be the main active sites for PDH[141-144]. However, direct characterization of these sites can be challenging. For instance, it is difficult to detect small amounts of extra-framework Ga species by Ga-NMR due to strong quadrupolar effects since the sites are mainly in low symmetry environments [145-148]. There have been several attempts to investigate the presence of extra-framework Ga species by acid site analysis using chemisorption techniques, which confirmed their strong Lewis acidic properties [128, 137, 149, 150]. Fourier transform infrared

spectroscopy (FT-IR) has also been used for characterization of acid sites in Ga-MFI [91, 93, 133, 137, 147, 151, 152]. Meriaudeau et al. utilized IR measurements of Ga/HZSM-5 samples with adsorbed pyridine and showed that the intensity of the band corresponding to Lewis acid sites (1450 cm^{-1}) was increased by addition of Ga [133]. Also, a decrease in the IR intensity at 1550 cm^{-1}, which is attributed to pyridinium ions at Brønsted acid sites, was observed with Ga impregnated HZSM-5. Otero Areán et al. studied the framework Ga bridged Brønsted group at 3617 cm^{-1} in the hydroxyl stretching region and showed decreased intensities of the peak with increased preheating temperatures [151]. Delgass et al. conducted IR measurements on Ga impregnated HZSM-5 whereby they observed decreased intensities of Brønsted acid sites with increased Ga loadings due to replacement of proton sites by Ga species[152]. Rodrigues et al. reported the presence of strong Lewis acid sites in Ga/HZSM-5 as evidenced by adsorbed pyridine that remained even at high temperatures (673 K) while almost no pyridine was left at the same temperature with HZSM-5 materials [137]. The authors suggested atomically dispersed oxidic Ga species in ion-exchange positions would be related to the strong Lewis acid sites.

A reaction mechanism of propane aromatization using Ga loaded HZSM-5 was suggested by Giannetto et al [142] as described in **Fig. 1-6a**. In this reaction pathway, propane is first protonated on Brønsted acid sites where it undergoes either a dehydrogenation or cracking step. A carbenium ion intermediate formed by the dehydrogenation pathway is then converted into propylene, followed by oligomerization and cyclization through Brønsted acid sites for aromatic formation. In propane aromatization, PDH is a primary step, as discussed in detail by Mériaudeau and Naccache

[129, 153]. These authors carried out catalytic tests using Ga impregnated ZSM-5 in both acidic (H-) and non-acidic (Na-) form. Almost a two-fold increase in the rate of dehydrogenation using the acidic form with the same Ga content was found. Hence a bifunctional mechanism was proposed during the PDH step when both Ga oxide species in extra-framework position and protonic sites are present. On the Brønsted acid sites of HZSM-5, formation of carbenium ions ($C_3H_7^+$) is slow and thus is the rate-limiting step. In the presence of Ga oxide species, however, the propyl carbenium species are formed through a gallium alkoxide intermediate, followed by exchange with zeolite protons, thus bypassing the rate-limiting step and leading to higher rates of production of propylene. Similarly Kwak et al. also suggested a bifunctional mechanism between Brønsted and Lewis acid sites as described in **Fig. 1-6b**, where a Lewis site abstracts a hydride ion from a propane molecule, followed by propylene formation from the carbenium species after interacting with a Brønsted acid site [149]. Considering this bifunctional mechanism in PDH, the strength and concentration of Brønsted and Lewis acid sites should be important factors. The strength of the Brønsted acid sites depends on the amount and types of heteroatoms in the framework and it is known that bridged framework Ga provides less acidity than Al [154]. The Lewis acid sites are suggested to be related to positively charged oxide clusters in zeolite pore structures, normally extra-framework species [154].

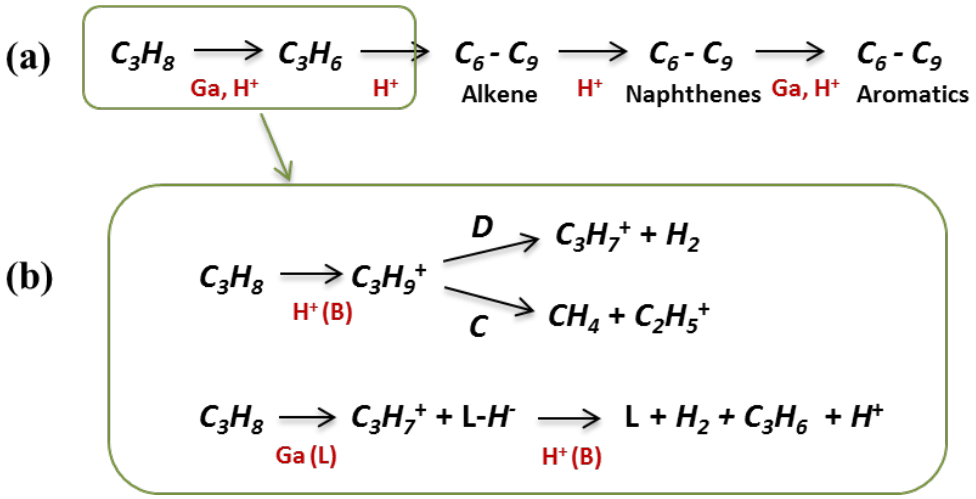

Fig. 1-6. (a) Reaction mechanism of propane aromatization in Ga loaded MFI zeolite catalyst. (b) PDH step through Brønsted acid site (top) and in presence of both Brønsted (B) and Lewis (L) acid site (bottom). D and C denote dehydrogenation and cracking pathways respectively.

During the synthesis of gallosilicate molecular sieves, the trivalent Ga^{3+} species not incorporated in the framework remain in the zeolite channels as highly dispersed oxide species [145]. Extra-framework Ga species can also be formed by degalliation of framework Ga, and the role of these species on PDH has been discussed [92, 142-145]. Simmons et al. carried out hydrothermal treatments of Ga impregnated HZSM-5 and observed a significant increase of n-butane cracking activity while the same treatment on HZSM-5 decreased the activity [92]. Bayense et al. also performed propane aromatization using gallosilicates after mild steaming and reported less activity but higher aromatic selectivities than catalysis with HZSM-5 [155]. Giannetto et al. investigated the changes in activity and aromatic selectivities using gallosilicate MFIs

with different calcination temperatures and observed increased activity and decreased ratios of cracking to dehydrogenation at calcination temperatures of 973 and 1073 K [142]. Similarly, Choudhary et al. reported the formation of extra-framework Ga by heat treatment and suggested extra-framework Ga should be the main active sites for PDH and framework Ga species were much less active for dehydrogenation [143, 144]. However, Choudhary et al. also reported that both Brønsted and extra-framework Ga sites were necessary to achieve high propane activity, suggesting a bifunctional PDH mechanism [140]. The relation between propane conversion and propylene/aromatic selectivity was studied by Guisnet et al., where high propylene selectivities (>70%) were observed at low conversion levels (<5%) while at high conversions (>20%), more aromatics were produced, with more than 50 % selectivity to aromatics [156]. Although the aforementioned studies assumed that the extra-framework Ga species were present in the zeolite pores, Ga oxide have also been found on the outer surface of zeolites upon calcination, with the oxide clusters being 3 – 10 nm in size [157].

1.4. Objectives and aims of this thesis

The overall objectives of this thesis are to develop a detailed model of propane dehydrogenation in membrane reactors, to understand the interplay of mass transport and reaction kinetics in the system, and to provide design guidelines for experimental and scaled-up operating configuration of such systems. The study also includes investigation and evaluation of novel zeolite catalysts for PDH with high conversion, selectivity, and stability with less deactivation. Overall, this study will accelerate the development of a membrane reactor system for high conversion and selectivity at high temperature. The specific objectives are as follows:

1) Performance predictions and experimental validation using a 1D model: The key performance predictions are calculated as a function of operating conditions using a 1D model for a lab scale membrane reactor. Kinetic parameters for both thermal cracking and a heterogeneous PDH reaction are obtained by fitting the modeling results on experimental data from a fixed bed reactor. The membrane permeance through zeolite membranes such as MFI and SAPO-34 are also obtained from a membrane permeation cell. I compare the modeling results with the data from our lab scale membrane reactor experiment to validate the model.

2) Investigation of the relation between operating conditions and material properties in operating windows using dimensional analysis of 1D model: The validated membrane reactor model to draw operating windows by dimensional analysis is used.

The dimensional analysis enables us to find optimal operating conditions, which are represented by Péclet (*Pe*) and Damköhler numbers (*Da*) numbers in operating windows. This clearly demonstrates the relation between operating conditions and material properties such as membrane permeance and catalytic activity. The operating windows provide useful guidelines for the design of PBMR system and hence allow us to select and/or design further improved membrane reactors and identify target parameters for optimal operation of the system.

3) Improving the PBMR model with 2D non-isothermal effects: The capability of the PBMR model is improved to provide accurate predictions in a scaled-up system although 1D isothermal model can provide a good prediction for the lab scale PBMR. The main improvements to the model include the effect of mass dispersion in a packed bed catalysts and non-isothermal effects from the endothermic reaction. The 2D non-isothermal model shows more detailed flow pattern in the catalytic side and enables us to predict the endothermic temperature drop and thermal effect from high temperature sweep gas.

4) Investigation of candidate PBMR configurations: I consider more effective PBMR configurations such as applying multi-membrane tubes with different size with packed bed catalysts in the shell side. From the detailed 2D model, the required membrane surface area and catalytic volume ratio are calculated for a target PDH performance. Then we obtain the number of membrane tubes in a fixed catalytic volume, which is the packing density of the membranes. I demonstrate the relation between the packing

density and membrane reactor volume for the design of scaled-up PBMR. The types of membrane support in this study include conventional ceramic tubes and hollow fiber type ceramic supports.

5) PDH plant simulation using 2D PBMR ASPEN-FORTRAN model: I further investigate the membrane reactor performance and its effect on the PDH plant. I develop a 2D non-isothermal PBMR model embedded ASPEN-FORTRAN simulation that integrates the PBMR PDH and downstream separation processes. The PDH performance between PBR and PBMR is compared in various operating ranges and calculate the required energy for both non-recycled and recycled system to find out better operating configuration of the PDH plant. The energy calculation includes inter-stage heaters, sweep gas removal, and C_3 splitter for propane/propylene separation.

6) Development of a novel Ga-containing zeolite catalyst from perturbed acidities: I synthesize and characterize gallium containing MFI zeolite catalysts for propane dehydrogenation with different amount of 3-mercaptopropyl-trimethoxy silane (MPS) addition. MPS-free gallosilicate, proton exchanged gallosilicate, and Ga impregnated pure-silica MFI zeolite are also prepared for a comparison. I use chemisorption techniques to investigate the acid sites, which include temperature programmed desorption (TPD) of ammonia and isopropyl amine, and pyridine FT-IR method to identify Brønsted and Lewis acid sites. PDH reaction using MPS-gallosilicates are conducted and compared with commercial Cr oxide catalyst and conventional gallosilicate catalyst.

CHAPTER 2

1-D MODEL OF A PACKED BED MEMBRANE REACTOR FOR PROPANE DEHYDROGENATION AND ITS EXPERIMENTAL VALIDATION

2.1. Introduction

The propane dehydrogenation (PDH) reaction in a packed bed membrane reactor (PBMR) involves both catalytic PDH reactions and thermal cracking, combined with membrane permeation. Since the enhancement of the conversion depends on the interplay between the reaction rate and membrane transport, I investigate the PBMR performance by modeling studies using a 1D model. The reaction kinetics and membrane properties were examined independently using a fixed bed reactor and a membrane permeation cell respectively to obtain the kinetic parameters and membrane permeance data.

I investigate the PDH kinetic studies using the Cr_2O_3 catalyst and obtain parameters best fitting the experimental data. As mentioned in Chapter 1, the PDH reaction mechanism on a Cr_2O_3 catalyst was based on Langmuir-Hinshelwood mechanism, and several kinetic models were suggested from different rate determining step assumptions. I determine a reliable kinetic model considering both experimental observation and consistency with the assumptions of each rate determining step such as whether the kinetic model considers the surface coverage of propane or propylene. Along

with the catalytic reaction, thermal cracking reactions also occur in gas phase at high temperature. Froment et al. carried out detailed studies of propane thermal cracking reactions at high temperature range (775 ~ 825 °C) and reported kinetic parameters and their activation energies [158, 159]. I analyze thermal cracking experiments to find parameters at 600 °C.

The PDH experiments in a lab scale PBMR are also carried out in order to validate the model. I fabricated MFI and SAPO-34 zeolite membranes on ceramic tubular Al_2O_3 supports as candidate materials for the PDH application in PBMR. High temperature permeance data of propane, propylene, and hydrogen are obtained through a membrane permeation cell before carrying out the PDH test.

2.2. Modeling scheme and experimental methods

2.2.1. Governing equations for 1D isothermal operation

The present PBMR model features the addition of membrane flux to a conventional PBR model (**Fig. 1-3**). The governing equations for any component on each side of the PBMR are:

$$\frac{dF_t}{dz} = rg_{cat}' - Q \cdot \left(P_t - P_s\right) 2\pi R_1 \qquad \text{(Tube)} \qquad (2\text{-}1)$$

$$\frac{dF_s}{dz} = Q \cdot \left(P_t - P_s\right) 2\pi R_1 \qquad \text{(Shell)} \qquad (2\text{-}2)$$

Here F, Q, P and R_1 represent molar flow rate (mol.s^{-1}), membrane permeance (mol.s^{-1}.m^{-}

^{2}.Pa^{-1}), pressure (Pa), and tube radius (m) respectively. The subscripts *t* and *s* denote the tube and the shell sides. The *r* term denotes the reaction kinetics and g_{cat}' refers to mass of catalyst per unit reactor length (g/m). The above governing equations are derived from material balance equations for each component (propane, propylene and hydrogen). I assume isothermal operation, plug flow inside the tube, no axial dispersion, and no radial diffusion. The mass transfer resistance of the membrane support and the pressure drop in the packed bed are neglected. To solve this equation, I can use either basic explicit Euler method or the MATLAB subroutine "ode23s", which is based on the implicit one-step modified Rosenbrock method[160]. The total pressure on the tube and the shell side is kept constant, typically at 1 atm in open system. At each step position along the reactor length, the partial pressures of the components on the tube and the shell are calculated (from the molar flow rates of each component), and the membrane flux is updated by multiplying these partial pressure differences with the component permeance *Q*. The membrane thickness is much smaller than the reactor radius, and hence for simplicity I use the same R_1 in the governing equations for both the tube and shell sides. Also, it is expected that the multicomponent diffusion and competitive adsorption effects become weak at high temperature, and hence the single-gas permeances (obtained from single-gas permeation experiments) can be used. The propane conversion is defined as

$$\text{Conversion} \equiv \frac{\text{Feed}_{\text{propane}} - \text{Total outlet}_{\text{propane}}}{\text{Feed}_{\text{propane}}} \tag{2-3}$$

2.2.2. Membrane reactor apparatus

The key performance prediction that can be obtained from the membrane reactor with MFI and SAPO-34 membranes is the enhancement of the PDH conversion. The conversion depends on process conditions such as temperature, weight hourly space velocity (WHSV, hr^{-1}), and sweep flow rate, which can be easily controlled and varied during the experiments. For the validation of our model, the conversion with various operating conditions is calculated for a lab scale membrane reactor. The temperature and pressure are 500 ~ 600 °C and 1 atm. For a range of WHSV (*e.g.*, 0.1-1 hr^{-1}), the PDH conversions are calculated at each temperature and sweep flow rate, and can be directly compared with the experimental results.

The design of the membrane reactor is shown in **Fig. 2-1**. The membrane reactor consists of inlet streams of feed and sweep gas and outlets streams of retentate and permeate sides as described. The space velocity can be varied by controlling feed flow rates at a fixed amount of catalyst packed in the membrane tube, and Ar sweep gas is used. The outlet flow goes to a GC so that propane conversion and propylene selectivity can be measured. The membrane permeation experiments are also carried out in the same membrane reactor without packed bed catalysts. MFI and SAPO-34 zeolite membranes are used, which are fabricated by a secondary growth method on a tubular Al_2O_3 support and placed between the tube (feed) and shell (permeate) side. The radius and length of the tubular membrane is 0.4 and 7 cm respectively.

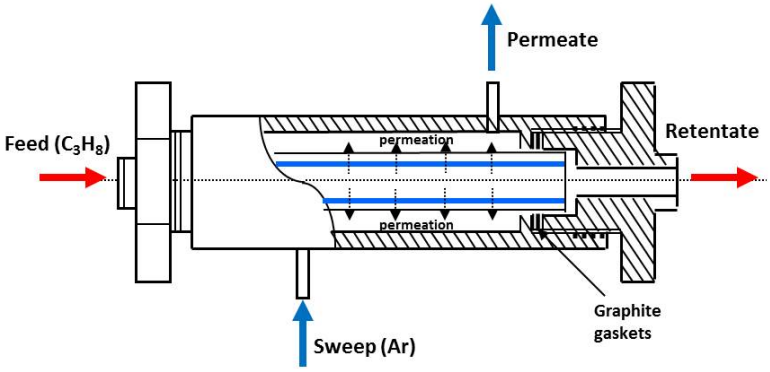

Fig. 2-1. Design of membrane reactor apparatus

2.2.3. Reaction kinetics of propane dehydrogenation and thermal cracking

Reaction kinetic experiments are conducted using a quartz fixed bed reactor in the temperature range 500-650 °C. I use commercially available catalysts such as Na doped Cr_2O_3/Al_2O_3, which is prepared by incipient wetness impregnation with a composition of 20 wt % Cr and 1 wt % Na. Similar to the membrane reactor, 100 mg of catalysts are placed in the tube. Total pressure is fixed at 1 atm, but propane feed concentrations are varied at a fixed total flow rate (20 cc.min^{-1}) with nitrogen balance. During the PDH reaction, the product stream was analyzed by the on-line GC (Shimadzu GC2014) using a flame ionization detector (FID) for hydrocarbon products and thermal conductivity detector (TCD) for H_2. The detectors in GC were pre-calibrated using known concentration (ppm level) of hydrocarbon standard gas mixtures with peak areas of each component. The propane conversion and product selectivities were calculated based on the feed conditions and the concentration of the products. The conversions are measured with time at each feed condition, and the kinetic parameters will be obtained by fitting the experimental data. At each feed condition, the initial data point is used for the parameter

fitting before the catalysts become highly deactivated. Hence the coke formation is not considered in the parameter fitting since this study mainly focuses on how much of enhancement we achieve by operating the PBMR rather than characterizing the deactivation behavior of the catalyst.

The Langmuir-Hinshelwood mechanism for PDH reaction is applied to describe the kinetics for Cr_2O_3 catalyst. In this mechanism, the surface coverage of intermediate species (C_3H_7) is not considered, and the desorption of H_2 is also relatively fast. It is first assumed that propane adsorption on the catalytic surface is the rate determining step as reported in the literature [7, 121]. This mechanism hence neglects propane coverage on the surface, and the reaction is inhibited by propylene adsorbed on the surface. This kinetic equation (LH1) can be expressed as follows:

$$r_A^{LH1} = \frac{k_1\left(P_A - 1/K_{eq}\left(P_B P_C\right)\right)}{1+K_{a2}P_B} \tag{2-4}$$

$$\begin{pmatrix} k_1 = k_1^{\,0}\exp\left(\frac{-E_a}{R_g}\left(\frac{1}{T}-\frac{1}{T_0}\right)\right) \\ K_{a2} = K_{a2}^{\,0}\exp\left(\frac{-\Delta H_a}{R_g}\left(\frac{1}{T}-\frac{1}{T_0}\right)\right) \end{pmatrix} \quad \left(T_0 = 873\,K\right)$$

Other kinetic models can be also suggested if the surface reaction is the rate determining step. In this assumption, since the adsorption of propane is relatively fast, now the kinetic models consider the surface coverage of both propane and propylene molecules. The kinetic models (LH2 and LH3) are as follows, depending on whether the rate determining step is the whole surface reaction ($C_3H_8{\cdot}S \rightarrow C_3H_6{\cdot}S + H_2$) or only the 1st

($C_3H_8 \cdot S + S \rightarrow C_3H_7 \cdot S + H \cdot S$) reaction step:

$$r_A^{LH2} = \frac{k_1 K_{a1}\left(P_A - \left(P_B P_C\right)/K_{eq}\right)}{1 + K_{a1}P_A + K_{a2}P_B} \quad (2\text{-}5)$$

$$r_A^{LH3} = \frac{k_1 K_{a1}\left(P_A - \left(P_B P_C\right)/K_{eq}\right)}{\left(1 + K_{a1}P_A + K_{a2}P_B\right)^2} \quad (2\text{-}6)$$

Here, k_1 is forward reaction rate ($mol.s^{-1}.g_{cat}^{-1}.kPa^{-1}$), K_{eq} is temperature dependent equilibrium constant (kPa), K_{a1} and K_{a2} are adsorption parameters for propane and propylene, respectively, on Cr_2O_3 surface (kPa^{-1}), and P_A, P_B, P_C are partial pressures of propane, propylene, and hydrogen respectively (kPa).

The kinetic parameters for thermal cracking in gas phase are also obtained from experiments in the empty quartz tube at 600 °C and the results are compared with the literature [158, 159].

2.3. Results and discussion

2.3.1. 1D results of packed bed membrane reactors

The PBMR breaks the equilibrium limitation and shifts the conversion to a higher value. An example is shown in **Fig. 2-2**, which shows mole flux of each component in the tube side in PBR and PBMR. A H_2 selective membrane where the permeances ($mol.s^{-1}.m^{-2}.Pa^{-1}$) of propane is applied and propylene are assumed to be small (10^{-10}) while the hydrogen permeance is 10^{-7}. In order to achieve the best performance of PBMR,

membrane permeation of both propylene and hydrogen would be ideally preferred. However, since high propane/propylene selectivity is difficult to achieve at high temperature due to their similar molecular sizes, it is aimed to confirm that the enhancement of conversion can be also made solely by H_2 permeation. In **Fig. 2-2a**, the propane flux in the PBR shows no change after it reaches the equilibrium, whereas the propane flux in the PBMR keeps decreasing along the reactor length in **Fig. 2-2b**, thereby increasing propylene production and the PDH conversion. This result confirms that the PBMR breaks the equilibrium even with only H_2 permeation. For the same membrane, the conversion obtained in the PBMR can be varied with different process conditions such as reactor size and feed flow rate once the system breaks the equilibrium as shown in **Fig. 2-3.** The conversion clearly increases with decreasing feed flow rates and increasing reactor length. Also increase in the tube radius shows higher conversion at fixed flow rates. These results are reasonable since a larger reactor and low feed flow rate lead to lower WHSV range at fixed void fraction and it gives relatively more membrane permeation throughput compared to the convective transport rate. The interplay between operating conditions and membrane properties will be more investigated in detail from Chapter 3.

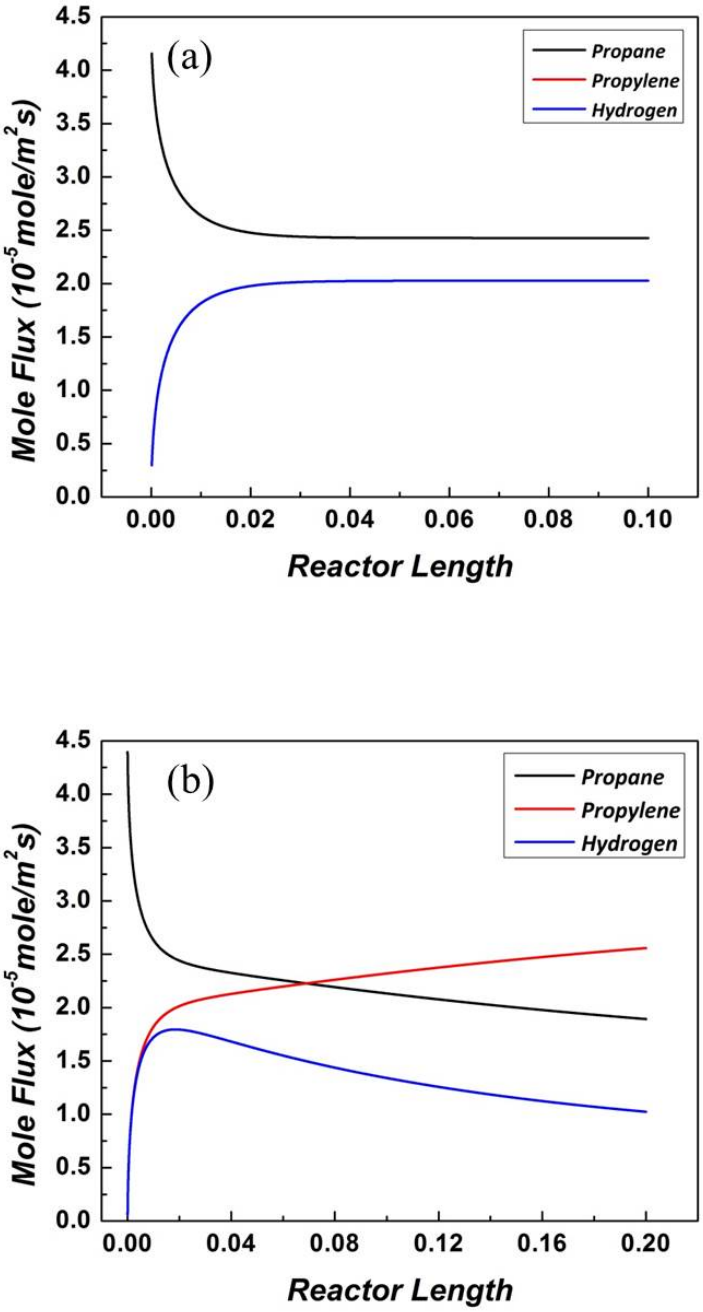

Fig. 2-2. Modeling results of mole flux profiles along the reactor length: (a) PBR and (b) PBMR.

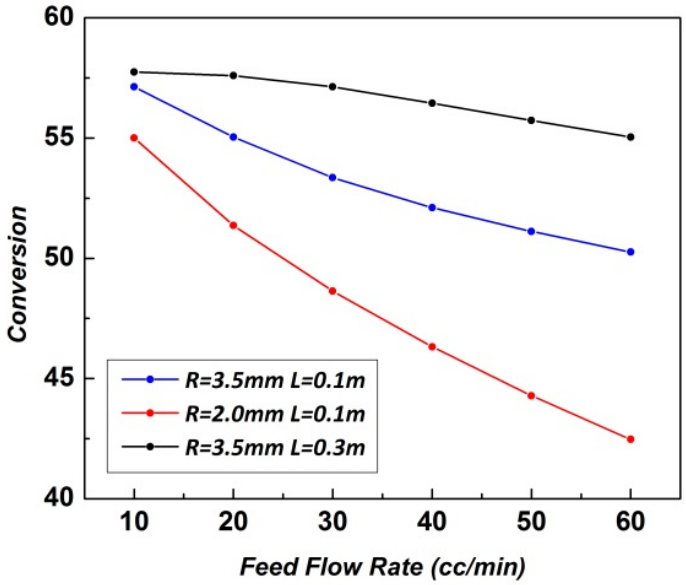

Fig. 2-3. Modeling results of conversion with different operating conditions.

2.3.2. Parameters for Cr_2O_3 catalyst and thermal cracking

In a typical PDH test using a fixed bed reactor, time on stream data of the PDH conversion is decreasing due to the deactivation of catalyst, which can be fit by an exponential decaying function as observed in **Fig. 2-4a**. Since the initial activity can be maintained by the regeneration process with a short cycle as discussed, the first data at each condition in **Fig. 2-4a** are only considered for the parameter fitting. The experimental data of the PDH conversion have only 1 ~ 3 % of errors from each conversion value, considering the ppm level detection in the on-line GC.

The first kinetic model (LH1) for the parameter fitting is first tested. The rate expression with the unknown variables k_1 and K_{a2} can be integrated in a packed bed reactor (PBR) model, which uses the same governing equation as the tube side PBMR

model without membrane permeations. Combining the PBR model and Matlab subroutine 'nlinfit' function, which is based on a least squares method, I can fit the experimental data and find kinetic parameters as shown in the **Fig. 2-4b**. Similarly in **Fig. 2-5**, I also conduct the PDH experiments with different operating temperatures to find the reaction activation energy (E_a) and heat of adsorption (ΔH_a) of K_{a2} using Arrhenius relation as described in the rate expression. The parameters obtained from **Fig. 2-4** and **Fig. 2-5** are listed in **Table 2-1**. Compared to the previously reported parameters on Cr_2O_3 catalyst [7], k_1, K_{a2} and E_a are in the similar order of magnitude, but ΔH_a is different. This is plausible because the surface condition cannot be exactly the same considering different preparation method such as Na addition.

Parameter fitting using the other kinetic models (LH2 and LH3) is also performed with the same fitting method used for the LH1 model. In **Fig. 2-6**, all models show good fitting of the experimental data and therefore LH2 and LH3 cannot be excluded as possible kinetic models. The kinetic parameters are also summarized in **Table 2-1**. Since the LH2 and LH3 models consider the surface coverage of both propane and propylene, the equilibrium parameters for the adsorption (K_{a1}) are assumed to be in the similar order of magnitude to K_{a2}. However, the parameter values of K_{a1} are not consistent with the assumption. Although I are able to obtain the kinetic parameters using the LH2 and LH3 models, the parameter values still indicate that the surface coverage of propane should be much lower than that of propylene. Hence, the model parameters for the LH2 and LH3 are not physically reliable and I apply the LH1 for the PDH kinetic model on Cr_2O_3 catalyst.

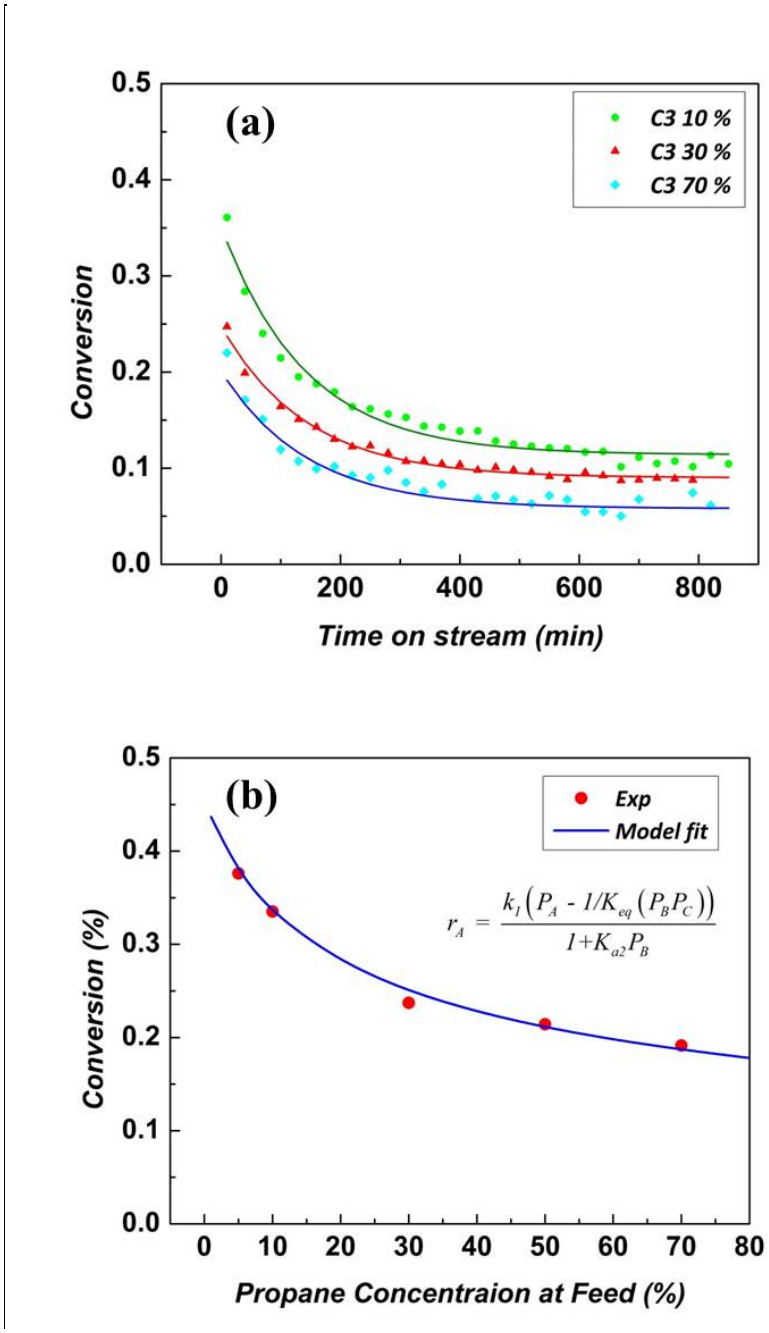

Fig. 2-4. (a) The deactivation of the PDH conversion. The curves are from the exponential decaying function. (b) fitting the experimental data with different propane feed concentrations at 600 °C.

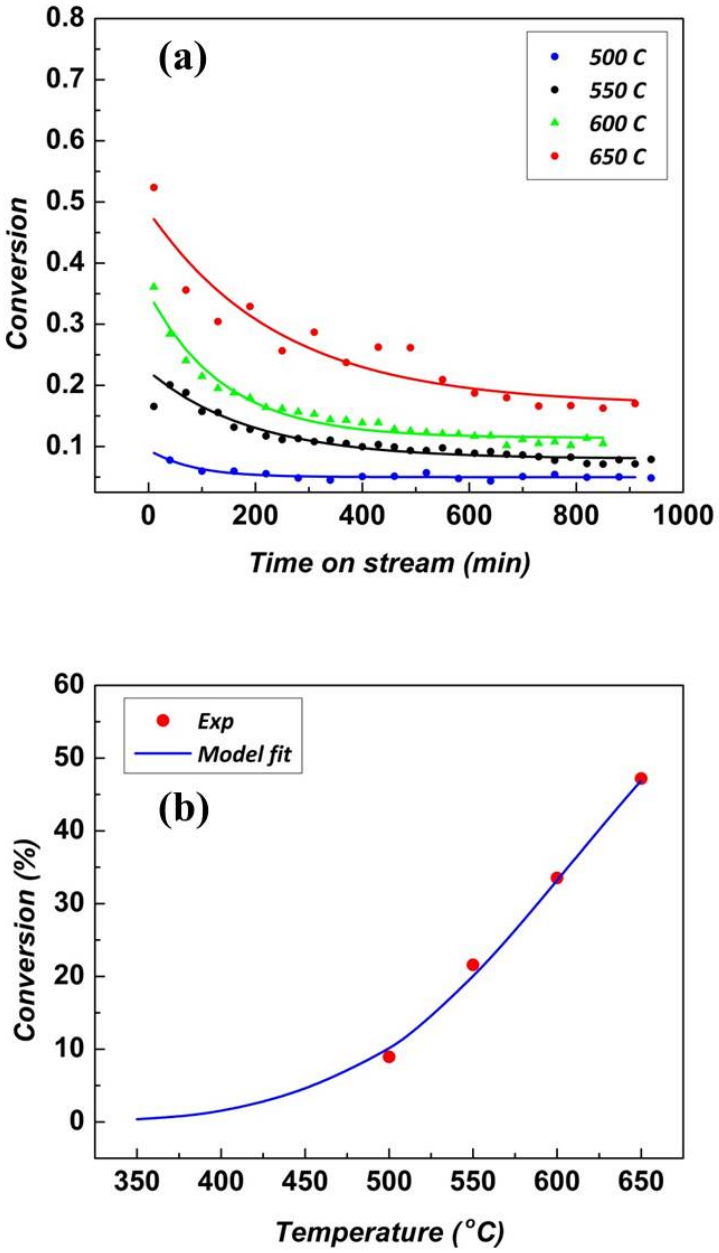

Fig. 2-5. (a) The time on stream PDH conversion with different operating temperature. (b) fitting the experimental data with different temperatures at 5 % propane feed.

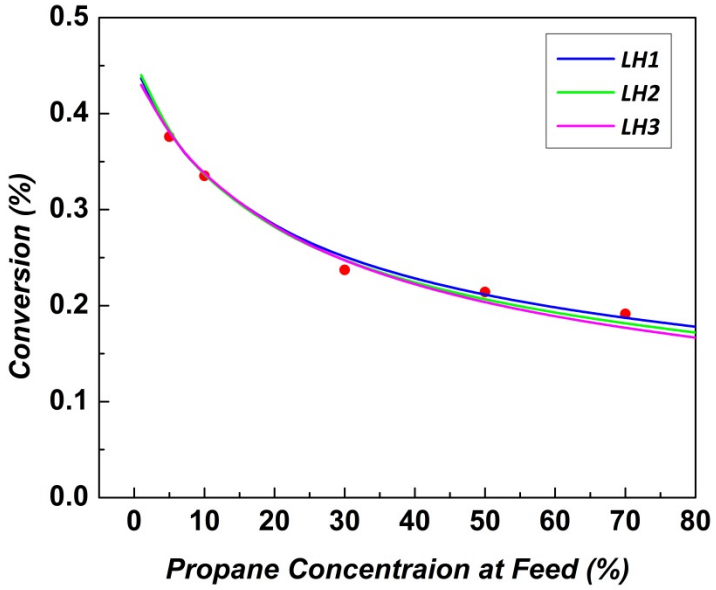

Fig. 2-6. Fitting the experimental data using LH1, LH2 and LH3 models.

Table 2-1. Kinetic Parameters of the PDH using the Na doped Cr_2O_3/Al_2O_3 catalysts.

	$k_1 \times 10^7$ (mol/s/g_{cat}/kPa)	K_{a1} (1/kPa)	K_{a2} (1/kPa)	ΔH_a (kJ/mol)	E_a (kJ/mol)
LH1	8.2 ± 0.2	-	0.26 ± 1e-3	-151 ± 9.0	37 ± 3.5
LH2	8.3 ± 0.2	3.6e-3 ± 1e-4	0.26 ± 1e-3	not tested	not tested
LH3	8.0 ± 0.1	4.0e-4 ± 1e-4	0.1 ± 1e-3	not tested	not tested
Gascon et al. (LH1)	6.9	-	0.23	-595	36

Thermal cracking experiments using the empty quartz reactor are also carried out. The kinetic parameters and their activation energies for thermal cracking of propane were already reported in the literature at temperatures higher than 700 °C [158, 159]. In this experimental condition at 600 °C, the kinetic parameters obtained by extrapolating the reported parameters using the activation energies overestimate the thermal cracking conversion as shown in the **Fig**. **2-7**. This overestimation may be caused by inaccuracy of the parameters I obtained by extrapolating the reference data. Similar to the previous section, I also conducted non-linear fitting with our own data and obtained more reliable reaction parameters for the thermal cracking. The same quartz tube reactor without catalysts is used at 600 °C and atmospheric pressure. I keep 50 % of propane feed concentration with different total flow rates using nitrogen balance to vary the residence time of the reactant.

During the thermal cracking reactions in the empty quartz tube at 600 °C, I mainly observe C_1, C_2, and C_3 cracking products and negligible concentrations of C_4 or aromatic

hydrocarbons. Also the coke, which is mainly observed during the catalytic test, is not formed in the gas phase reaction at 600 °C. Hence among the list of thermal cracking reactions in Sundaram and Froment [159], I choose candidate reactions which produce C_1 to C_3 components as follows:

$$C_3H_8 \xrightarrow{kc_1} C_2H_4 + CH_4$$

$$C_3H_8 \underset{kc_{-2}}{\overset{kc_2}{\rightleftharpoons}} C_3H_6 + H_2$$

$$C_3H_8 + C_2H_4 \xrightarrow{kc_3} C_2H_6 + C_3H_6$$

$$2C_3H_6 \xrightarrow{kc_4} 3C_2H_4$$

$$C_2H_6 \underset{kc_{-5}}{\overset{kc_5}{\rightleftharpoons}} C_2H_4 + H_2$$

At each residence time, experimental data of total propane conversion and product distributions are used for the non-linear fitting as described in the **Fig. 2-8** and the cracking parameters are listed in the **Table 2-2**. The equilibrium constants for thermal cracking reactions were adopted from Sundaram and Froment [159].

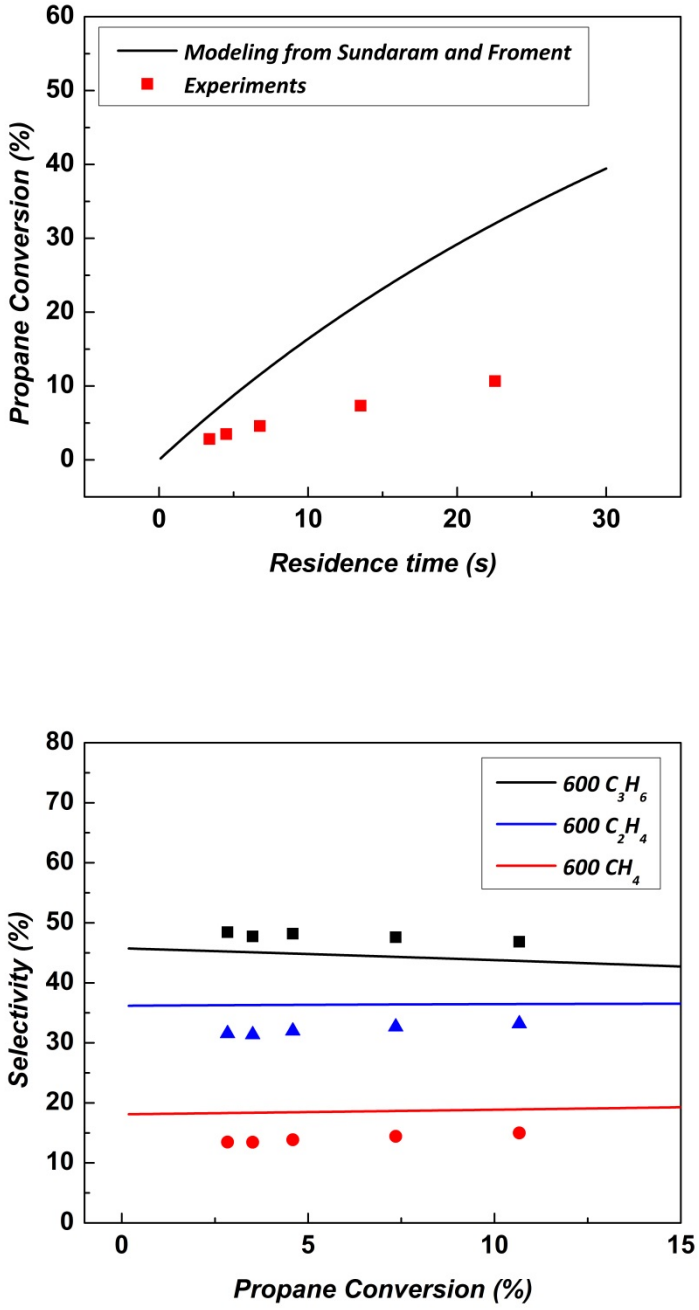

Fig. 2-7. (a) Overestimation of conversions and (b) inaccuracy of product selectivities from thermal cracking model.

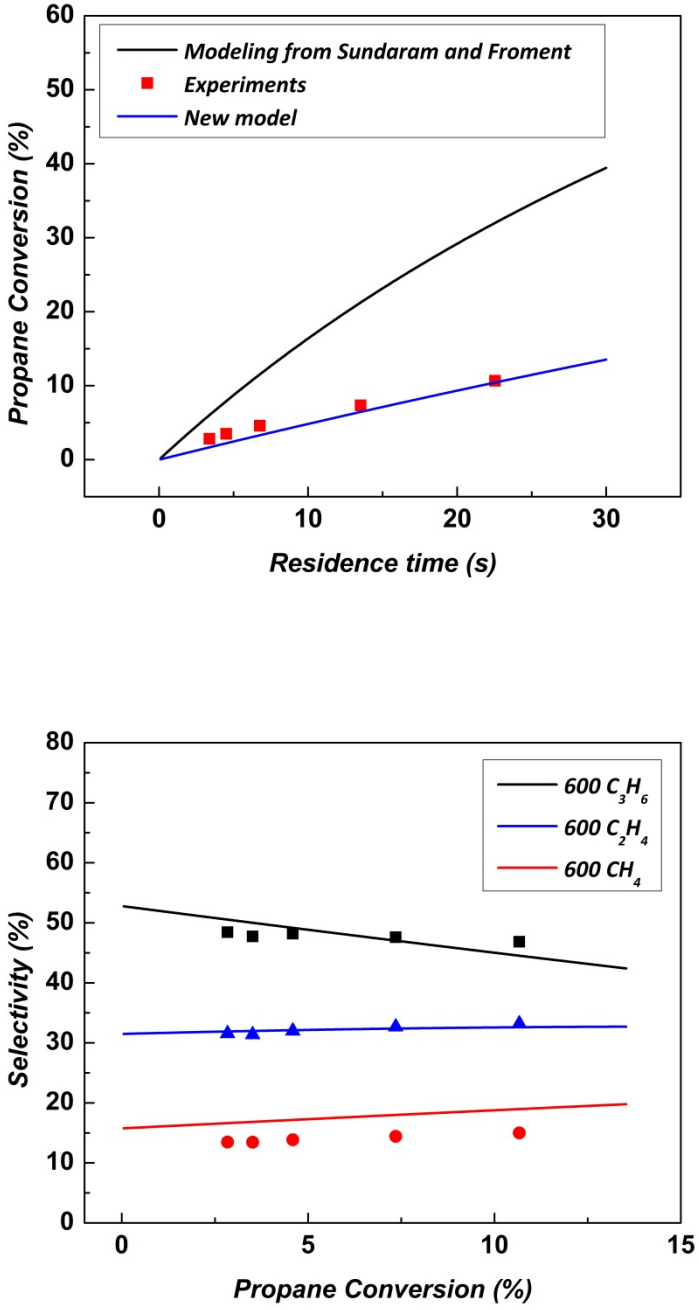

Fig. 2-8. Parameter fitting for (a) conversions and (b) product selectivities for thermal cracking model.

Table 2-2. Kinetic parameters of thermal cracking.

kc_1 (mol/s/m^3/kPa)	kc_2 (mol/s/m^3/kPa)	kc_3 (mol/s/m^3/kPa^2)	kc_4 (mol/s/m^3/kPa)	kc_5 (mol/s/m^3/kPa)
3.1e-4	3.1e-4	2.4e-5	6.2e-4	2.1e-4

The thermal cracking expressions can be combined with the catalytic reaction in the PBR model. One may argue that the background cracking conversion should be subtracted from the real experimental data. However, our new detailed model shows that there is competitive kinetics between the thermal cracking and the catalytic PDH reaction, with the result that the thermal cracking conversion is much lower in the catalytic reactor as compared to the empty tube. Thus in most of the operating conditions (residence times less than 10 s), the contribution of thermal cracking can be neglected in our results, as shown in **Fig. 2-9.** In such conditions where the thermal cracking contribution cannot be negligible due to large residence time, the combined model with catalytic and thermal cracking model can be used.

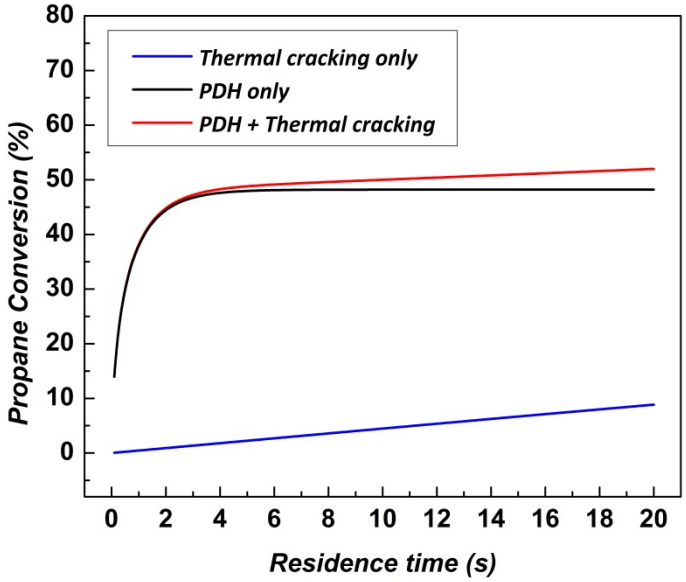

Fig. 2-9. PBMR modeling results with and without thermal cracking.

2.3.3. Comparative studies between modeling and experiments

The modeling predictions using the PBMR 1D model are made using kinetic parameters and membrane permeance values. The membrane permeances of propane, propylene and hydrogen are summarized in **Table 2-3**. The thickness of the MFI and SAPO-34 membranes are about 5 and 1 μm respectively, and therefore the H_2 permeances of SAPO-34 is larger than MFI even with smaller pore size. In **Fig. 2-10**, I compare PDH conversions with respect to different operating temperature in PBR and PBMR using MFI membrane. The feed flow and sweep flow rates are fixed at 5 and 20 $cc.min^{-1}$ respectively, and apply the fixed amount of catalyst (g_{cat}, 1.2 g). The modeling results include the contribution from thermal cracking, and the reaction rate at each

operating temperature is interpolated based on the activation energy obtained from parameter fitting. It is observed that the modeling and experiments show good agreement. **Fig**. **2-11** shows the PDH conversions with increasing Ar sweep flow rate in PBMR operation using MFI membrane. The feed flow rate and g_{cat} are the same as the previous conditions. I can see an increasing trend of the PDH conversion with increasing sweep flow rate in both modeling and experiments due to increasing driving force of membrane permeation. However, for both case, the PDH conversion levels off at large sweep flow rate. Although a large sweep flow rate increases the driving force of membrane permeation, it will decrease the partial pressure difference from a middle of the reactor due to increased concentration of permeated gas in the shell side. Also increasing membrane permeation from large sweep flow rates means that propane permeation is also increased, which will rather decrease the conversions. In **Fig. 2-11 and Fig. 2-12,** the modeling results a little overestimate the conversions at large sweep flow and low WHSV region. This is possibly due to mass transport resistances near the membrane surface, which may affect more at large sweep/feed ratios where large membrane transport rates are expected. **Fig. 2-12** shows conversions at different WHSV in PBR and PBMR operations using MFI and SAPO-34 membranes. The sweep flow rates and g_{cat} are fixed at 20 $cc.min^{-1}$ and 1.2 g respectively, and then different feed flow rates are applied. In **Fig. 2-12**, the conversions are decreasing with increasing WHSV not only due to slow kinetics at higher WHSV, but also the effects from membrane permeation become relatively lower due to large convective flow rates. At low WHSV region, large increase in conversion is observed, which is mainly due to increasing contribution from thermal cracking at longer residence time considering that even the conversion of PBR is higher than the

equilibrium (~48 % at 600 °C).

Table 2-3. Permeance ($mol.s^{-1}.m^{-2}.Pa^{-1}$) data from permeation experiments using MFI and SAPO-34 membranes.

	MFI			**SAPO-34**		
T (°C)	C_3H_8	C_3H_6	H_2	C_3H_8	C_3H_6	H_2
500	2.9e-8	2.8e-8	1.5e-7	8.0e-9	8.8e-9	1.9e-7
550	2.5e-8	2.5e-8	1.6e-7	8.6e-9	9.5e-9	2.0e-7
600	2.4e-8	2.3e-8	1.6e-7	8.7e-9	9.6e-9	2.4e-7

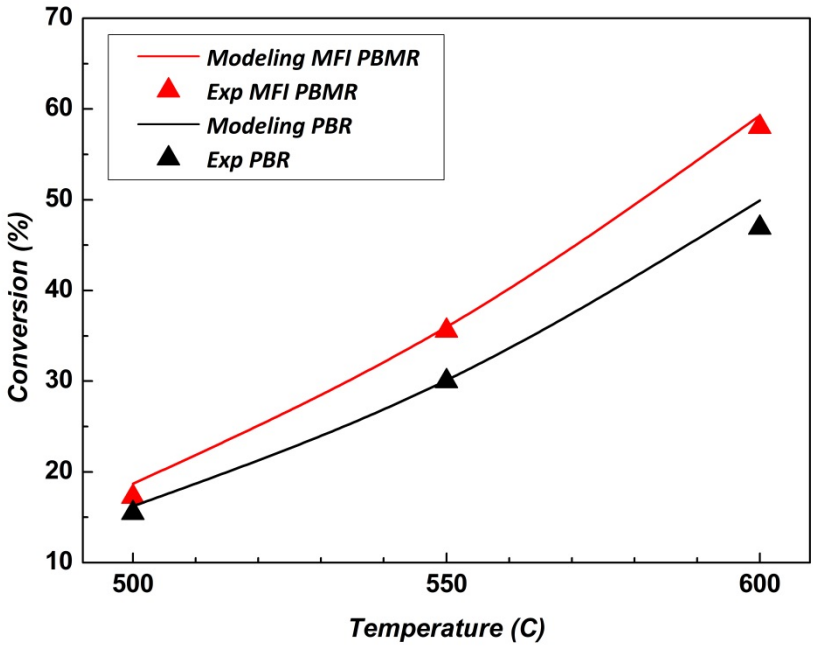

Fig. 2-10. The comparison between modeling and experimental results of PDH conversion in PBMR and PBR with respect to operating temperatures.

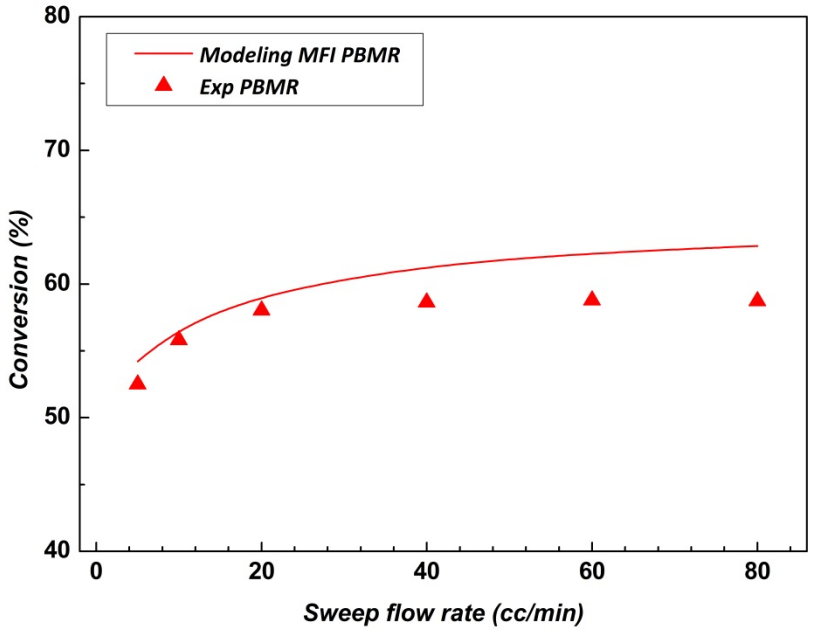

Fig. 2-11. The comparison between modeling and experimental results of PDH conversion in PBMR using MFI membrane with respect to sweep flow rate.

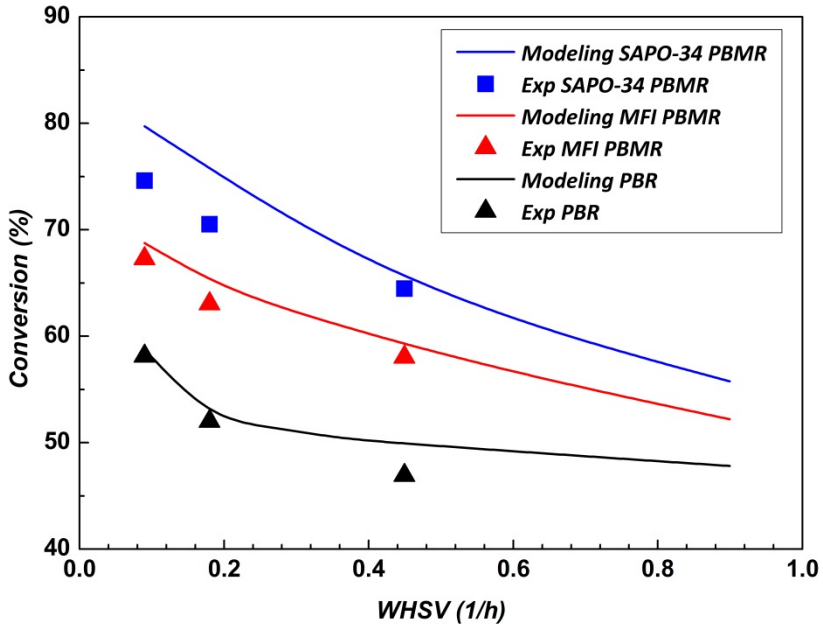

Fig. 2-12. The comparison between modeling and experimental results of PDH conversion in PBMR and PBR with respect to WHSV.

2.4. Conclusions

PDH experiments in a fixed bed reactor are carried out to find reaction kinetic parameters on Cr_2O_3 catalyst. The experimental data are obtained in varied propane concentrations at a fixed total flow rate. Combining our PFR model and the Matlab subroutine 'nlinfit' function, I fit the experimental data based on the least square method. Based on the rate determining step, several different kinetic models are suggested. From our kinetic parameter fitting, adsorption of propane on the catalytic surface should be the rate determining step, which is consistent with previous literature. Thermal cracking experiments were also performed based on possible thermal cracking reactions reported previously. Similarly new kinetic parameters for thermal cracking are also updated at 600 °C. I combined the PDH reaction and thermal cracking reactions in the PBMR model. The results indicated that the contribution from thermal cracking would be small due to competitive kinetics with the heterogeneous PDH reaction, and therefore can be negligible in many cases with short residence time. Modeling and experimental results in PBMR were compared in various operating conditions. There exist a little overestimation from modeling results at large sweep flow rates and low WHSV conditions, which is due to neglecting mass transport resistances near the membrane surface. However, the modeling and experimental data show good agreements at WHSV range more than 0.4 hr^{-1} for a lab scale PBMR. This 1D model can be also used for analysis of interplay between operating conditions and membrane properties for better PBMR performance. I will further discuss this in the next Chapter.

CHAPTER 3

MATERIAL PROPERTIES AND OPERATING CONFIGURATIONS OF PACKED BED MEMBRANE REACTORS FOR PROPANE DEHYDROGENATION

3.1. Introduction

Modeling and experimental studies of PBMR show clear potential for obtaining enhancement in conversion over conventional reactors. Although complex models for membrane reactors have been developed, the previous literature has considered the PBMR performance (e.g., conversion and yield) only in a limited range of operating conditions and material parameters. Relatively little attention has so far been paid to understanding in detail the operating 'windows' of PBMRs as a function of the catalyst and membrane performance parameters and the system operating parameters, particularly for PDH. Such a study would be useful in the design and selection of appropriate PDH PBMR materials and configurations for target applications, and in understanding the complex interaction of membrane permeation and catalyst kinetics in PBMRs. In the present study, I construct a sufficiently detailed model of PDH in a PBMR and then use it to systematically study the PBMR performance characteristics over a wide range of possible material and operating parameters, including cocurrent and countercurrent sweep modes. For the sake of simplicity, our model does not consider non-isothermal operation

or radial dispersion. Our approach here is to use a relatively simple model to identify appropriate operating windows for PDH PBMRs, which can then be investigated in further detail *via* more complex models and targeted experiments. I use dimensional analysis to identify the operating windows for PDH PBMRs for desired performance levels and to specify realistic yet high-performance membranes, catalysts, and operating configurations. Building upon previous PBMR modeling literature for other dehydrogenation reactions [65, 66, 161], I present here a more detailed investigation of PDH PBMRs covering a broad range of material and operating parameters, operating configurations such as counter current sweep gas operation and multiple membrane tubes, and place greater emphasis on determining the required membrane properties necessary to obtain target performance in the PDH reaction. The objectives of this Chapter are to better understand the interaction of mass transport and reaction kinetics in the operating windows and to clarify the realistic upper bounds of performance enhancement in PDH PBMRs. Finally, I also make an illustrative comparison of our convenient isothermal model with a more detailed non-isothermal 2D model to confirm the validity of our main assumptions.

3.2. Modeling scheme and operating conditions

For most of the following discussion, I assume isothermal operation, plug flow inside the tube, no axial dispersion, and no radial diffusion. A discussion confirming the general validity of these assumptions in PDH PBMRs is presented towards the end of this chapter. The mass transfer resistance of the membrane support and the pressure drop in the packed bed are neglected. The same governing equations and assumptions from the

1D model in Chapter 2 are used. The total pressure on the tube and the shell side is fixed at 1 atm. At each step position along the axial direction, the membrane flux of each component is updated from the partial pressure differences and experimentally obtained permeance values. To solve the governing equations, I use the explicit Euler method for the cocurrent mode and the implicit one-step modified Rosenbrock method [160] for the countercurrent mode.

There are several papers describing the mechanisms for PDH reaction on chromium oxide-based and platinum-based catalysts [2, 7, 21]. In this Chapter the known Langmuir-Hinshelwood kinetics model for PDH on a Pt-Sn/Al_2O_3 catalyst is employed. In this model, propane is physisorbed on Pt-Sn, followed by step-by-step dehydrogenation reactions on the surface, and finally the desorption of chemisorbed propylene and hydrogen [21]. This mechanism is described by the following overall rate equation:

$$r = \frac{k_1\left(P_{C_3H_8} - 1/K_{eq}\left(P_{C_3H_6}P_{H_2}\right)\right)}{\left(1+K_{C_3H_6}P_{C_3H_6}+\left(K_{H_2}P_{H_2}\right)^{0.5}\right)^2} \quad (3\text{-}1)$$

Here, k_1 is the forward reaction rate ($mol.s^{-1}.g_{cat}^{-1}.kPa^{-1}$), K_{eq} is the temperature-dependent kinetic equilibrium constant, and K_i are the adsorption constants on the Pt-Sn surface. The temperature-dependent kinetic parameters are obtained from the rate constants and activation energy parameters given by Li et al.[21] , and the operating temperature is 600°C. The PDH conversion is calculated accounting for the total outlet mole flow rate of propane including both the tube and shell (due to membrane permeation)

side.

3.2.1. Dimensional analysis

To gain insight into the PBMR performance in a wide range of operating conditions, I non-dimensionalize the governing equations using a characteristic flow rate and length, which are the feed flow rate (F) and reactor length (L) respectively:

$$\frac{d\left(\tilde{v}_t y_t\right)}{d\tilde{z}} = Da\left(\frac{\left(y_{C_3H_8} - P_{total}/K_{eq}\left(y_{C_3H_6}y_{H_2}\right)\right)}{\left(1+K_{C_3H_6}P_{C_3H_6}+\left(K_{H_2}P_{H_2}\right)^{0.5}\right)^2}\right) - \frac{1}{Pe}\alpha\left(y_t - R_p y_s\right) \qquad \text{(Tube)} \qquad (3\text{-}2)$$

$$\frac{d\left(\tilde{v}_s y_s\right)}{d\tilde{z}} = \frac{1}{Pe}\frac{\alpha}{R_s}\left(y_t - R_p y_s\right) \qquad \text{(Shell)} \qquad (3\text{-}3)$$

$$\sum y_t = 1, \sum y_s = 1 \qquad (3\text{-}4)$$

$$\left(\begin{array}{l} Da = \dfrac{k_1 R_g T(1-\varepsilon)L\rho_{cat}}{v_{t0}}, \quad Pe = \dfrac{v_{t0}}{Q_{H_2}\cdot R_g T}\dfrac{R_1}{2L} \text{ or } \dfrac{v_0\delta_{mem}}{D_{H_2}}\dfrac{R_1}{2L}, \\ \alpha_i = \text{membrane selectivity}\left(Q_i / Q_{H_2}\right), \\ R_s = \dfrac{\text{sweep flow rate}}{\text{feed flow rate}}, \quad R_p = \dfrac{\text{Permeate pressure}}{\text{Retentate pressure}} \end{array}\right) \qquad (3\text{-}5)$$

The mole fractions of each component are represented by y on the tube and shell sides. Da (the Damköhler number) represents the ratio of reaction rate and convective flow rate and Pe (the Péclet number) describes the ratio of membrane flux and convective flux. It should be noted that the diffusivity used in Pe is refers to diffusion of H_2 in the membrane, and hence this Pe is different from a gas-phase mass transfer Pe inside the

tube (which does not appear in the governing equations). The *Pe* defined here is the ratio of membrane permeance and WHSV (Weight Hourly Space Velocity, hr^{-1}), or alternatively the ratio of g_{cat} and membrane surface area. The permeance used in *Pe* is that of hydrogen, and the membrane selectivity α_i is the permeance of component *Qi* divided by the hydrogen permeance. For example, α_i is zero if the membrane does not allow propane and propylene permeation, thus corresponding to perfect H_2 selectivity. The parameter R_s represents the ratio of sweep and feed volumetric flow rates. The parameter R_p is the ratio of permeate and retentate total pressure. The above methods of non-dimensionalization are broadly consistent with those carried out in the previous PBMR modeling literature [65, 66, 161].

As discussed, I have assumed isothermal operation, no axial diffusion, and no radial dispersion. The isothermal assumption requires further analysis, since PDH is a highly endothermic reaction (ΔH = 125 $kJ.mol^{-1}$). To address this issue, I augment our model with a dimensionless 2D energy conservation along with appropriate boundary conditions:

$$\frac{\partial \theta_T}{\partial \tilde{z}} = \left(\frac{1}{Pe_{heat}}\right)\left(\frac{L}{R}\right)^2 \left\{\frac{1}{\tilde{r}}\frac{\partial}{\partial \tilde{r}}\left(\tilde{r}\frac{\partial \theta_T}{\partial \tilde{r}}\right)\right\} + \left(\frac{1}{Pe_{heat}}\right)\left\{\frac{\partial^2 \theta_T}{\partial \tilde{z}^2}\right\} + Da\frac{(-\Delta H)}{C_p T_0}(-\tilde{r}_A) \qquad \text{(Tube)} \tag{3-6}$$

$$\text{B.C.} \quad \begin{bmatrix} \tilde{z} = 0, \quad \theta_0 = 1, \quad \tilde{z} = 1, \quad \dfrac{\partial \theta_T}{\partial \tilde{z}} = 0 \\ \tilde{r} = 0, \quad \dfrac{\partial \theta_T}{\partial \tilde{r}} = 0, \quad \tilde{r} = 1, \quad \dfrac{\partial \theta_T}{\partial \tilde{r}} = \dfrac{hR}{k_{eff}}(\theta_M - \theta_T) \end{bmatrix} \tag{3-7}$$

$$\left(\alpha_{heat} = \frac{k_{eff}}{\rho C_p}, \qquad Pe_{heat} = \frac{\alpha_{heat}}{uL} \right) \tag{3-8}$$

Here θ represents dimensionless temperature which is defined by temperature divided by inlet temperature (T_0). The governing equations include thermal diffusivity (α_{heat}) and Péclet number for heat transfer as generally defined above. The k_{eff} is effective thermal conductivity, which can be obtained from Zehner-Schlünder model [162, 163]. The ρ and C_p denote average density and heat capacity respectively. The u is linear velocity along the axial direction and h is heat transfer coefficient. The Da and dimensionless reaction term in Equation S1 are the same as what I use in the mass transfer equation. For the membrane side, heat conduction across the support is considered as follows:

$$\frac{\partial}{\partial \tilde{r}}\left(\tilde{r} \frac{\partial \theta_m}{\partial \tilde{r}} \right) = 0 \qquad \text{(Membrane support)} \tag{3-9}$$

$$\text{B.C.} \qquad \begin{bmatrix} \tilde{r} = 0, & \dfrac{\partial \theta_M}{\partial \tilde{r}} = \dfrac{h\delta_m}{k_{eff}}\left(\theta_M - \theta_T\right) \\ \tilde{r} = 1, & \dfrac{\partial \theta_M}{\partial \tilde{r}} = \dfrac{h\delta_m}{k_{eff}}\left(\theta_S - \theta_M\right) \end{bmatrix} \tag{3-10}$$

I also set up a heat transfer equation for the shell side as follows:

$$\frac{\partial \theta_s}{\partial \tilde{z}} = \left(\frac{1}{Pe_{heat}} \right)\left(\frac{L}{\delta_S} \right)^2 \left\{ \frac{1}{\tilde{r}} \frac{\partial}{\partial \tilde{r}}\left(\tilde{r} \frac{\partial \theta_s}{\partial \tilde{r}} \right) \right\} \qquad \text{(Shell)} \tag{3-11}$$

$$\text{B.C.} \quad \left[\begin{array}{l} \tilde{r} = 0\,, \quad \dfrac{\partial \theta_s}{d\tilde{r}} = \dfrac{h\delta_S}{k_{gas}}\left(\theta_s - \theta_m\right), \quad \tilde{r} = 1\,, \quad \dfrac{\partial \theta_s}{\partial \tilde{r}} = 0 \ \text{(adiatatic)} \\ \tilde{r} = 1\,, \quad \dfrac{\partial \theta_s}{\partial \tilde{r}} = \dfrac{h\delta_S}{k_{gas}}\left(\theta_w - \theta_s\right), \quad \theta_w = \dfrac{T_w}{T_s} \ \text{(constant wall temperature)} \end{array} \right] \tag{3-12}$$

The subscripts *t. m* and *s* denote the tube, membrane and shell sides. For each side, the characteristic length in radial direction is the radial distance between its radial boundaries. For example, for the shell side the characteristic length (δ_s) is from the boundary between membrane support and the shell side to the outer wall of the reactor. The T_w is the constant wall temperature in non-adiabatic operation. I assume constant wall heat flux with fixed heat transfer coefficient, which is estimated based on Nusselt number in fully developed flow (Nu = 8). The average heat capacity and conductivity for the gas mixture are estimated by extrapolating gas property data provided by NIST to 600°C, and are assumed to be constant throughout the reactor. The gas density is calculated from equation of state at 1 atm and 600°C.

3.2.2. Operating window and membrane properties

As shown in the dimensionless equations, the governing relations become functions of *Pe*, *Da*, α (membrane selectivity), R_s (ratio of volumetric sweep and feed flow rates) and R_p (ratio of pressures at the tube and shell side). For fixed α, R_s, and R_p, the results can be represented by *Pe* and *Da* regardless of reactor size, thus allowing 2D 'operating window' plots for the PBMR performance. Before showing these plots, I briefly discuss a few typical results of the simulation at given *Pe* and *Da* values. **Fig. 3-1** shows the dimensionless mole flow rate of propane along the reactor with different *Da*

and *Pe*. Since *Da* relates reaction kinetics to space velocity, it determines the initial slope of the dimensionless flow rate as shown in **Fig. 3-1a**. The larger the *Da*, the faster the decrease of flow rate observed near the reactor entrance; whereas smaller *Pe* values further decrease the flow rate of propane due to membrane permeation after the initial decrease. At infinite *Pe* (*i.e.*, no membrane permeation), the equilibrium PDH conversion is reached. As seen in **Fig. 3-1b**, enhancement of conversion using the PBMR is achieved by decreasing *Pe* (*i.e.*, increasing the membrane permeation rate).

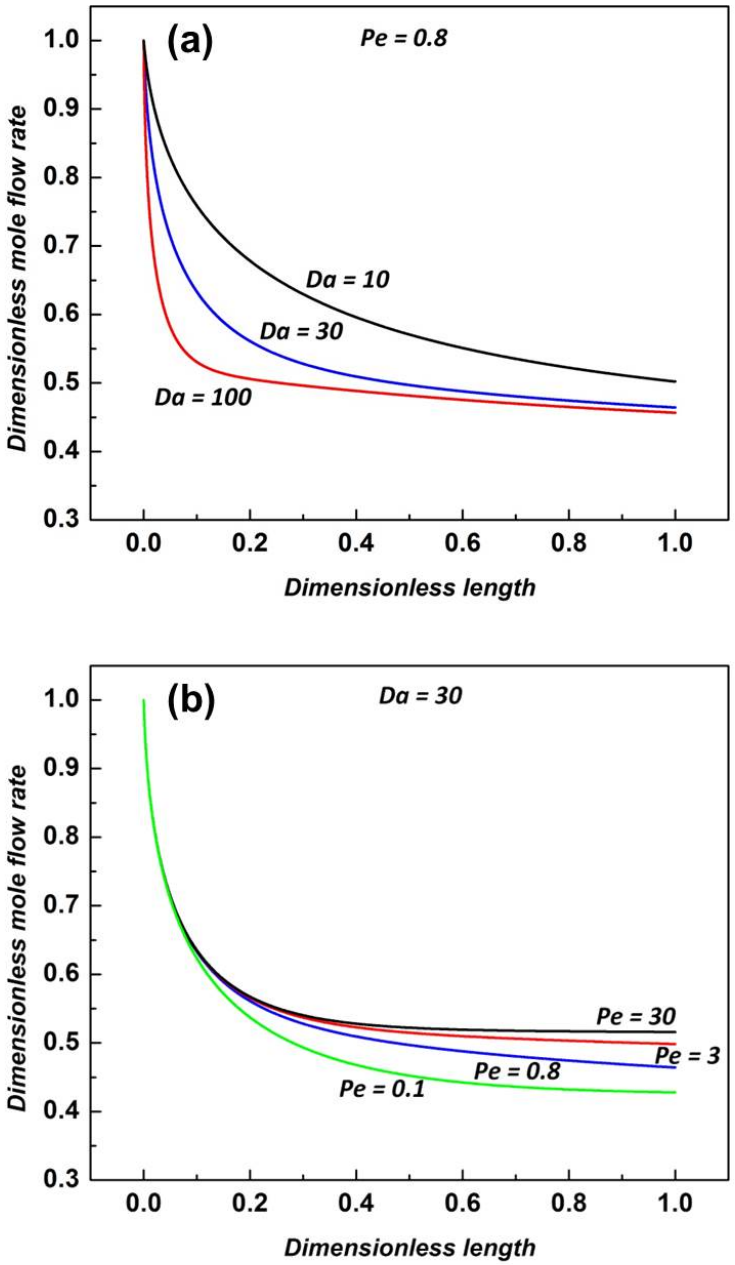

Fig. 3-1. Dimensionless propane flow rate along the reactor at fixed (a) *Pe* and (b) *Da* ($\alpha = 0$, $R_s = 1$, $R_p = 1$).

3.3. Results and discussion

3.3.1. Effect of membrane properties

Fig. 3-2 shows the operating window wherein the calculated conversions are displayed as a color-coded contour plot with respect to a wide range of *Da* and *Pe*. These results are for small-pore hydrogen-selective zeolite membranes wherein α is zero for propane and propylene. One can easily conclude that higher conversion can be achieved by increasing *Da* and lowering *Pe*. In the low-*Da* region, the system becomes kinetic-controlled while in the high-*Da* region the conversion is strongly affected by the *Pe* value in the range of 0.1 - 10. In this region membrane permeation becomes effective in breaking the equilibrium limitation. There exists a plateau region at $Da > 20$ and $Pe < 0.1$ in which there is no further conversion enhancement. This behavior is due to the decreasing membrane permeation along the reactor length. Although enhanced membrane permeation lowers *Pe*, it also increases the shell-side hydrogen concentration and thus decreases the permeation driving force (the partial pressure difference of H_2 between the tube and shell sides) as the feed flow proceeds down the reactor length. Increasing the membrane permeation assists enhancement near the reactor inlet, but eventually the differences in mole fraction between the tube and the shell side become small, and there is little membrane permeation downstream as shown in **Fig. 3-3**. This highlights an important fact that the degree of enhancement in the PBMR will be limited unless other factors such as feed composition, sweep flow rate (R_s), or operating configuration itself, are changed. I discuss this further in the next section.

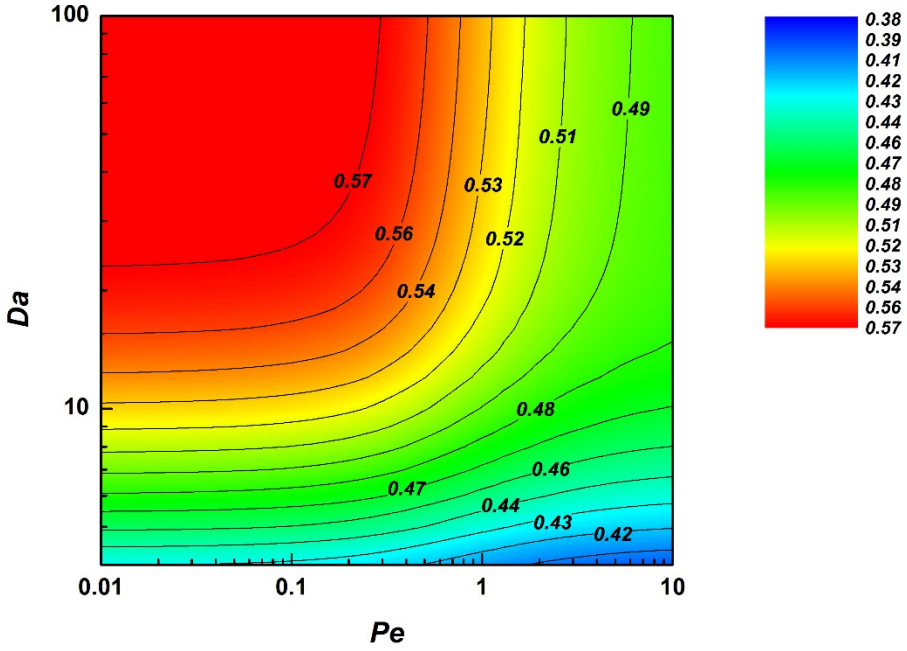

Fig. 3-2. Operating window for PDH PBMRs using hydrogen-selective membranes (α = 0, R_s =1, R_p =1). The color scale depicts the PBMR conversion.

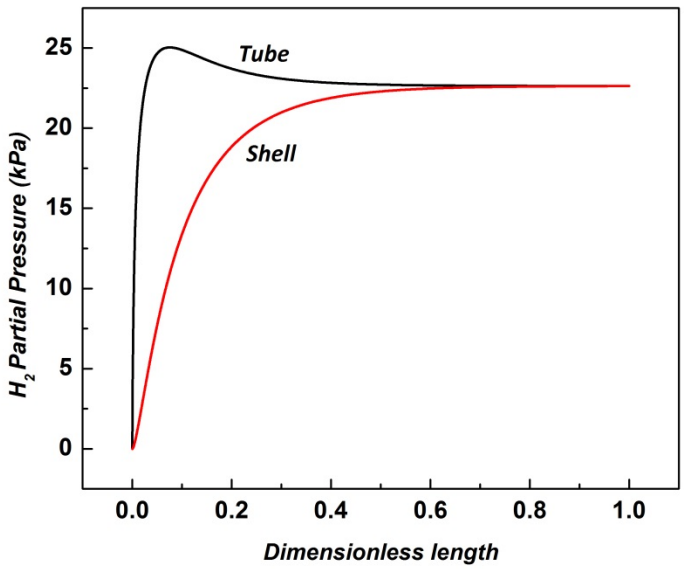

Fig. 3-3. Partial pressure profiles of hydrogen along the PBMR length at the tube and the shell sides, with Pe = 0.1 and Da = 80 (α = 0, R_s =1, R_p =1).

I also consider other types of membranes, as mentioned earlier. The most commonly used large-pore ceramic membranes follow Knudsen diffusion due to their relatively large pore size (2-200 nm). The Knudsen selectivity is determined by the square root of the ratio of the component molecular weights. The H_2/C_3H_8 and H_2/C_3H_6 selectivities are about 4.7 and hence α is about 0.2 for both the olefin and paraffin. For medium-pore zeolite membranes such as MFI, α is about 0.1 for both the olefin and paraffin [110, 164, 165]. **Fig. 3-4** shows the operating windows for these two values of α. Both windows are calculated with the same assumptions as for the hydrogen-selective membranes. It is found that there exist 'non-operating regions', which are shown in gray color. The boundary lines between the operating and non-operating regions represent

'depletion line' of propane, which is zero flow rate of propane on the retentate (tube) side. This condition occurs when all the propane feed gas is consumed by membrane permeation and catalytic reaction. Hence, the calculated conversions in the non-operating region are not physically meaningful.

Fig. 3-4 also indicates narrower operating regions for medium-pore and larger-pore membranes. It should be noted that if the propane is completely consumed in a certain length of the reactor, the propane on the shell side can back-permeate to the tube side in the remaining downstream length. However, this is not considered here since such a reactor operation condition is not practical. Compared to the case of hydrogen-selective membranes, the operating windows in **Fig. 3-4** do not show a plateau region. Instead there exist maximum values of the conversion at each *Da*. Although low values of *Pe* generally enhance conversion, the propane reactant also permeates through the membrane thus forcing the equilibrium backwards. Hence there is a trade-off between reactant and product permeation. The trends seen in **Fig. 3-2** and **Fig. 3-4** for PDH are consistent with those seen in Harold et al. for cyclohexane dehydrogenation.[65] In that work, it was shown that there exist optimum ratios of permeation and reaction rates for certain values of membrane selectivities. Furthermore, for an infinitely hydrogen-selective membrane, the cyclohexane conversion reached a plateau with increasing permeation rate. Here I have examined this trend in the context of PDH for a much wider range of *Da* (ratio of reaction rate and convective transport rate), so that I can clearly identify the optimum value of *Pe* at each *Da* of practical interest. Among the different types of membranes, hydrogen-selective membranes show the best performance since they allow negligible permeation of the propane reactant, even though they also retain the propylene product on

the tube side. Hence, membranes made of small-pore zeolites such as DDR or SAPO-34 are likely the best candidates for PDH PBMR applications, but medium-pore zeolite or larger-pore Knudsen-selective membranes also show some level of enhancement. In order to apply Knudsen selective membranes one should consider the reactant/product permeation trade-off and the narrower operating region allowed.

Using the definitions of *Pe* and *Da* and assigning reactor dimensions (*e.g.*, R_1 = 0.35 cm and L = 10 cm, which are typical dimensions of ceramic tubes used for PDH PBMRs), I can extract dimensional process variables such as the WHSV (hr^{-1}) and the membrane permeance ($mol.s^{-1}.m^{-2}.Pa^{-1}$), which are two important parameters for PBMR application. Using **Fig. 3-5**, I can deduce the range of WHSV and membrane permeance required for a target conversion. For example, 55% PDH conversion can be obtained using small-pore zeolite membranes with a required permeance range of $2–6 \times 10^{-7}$ $mol.s^{-1}.m^{-2}.Pa^{-1}$ if the PBMR is operated at WHSV 1–1.5 hr^{-1}. This H_2 permeance can be achieved by fabricating membranes about 1 μm thin, considering that the previously reported H_2 permeance range of SAPO-34 and DDR membranes is about 5×10^{-8} $mol.s^{-1}.m^{-2}.Pa^{-1}$ with 5-10 μm thickness[95, 166]. This type of information is important for PBMR evaluation, and for appropriate material selection or design.

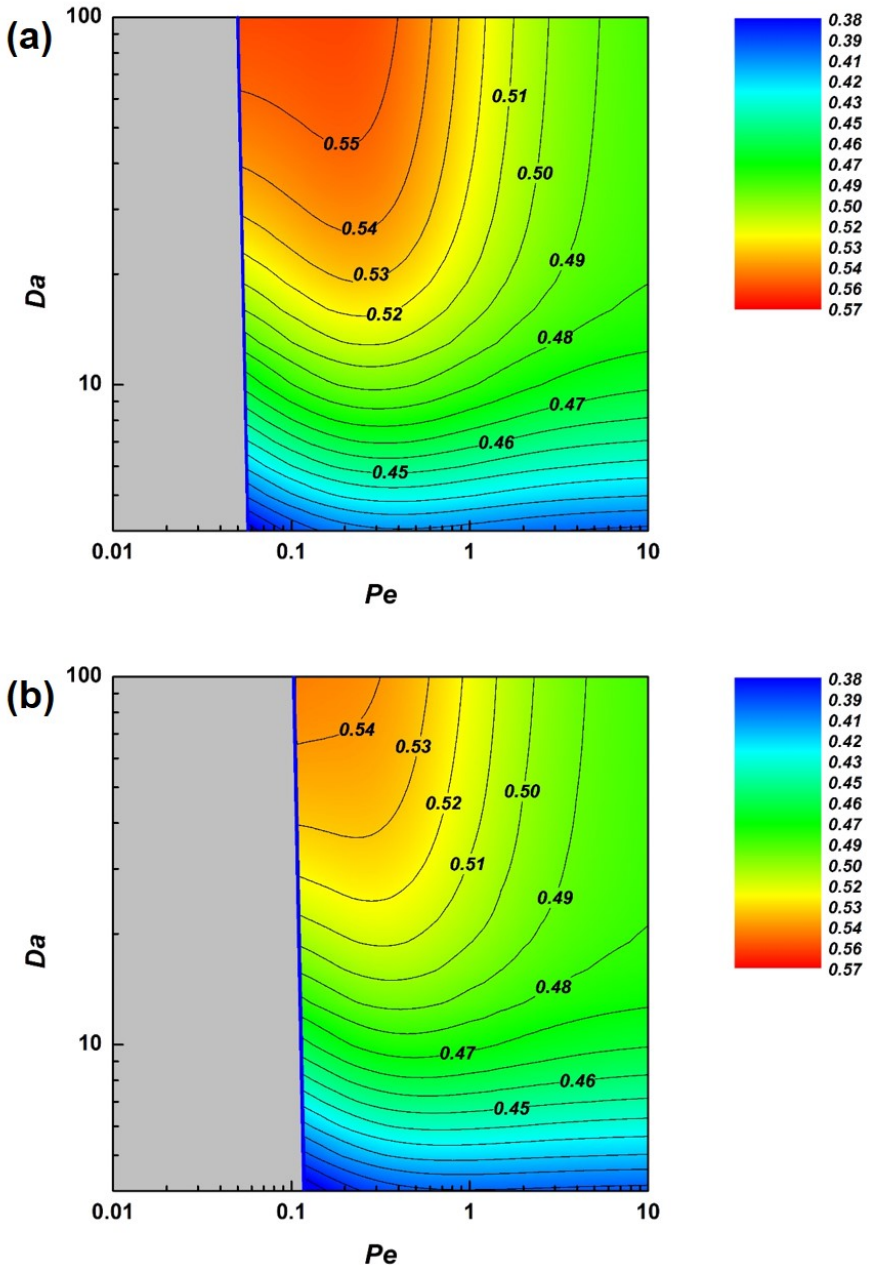

Fig. 3-4. Operating windows for PDH PBMRs using (a) medium-pore (α = 0.1) and (b) large-pore (Knudsen, α = 0.2) membranes. The 'non-operating' regions are shaded in grey. The color scale depicts the PBMR conversion.

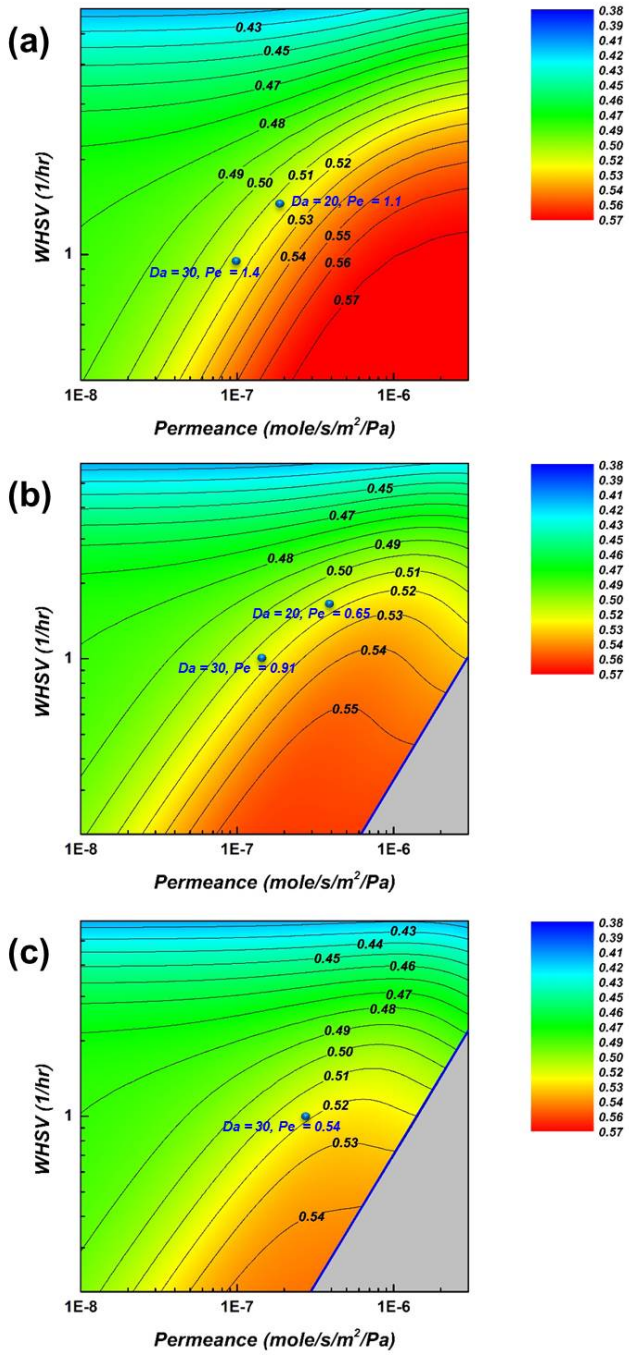

Fig. 3-5. Operating windows for PDH PBMRs using membrane permeance and WHSV for (a) small-pore (α = 0), (b) medium-pore (α = 0.1), and (c) Knudsen (α = 0.2) membranes (R_1=0.0035 m, L=0.1 m). The color scale depicts the PBMR conversion.

3.3.2. Effect of operating conditions: sweep flow rate, pressure

As discussed in the previous section, the PBMR shows a plateau region in which there is no further conversion enhancement. This is because of the increase in hydrogen concentration at the shell side due to membrane permeation, thereby decreasing the driving force for further permeation. A simple way of overcoming this limitation is to increase the sweep flow rate in order to decrease the mole fraction of hydrogen in the permeate and hence allow more membrane permeation for the same *Pe*. This is represented in **Fig. 3-6** using a sweep flow rate of R_s = 3, three times larger than the calculations shown above. The other parameters are the same as in the previous case of hydrogen-selective membranes. In **Fig. 3-6**, conversion increases significantly to a plateau of 66% as compared to 57% in the case of R_s = 1. However, the conversion enhancement by increasing the sweep flow rate should be weighed appropriately against the increase in the operating cost of the PBMR.

The total pressures of both the tube and shell side are maintained at 1 atm (R_p = 1), primarily because the equilibrium conversion of the dehydrogenation reaction decreases with increasing pressure. The driving forces for membrane permeation are the partial pressure differentials of each component between the tube and shell side, rather than the total pressure differential across the membrane. However, the membrane fluxes would be increased by using a higher total pressure at the tube side or lowering the pressure at the shell side. Gokhale et al. have discussed the effect of pressure ratio on isobutane dehydrogenation in a PBMR, and showed a conversion increase with decreasing pressure ratio[66]. However, this trend is only valid if the total pressure at the shell side is decreased while the tube pressure is maintained at 1 atm. Pressurizing the feed (tube) side

will lead to decrease conversion with decreasing pressure ratio, which is opposite to Gokhale et al. even with the same pressure ratio. There will be more increase in product concentrations than that of the reactant, leading to an equilibrium shift to the reactant side. In large-scale PDH processes, applying a vacuum on the permeate side is not considered cost-effective. *Pe* decreases and *Da* increases with increasing total pressure at the tube side, but the reverse reaction in the dimensionless reaction term will be increased as well, which is not favorable for conversion. **Fig. 3-7** shows the operating window at a larger tube pressure (3 atm, R_p = 0.33) with the shell side at 1 atm, and it clearly indicates that the equilibrium shift away from the products is more significant than increased membrane permeation. Therefore, I consider atmospheric-pressure operation as the most practical case in this study.

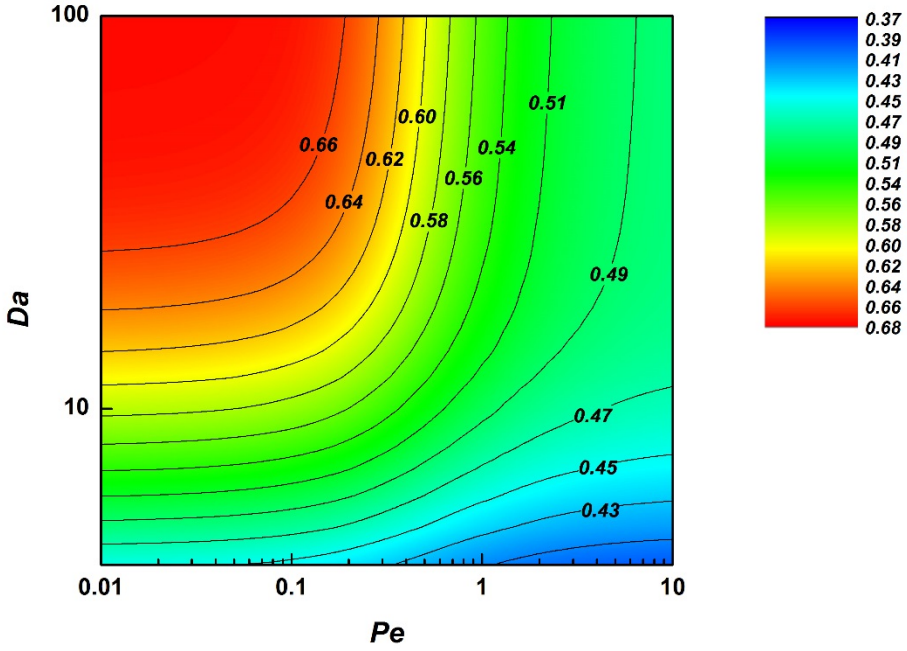

Fig. 3-6. Operating window for PDH PBMRs using hydrogen-selective membranes with a large sweep flow rate, corresponding to parameters $\alpha = 0$, $R_s = 3$, $R_p = 1$. The color scale depicts the PBMR conversion.

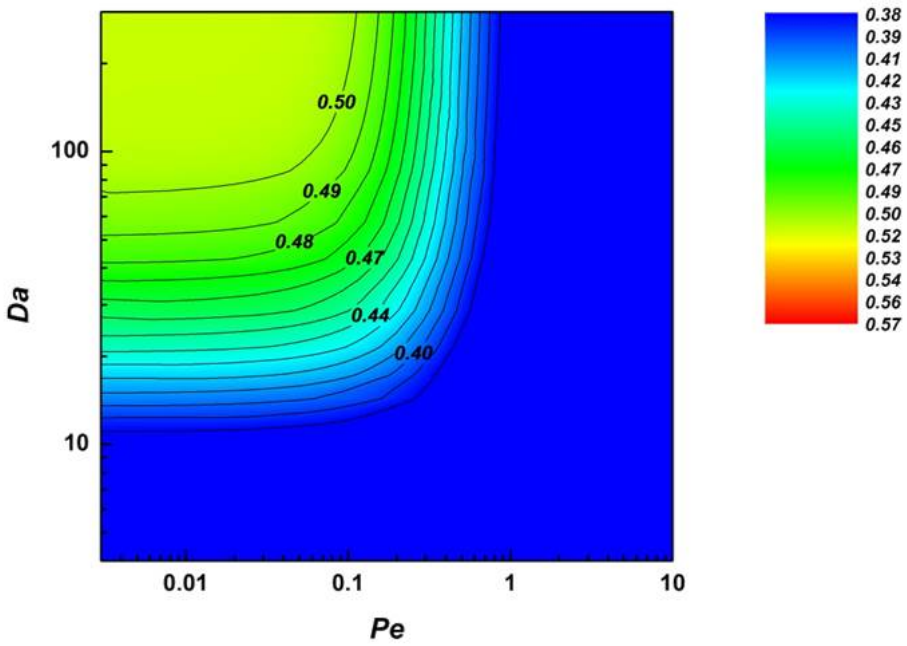

Fig. 3-7. Operating window for PDH PBMRs using hydrogen-selective membranes with a large pressure at tube (3 atm, R_p = 0.33), corresponding to parameters α = 0, R_s =1. The color scale depicts the PBMR conversion.

3.3.3. Counter-current operation

The results presented in the foregoing sections all assumed a co-flow sweep gas mode. Another potential way of enhancing PBMR performance is the use of a counter-current sweep gas mode. In the counter-flow case, the governing equation remains the same for the tube side. For the shell side, the flow direction is reversed and the governing equation is slightly modified:

$$-\frac{d\left(\tilde{v}_s y_s\right)}{d\tilde{z}} = \frac{1}{Pe}.\frac{\alpha}{R_s}\left(y_t - y_s\right) \qquad \text{(Shell)} \qquad (3\text{-}13)$$

The variables on the shell side are unknown at the reactor entrance ($z = 0$), so the simulations are repeated with different assumed values at the entrance, and iterated until the known sweep gas conditions at the exit ($z = 1$) are achieved. Then the operating window for countercurrent mode can be drawn as shown in **Fig. 3-8** for both medium-pore ($\alpha = 0.1$) and hydrogen-selective ($\alpha = 0$) membranes, and can be compared to the cocurrent mode (**Fig. 3-2** and **Fig. 3-4**). It is seen that the depletion line of propane for medium-pore membranes still remains in the case of countercurrent operation. There is a very strong dependence of conversion on *Da* near the depletion line since the depletion of propane due to membrane permeation is also strongly affected by the feed flow rate. The difference in conversion between counter-current and co-current modes is shown in **Fig. 3-9**. The co-current mode shows better performance for most of the range of operating conditions, as can be seen in **Fig. 3-9**. Only at high *Da* and low *Pe* does the counter-current mode overcome the plateau region seen in the co-current mode. Unlike the co-current mode, continuous membrane permeation along the reactor length can be achieved by using countercurrent mode as shown in **Fig. 3-10**. However, although the counter-current sweep gas decreases the hydrogen concentration more effectively near the sweep gas entrance ($z = 1$), there is also a back-permeation of hydrogen from the shell to the tube side near the feed gas entrance due to higher partial pressure in the shell side (**Fig. 3-10**), thereby decreasing the MR conversion. It was believed that the counter-current sweep mode better eliminates gas concentrations in the shell side, similar to the countercurrent heat exchanger concept. Gallucci et al. showed modeling results at a

particular operating condition, wherein continuous hydrogen permeation along the reactor is observed [73]. This is consistent with **Fig. 3-10**, but in terms of the PBMR performance a significantly higher conversion with counter-current sweep can be only achieved in a limited operating range of high *Da* (~ 100) and low *Pe* (~ 0.1). **Fig. 3-11** shows the difference of dimensionless propane flow rate between cocurrent and counter-current sweep gas modes, with *Pe* and *Da* indicated. In **Fig. 3-11a**, a smaller decrease in flow rate is observed at *Pe* = 0.1 and *Da* = 20 for the countercurrent mode near the feed gas entrance, due to hydrogen back-permeation in that region. However, there is a greater propane flow decrease in countercurrent mode near the reactor exit, which is because of the effective removal of hydrogen. When *Pe* drops to =0.01, I observe more decrease in propane flow rate in counter-current than the concurrent mode. However, at *Da* = 20, the more effective hydrogen removal still cannot overcome the effect of hydrogen back-permeation and shows a smaller decrease of propane feed flow rate overall, thus ending up with a lower conversion. On the other hand, **Fig. 3-11b** shows that for *Pe* = 0.1 and *Da* = 80, the hydrogen back-permeation still exists but the countercurrent hydrogen removal overcomes this negative effect and attains a higher conversion. It should be mentioned that further decreasing *Pe*, *e.g.*, to 0.02 as shown in **Fig. 3-11b**, leads to lower conversion since it further increases the hydrogen back-permeation. In summary, a high *Da* is always necessary for the counter-current mode since the reaction kinetics should be fast enough to compensate for the negative effect of hydrogen back-permeation. A low *Pe* is also required for effective hydrogen removal, but a *Pe* that is too low will cause undesired hydrogen back-permeation. Therefore, a trade-off relation exists between effective hydrogen removal and its own back permeation. Compared to the co-current

mode, the operating window for the counter-current mode shows considerable sensitivity to process conditions for $Pe < 0.1$, which implies there could be difficulties in process control of the counter-current PBMR. However, it still suggests a possibility of enhancing PBMR performance by simply changing the direction of sweep flow, which does not increase the operating cost significantly.

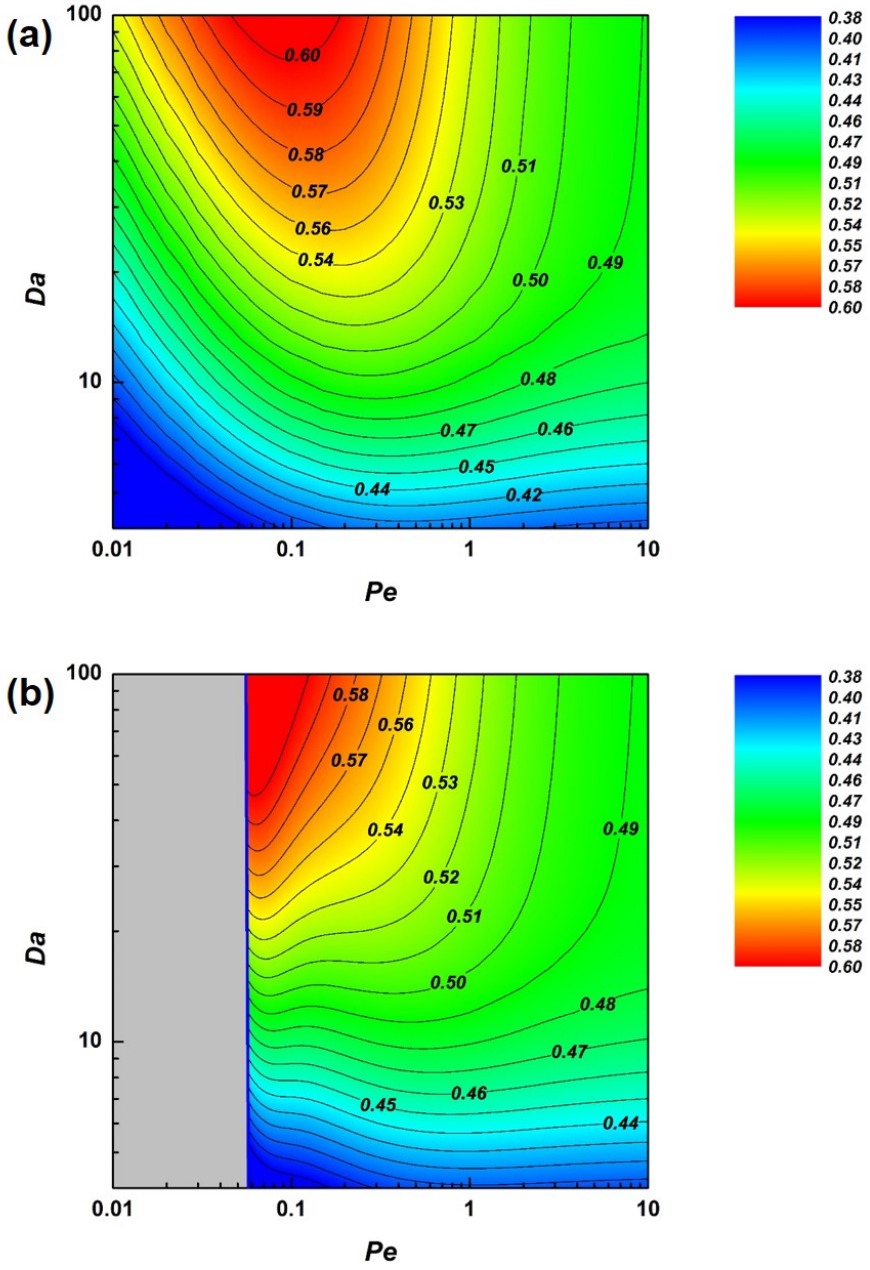

Fig. 3-8. Operating windows for PDH PBMRs using (a) hydrogen-selective (α = 0) and (b) medium-pore (α = 0.1) membranes in counter-current sweep gas mode. The color scale depicts the PBMR conversion.

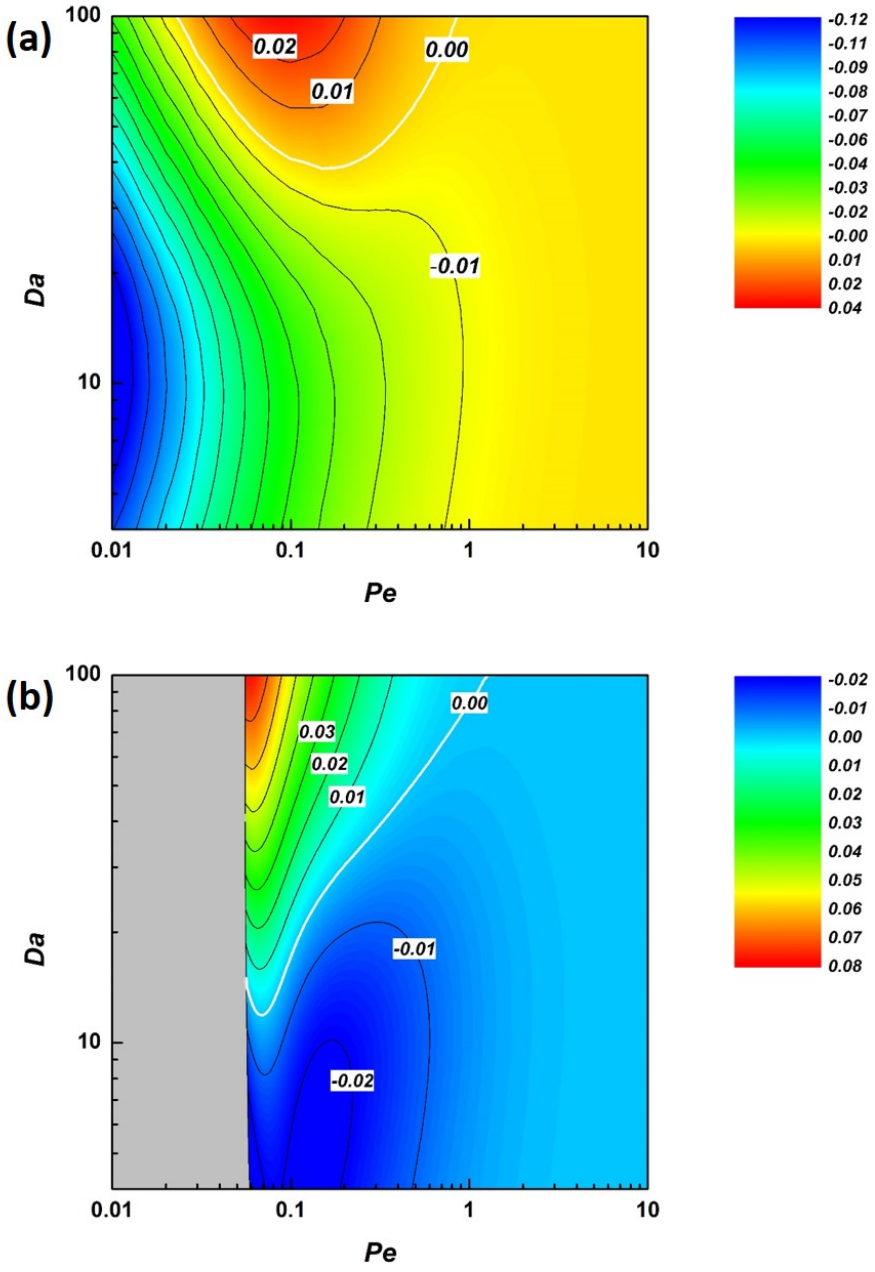

Fig. 3-9. Difference in PBMR conversion between counter-current and co-current sweep gas modes for (a) hydrogen-selective (α = 0) and (b) medium-pore (α = 0.1) membranes. The color scale depicts the PBMR conversion.

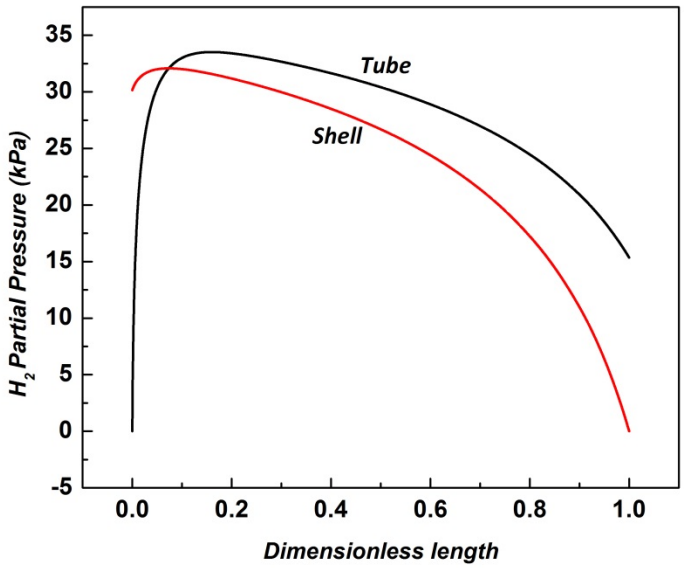

Fig. 3-10. Partial pressure profiles of hydrogen along the reactor length at the tube and the shell side in counter-current sweep gas mode using hydrogen-selective (α = 0) membranes (*Pe* =0.1 and *Da* = 80).

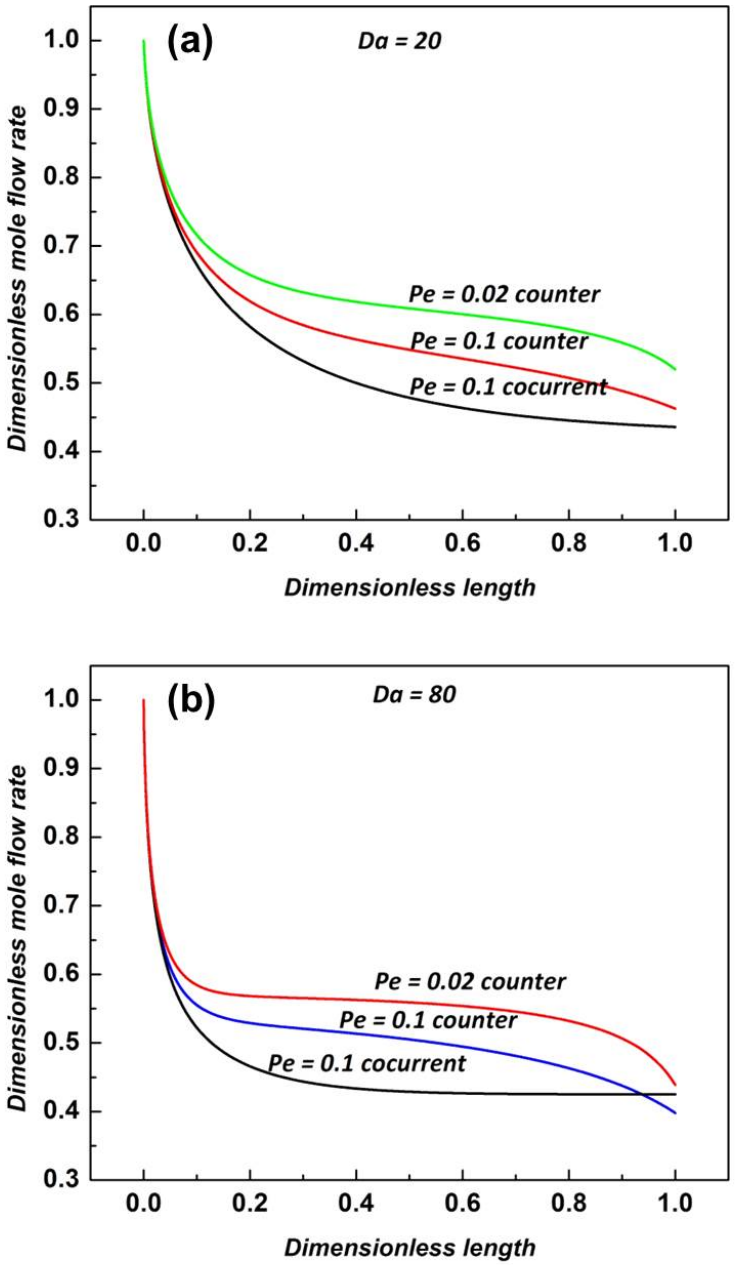

Fig. 3-11. Dimensionless propane flow rates for cocurrent and countercurrent sweep modes using hydrogen-selective ($\alpha = 0$) membranes, with (a) $Da = 20$, and (b) $Da = 80$.

3.3.4. Shell side catalyst

In this section I consider another PBMR configuration, in which the packed catalyst bed is placed on the shell side and permeate gases are collected in the membrane tubes. The governing equations are slightly modified, and I employ one more parameter, which is the number of membrane tubes (n) for a given amount of shell-side catalyst. The dimensionless governing equations remain the same, but the definition of *Pe* changes when considering permeation through n tubes. Assuming the same total volumetric flow rate and g_{cat}, and the same radius of membrane tubes (R_1), the *Pe* for a PBMR using n tubes can be defined as

$$Pe = \frac{v_{t0}}{Q_{H_2} R_g T} \frac{R_1}{2L} \frac{1}{n} \tag{3-14}$$

The definition of *Da* remains unchanged. The operating windows shown in previous Fig.s do not change, since the same governing equations still apply. However, I can now alter the value of *Pe* by changing the value of n. As I increase n, the resulting lower *Pe* allows an increased conversion over the case of tube-side catalyst, for the same operating conditions and membrane properties. For example, if *Da* = 20 and *Pe* = 4, I expect to obtain about 49% conversion with a tube-side catalyst (**Fig. 3-2**). For given reactor dimensions (R_1 = 0.0035 m, L = 0.1 m), the required WHSV is 1.5 hr^{-1} and the membrane permeance is 8×10^{-8} $mol.s^{-1}.m^{-2}.Pa^{-1}$. However, if 5 tubes are used with a shell-side catalyst, *Pe* becomes 0.8 and the conversion increases to 53% with the same membrane properties. This implies the potential of using multiple tubes in one unit if a membrane with a large permeance is not available. The *Pe* and *Da* can be defined using

more familiar operating and material parameters such as WHSV and permeance:

$$Pe = \frac{1}{P_{total}(mw_{feed})3600}\frac{WHSV}{Q_{H_2}}\frac{g_{cat}}{n2\pi R_1 L} \tag{3-15}$$

$$Da = P_{total}(mw_{feed})3600\frac{k_1}{WHSV} \tag{3-16}$$

Here, P_{total} is the tube-side total pressure, mw_{feed} (g.mol^{-1}) is the molecular weight of the feed flow and 3600 (s) is used for conversion to hourly flow rate. Since *Pe* includes the ratio of g_{cat} and membrane surface area, adding more tubes will increase the total membrane surface area, which leads to a lower *Pe*. For a certain conversion, the required *Pe* is determined at each *Da*, and the required ratio of g_{cat} and membrane surface area can then be calculated for a specific catalyst, membrane, and desired WHSV. Since g_{cat} is proportional to the shell side volume, I can derive a characteristic length scale (λ) for the PBMR with multiple tubes as follows:

$$\lambda \propto \frac{R_2^{\,2} - nR_1^{\,2}}{nR_1} \tag{3-17}$$

Here, R_1 and R_2 are the radii of the membrane tubes and whole reactor vessel surrounding the shell-side catalyst respectively. With increasing *n*, λ decreases and leads to greater surface area relative to the total tube volume. Since higher conversion corresponds to smaller *Pe*, a smaller characteristic length to enhance the performance. This suggests the use of closely-packed multiple membrane tubes or ceramic hollow-fiber tubes (which are currently available) as options for scale-up of PDH PBMRs.

3.3.5. Required membrane properties for a target conversion

The operating windows can be used for specifying the required membrane properties, catalyst properties, or reactor conditions to obtain a target conversion. Since conventional PDH PBRs in commercial use operate with well-optimized catalysts, I focus on membrane properties in this paper. If the reactor dimensions and catalyst for PDH are already determined, I can design the required membrane properties based upon the operating windows. For example, I assume a concurrent PBMR conversion of 52% at 600°C as a moderate but significant target (about 10% enhancement from the equilibrium conversion of 48% with a pure propane feed). **Table 3-2** shows the maximum *Pe* at three different values of *Da* to obtain the target conversion. These specific *Pe* and *Da* values are also superimposed in **Fig. 3-5**. It should be noted that the permeances on the *x*-axis of **Fig. 3-5** are chosen to be in the range achievable with current membrane fabrication technology (also see discussion below). Thus the *Pe*, *Da* combinations highlighted in **Fig. 3-5** represent technologically feasible conditions. If the same reactor conditions and kinetics for the Pt-Sn catalyst are applied, the minimum required permeances of different types of membranes are calculated at each WHSV. One finds that the medium-pore (α = 0.1) or Knudsen (α = 0.2) membranes require more permeance than hydrogen selective membranes (α = 0) to obtain the target conversion. The membrane permeance already includes the effect of thickness, so the required permeance can be achieved both by appropriate material selection and by controlling the membrane thickness. Considering that the high-temperature H_2 permeance range of zeolite membranes is 10^{-8}-10^{-6} mol.s^{-1}.m^{-2}.Pa^{-1} for an approximately 1-5 micron thickness range [95, 97, 166], it appears that the required properties can be achieved for the target conversion at low WHSV < 1 hr^{-1}.

However, if a larger WHSV (> 2 hr^{-1}) is used, medium-pore or Knudsen membranes will not be recommended since they cannot achieve the target conversion (**Table 3-1**).

Fig. 3-12 shows the minimum permeances required for the three types of membranes in the WHSV range 0.1-5 hr^{-1} for two different conversions. Medium-pore membranes such as MFI can be still used for WHSVs up to about 1.8 $hr^{-1}$for a 52% conversion. However, if the target conversion is 54% the possible operating range of WHSV become significantly narrower especially for medium-pore and Knudsen membranes as described in **Fig. 3-12**b. Small-pore membranes (*e.g.*, SAPO-34), require relatively moderate membrane permeance for WHSV up to 2 hr^{-1}, which can be achieved by fabrication of membranes of < 2 micron thickness. At higher WHSVs, permeances higher than 10^{-6} $mol.s^{-1}.m^{-2}.Pa^{-1}$ are required. This result implies that reducing zeolite membrane thickness to the sub-micron regime while controlling membrane defects is an important opportunity and challenge for PBMR applications. Recent developments in hydrothermal zeolite membrane synthesis[167], as well as fabrication of ultra-thin membranes from 2D zeolite materials[168], offer useful directions for the pursuit of membrane thickness reduction.

Table 3-1. Required *Pe* and membrane permeances (in $mol.s^{-1}.m^{-2}.Pa^{-1}$) at different fixed *Da* (and hence WHSV) values, for a target 52 % PBMR conversion (R_1=0.0035 m, L=0.1 m). *n.a.*: not achievable.

	Da=30 (WHSV=0.95)			*Da*=20 (WHSV=1.43)			*Da*=10 (WHSV=2.87)		
	$\alpha = 0$	$\alpha = 0.1$	$\alpha = 0.2$	$\alpha = 0$	$\alpha = 0.1$	$\alpha = 0.2$	$\alpha = 0$	$\alpha = 0.1$	$\alpha = 0.2$
Pe	1.38	0.91	0.54	1.12	0.65	*n.a.*	0.24	*n.a.*	*n.a.*
Q ($\times 10^{-7}$)	0.96	1.6	2.8	1.8	3.7	*n.a.*	16	*n.a.*	*n.a.*

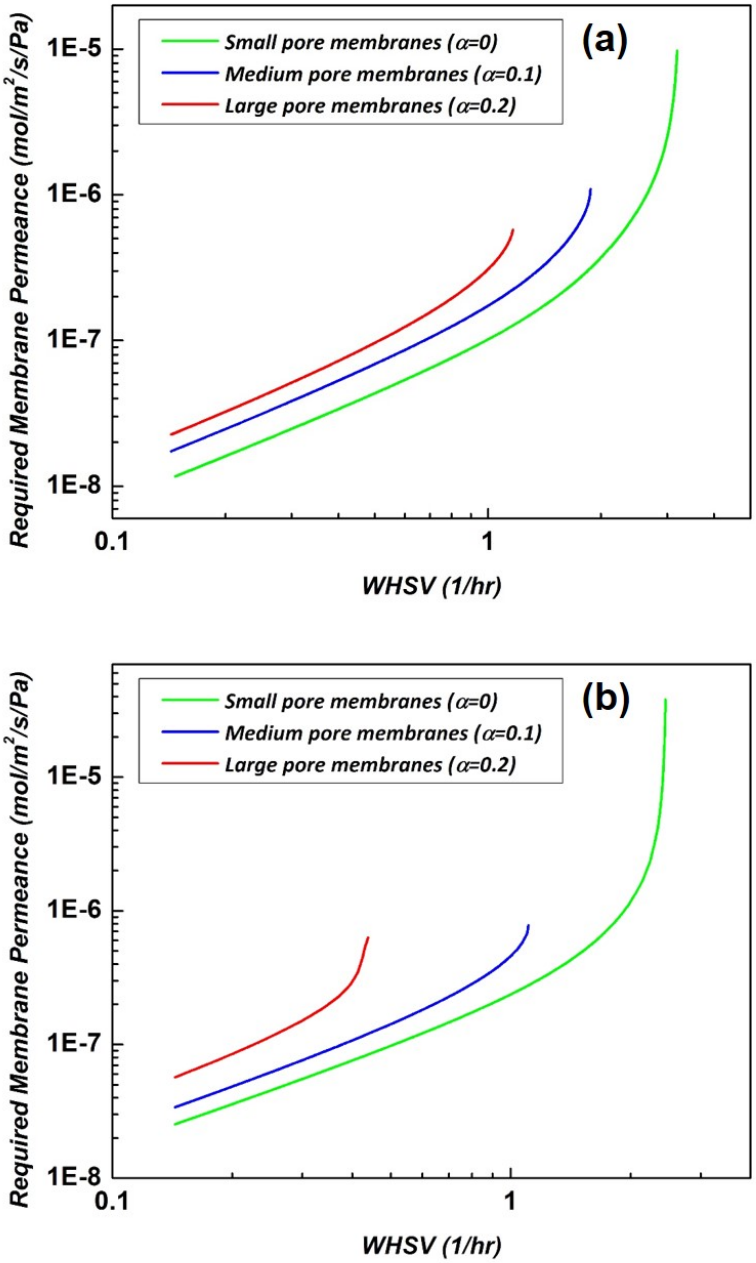

Fig. 3-12. Required membrane permeances for targeted conversions of (a) 52% and (b) 54%, in PBMRs using all three types of membranes.

3.3.6. Effect of simplifying assumptions

The mass and heat transfer equations are coupled and solved simultaneously, using realistic values for the heat transfer parameters (Supplementary Information) and the same PBMR dimensions as used in **Table 3-2**. The PBMR performance now cannot be understood solely as a function of *Pe* and *Da*, but is also a function of the heat transfer parameters (whose numerical values are listed in the Supplementary Information). Moon and Park previously studied non-isothermal conditions for cyclohexane dehydrogenation [161]. However, parabolic temperature profiles were assumed along the reactor, with a maximum temperature of 493 K at the reactor axis. These assumptions clearly are not valid in PDH. Considering the fact that there are several different heat supply options, such as non-adiabatic heat supply from the outer wall or adiabatic operation with different preheating temperatures, there will be different types of operating windows. Here, I illustrate the validity of our initial simplifying assumptions using the operating windows shown in **Fig. 3-13** for non-adiabatic and adiabatic operation. It is seen that non-isothermal operation (involving axial and radial temperature variations) shifts the conversion to lower values, but the qualitative trends remain the same over the range of practically useful *Da* and *Pe*. At small *Da*, the performance is mainly affected by *Da* since the system is kinetically controlled. However, *Pe* comes into effect after the system reaches equilibrium-limited conditions. It is worth mentioning that the region of $Da < 10$ (where large temperature drops are observed) shows almost no effect of *Pe*, and thus membrane permeation would not be useful. To avoid these conditions, a higher preheating temperature or higher wall temperature would typically be used. Finally, the mass dispersion assumptions can be examined using the axial and radial mass transfer

Péclet numbers. Although the Péclet numbers depend on the mass dispersion coefficients which are not precisely known for the PDH PBMR, I can estimate that for a PDH PBMR tube of length ~1 m operated at a typical WHSV of 1-10 hr^{-1} at 600°C, the axial mass transfer *Pe* would typically be >>1 and is not expected to have a significant effect. On the other hand, the radial *Pe* should be much smaller than the axial *Pe* in order to avoid the deleterious effects of external mass transfer resistance on the permeation rate. For PBMR tubes with $R_1/L \sim 10^{-2}$ as considered in this work, and for hollow-fiber PBMRs of even smaller radius, the effects of radial dispersion can be reasonably expected to be small. Overall, the simplified 1D isothermal PDH PBMR model provides useful design guidelines for membrane material selection and operating conditions.

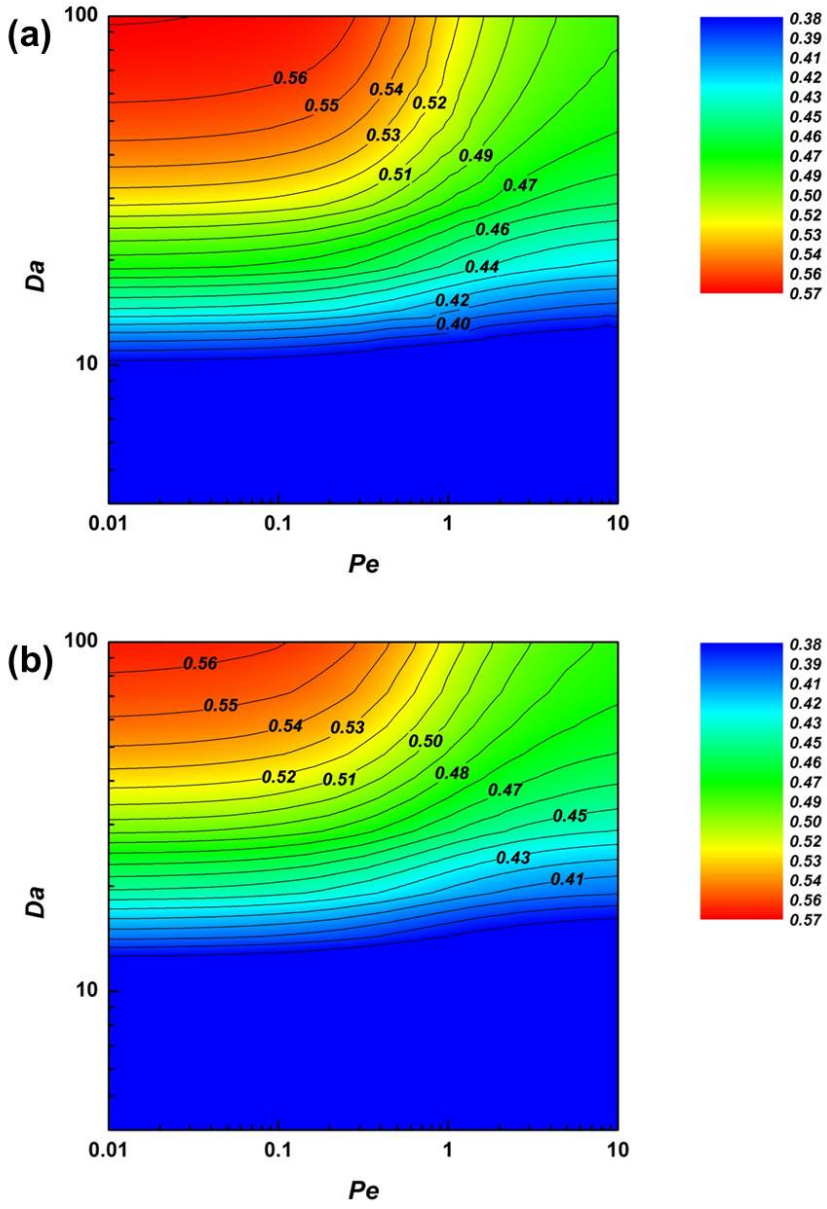

Fig. 3-13. Operating window for PDH PBMRs using hydrogen-selective membranes with non-isothermal conditions of (a) non-adiabatic heat supply with fixed wall temperature (T_w = 600 °C) and (b) adiabatic operation, corresponding to parameters α = 0, R_s =1, R_p =1. The color scale depicts the PBMR conversion.

3.5. Conclusions

I have considered the 'operating windows' of packed-bed membrane reactors (PBMRs) for propane dehydrogenation (PDH) applications are considered. Using a relatively simple isothermal model to set up dimensionless governing variables, I plotted and compared the operating ranges and reactor conversions for different types of membranes. Medium-pore zeolite and Knudsen-selective membranes show complex trends with *Pe*, whereas hydrogen-selective small-pore zeolite membranes show a plateau region of conversion at low *Pe*. This limitation can be overcome with different sweep gas operations, *i.e.*, larger sweep flow rate and countercurrent sweep gas mode. Obviously, a large sweep flow rate leads to more membrane permeation and thus increases conversion. However, use of the countercurrent sweep mode is more complicated since it has a trade-off relation between forward permeation and back-permeation of hydrogen, and it shows sensitivity to process conditions. I also consider another type of PBMR configuration, which is the use of shell-side catalyst. This is predicted to show better performance than a PBMR with a tube-side catalyst, as *Pe* can now be adjusted by altering the number of membrane tubes that collect the permeate. As far as the membrane material selection is concerned, small-pore zeolite membranes would be preferred over medium-pore and Knudsen membranes, since they provide a wider range of WHSV for the PBMR operation to achieve a target conversion. However, they have a lower permeability due to their small (< 0.4 nm) pores, and hence require reliable fabrication in the form of micron-thin or submicron membranes. Although hydrogen-selective small-pore membranes are preferred, the medium-pore and Knudsen membranes do provide moderate enhancement of PBMR performance at low WSHV < 1 hr^{-1}. The non-

isothermal operating windows show a shift of conversion to lower values especially at small *Da* where heat supply is poor; however, the general trends of PBMR performance remain the same. Our consideration of the PDH PBMR in terms of operating windows thus provides useful guidelines for overall design of the PBMR system as well as for selection and design of appropriate membrane materials and fabrication processes. This method should also be easily transferrable for other dehydrogenation reactions (*e.g.*, ethane and *iso*-butane).

CHAPTER 4

DESIGN AND PROCESS SIMULATION OF A PACKED BED MEMBRANE REACTOR SYSTEM FOR PROPANE DEHYDROGENATION

4.1. Introduction

There is considerable interest in modeling studies on membrane reactors to investigate their performance and provide useful information for selecting optimal operating configurations and membrane properties. Such works initially focused on applying simple one-dimensional (1D) isothermal models. Wu et al. used 1D isothermal model for ethylbenzene dehydrogenation in membrane reactors using ceramic membranes [63]. Tsai et al. conducted 1D non-isothermal modeling studies for partial oxidation of methane and studied temperature profiles in adiabatic operating conditions [67]. They used a 1D model inside the tube and the shell along the axial direction and included radial thermal effects from the membrane [67]. Similar work was done by Harold and Lee for a disk-type catalytic membrane reactor for ethylene oxidation [169]. Although the 1D isothermal model does not consider potentially important issues such as mass dispersion or temperature variations, it can still be widely applied in membrane reactor evaluation, especially for laboratory-scale reactors [64, 105, 170, 171]. More detailed two-dimensional (2D) and non-isothermal models were developed by several

research groups [70, 71, 172, 173]. Gobina et al. applied a 2D isothermal membrane reactor model for ethylbenzene dehydrogenation and compared the performance of reactors that used Pd-Ag membranes and microporous ceramic membranes [172]. Koukou used a 2D isothermal membrane reactor model to evaluate the dispersion effect with low and high H_2 permeability membranes for cyclohexane dehydrogenation [70].

However, very little work has been reported in the literature on modeling of scaled-up PBMR systems integrated with downstream separation processes such as sweep gas removal and the C_3 splitter for separation of propylene from propane. Such a model is important for understanding of the overall viability of a chemical production process that incorporates a membrane reactor system. At the reactor level, I describe the PBMR system using a detailed 2D non-isothermal model and examine the mass dispersion effects and temperature drop in the endothermic PDH reaction. The study also includes the thermal effects from high temperature sweep gas in a series of reactors with inter-stage heaters. I compare different membrane supports such as conventional ceramic supports versus hollow fiber supports. The required size of the PBMR is calculated for a target propylene production and better PBMR configurations are considered to overcome the limitations of conventional PBRs. At the process level, I incorporate the 2D PBMR PDH model into an ASPEN-FORTRAN simulation including downstream separation. In this Chapter, I focus on determining the advantages of using a PBMR system in a large-scale PDH plant. I compare the energy load between PBR and PBMR in non-recycled and recycled configuration and elucidate the effect of enhancement of PDH conversion and selectivity on the downstream separation. The ASPEN-FORTRAN simulation with the embedded 2D non-isothermal PBMR model can thus provide design guidelines for

PBMR incorporation in a commercial-scale PDH plant.

4.2. Modeling scheme and operating conditions

4.2.1. Governing equations for 2D isothermal operation

Although 1D isothermal models can be applied to describe the membrane reactor performance, there are several significant issues related to improving the membrane reactor modeling that will result in an accurate tool for assessing and optimizing the system performance. In addition to the 1D model which only considers the changes in compositions along the axial direction, I also consider radial dispersion effects in detailed 2D model. The 2D mass transfer governing equations are:

$$\frac{\partial\left(u_T C_i^{\,t}\right)}{\partial z} = D_t\left\{\frac{1}{r_t}\frac{\partial}{\partial r_t}\left(r_t\frac{\partial C_i^{\,t}}{\partial r_t}\right)\right\} + \rho_B\left(-rA\right) \qquad \text{(Tube)} \qquad (4\text{-}1)$$

$$\text{B.C.} \quad \left[\begin{array}{l} z = 0\,, \quad C_i = C_{i0}^{\,t}\,, \quad r_t = 0\,, \quad \dfrac{\partial C_i^{\,t}}{\partial r_t} = 0\,, \\ \\ r_t = R_1\,, \quad D_t\dfrac{\partial C_i^{\,t}}{\partial r_t} = -q_i\left(P_i^t - P_i^m\right) \end{array}\right] \qquad (4\text{-}2)$$

$$D_m\frac{1}{r_m}\frac{\partial}{\partial r_m}\left(r_m\frac{\partial C_i^{\,m}}{\partial r_m}\right) = 0 \qquad \text{(Membrane support)} \qquad (4\text{-}3)$$

$$\text{B.C.} \quad \left[\begin{array}{l} r_m = R_1\,, \quad D_m\dfrac{\partial C_i^{\,m}}{\partial r_m} = -q_i\left(P_i^t - P_i^m\right) \\ \\ r_m = R_2\,, \quad D_m\dfrac{\partial C_i^{\,m}}{\partial r_m} = D_s\dfrac{\partial C_i^{\,s}}{\partial r_s} \end{array}\right] \qquad (4\text{-}4)$$

$$\frac{\partial\left(u_s C_i^{\,s}\right)}{\partial z} = D_s\left\{\frac{1}{r_s}\frac{\partial}{\partial r_s}\left(r_s\frac{\partial\left(u_s C_i^{\,s}\right)}{\partial r_s}\right)\right\} \qquad \text{(Shell)} \qquad (4\text{-}5)$$

$$\text{B.C.} \quad \begin{bmatrix} z = 0\,, & C_i = C_{i0}^{\,s} \\ r = R_2\,, & D_s\dfrac{\partial C_i^{\,m}}{\partial r_s} = D_m\dfrac{\partial C_i^{\,s}}{\partial r_s} \\ r = R_3\,, & D_s\dfrac{\partial C_i^{\,s}}{\partial r_s} = 0 \end{bmatrix} \qquad (4\text{-}5)$$

Compared to the 1D model in Chapter 2 and 3, I have replaced the membrane permeation term with a dispersion term to describe the radial profile inside the tube. The membrane permeance in the 1D model is then included as a boundary condition. Here D represents the dispersion coefficient, u is linear velocity of convective flow at the tube and shell side based on a plug flow assumption, the *R1*,*R2* and *R3* are described **in Fig. 4-1.** C and q are concentration and membrane permeance of each component (with subscript i), ρ_B is the bulk density of catalyst in the packed bed and r_A is the PDH reaction kinetics term. Superscripts and subscripts *t, m* and *s* denote the tube, membrane support and shell side respectively.

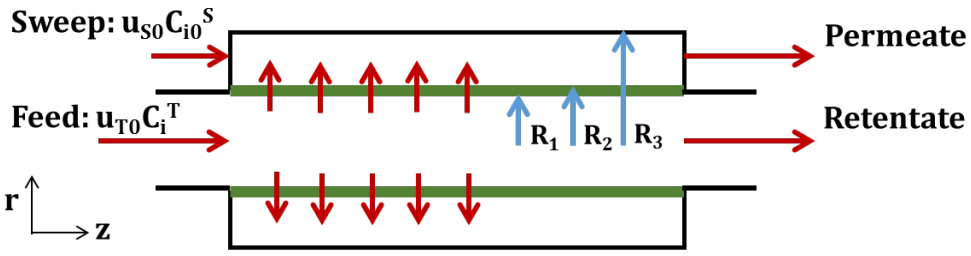

Fig. 4-1. Schematic of PBMR configuration.

4.2.2. 2D non-isothermal modeling

In a laboratory scale PBMR, heat is provided by a heating jacket to the small reactor. The temperature variation is negligible and I can still consider the system as isothermal. However, in a scaled-up system, the temperature distribution cannot be neglected, especially the temperature drop along the axial direction in an adiabatic system. Hence, non-isothermal modeling will be necessary. It is also expected that the non-isothermal model will ultimately provide more accurate design with better prediction of temperature drop from the endothermic reaction. Therefore, the main improvements to the model will be made by including non-isothermal effects as well as the effect of radial dispersion of mass transport. I combine 2D non-isothermal energy balance equation to incorporate the endothermic heat of reaction and possible thermal effect between the tube and the shell side. I consider radial heat conduction in an adiabatic reactor condition. The energy balance equations for the tube, membrane support and the shell side are as follows:

$$\frac{\partial\left(u_T \rho_T C_p T_t\right)}{\partial z} = k_{eff}\left\{\frac{1}{r_t}\frac{\partial}{\partial r_t}\left(r_t \frac{\partial T_t}{\partial r_t}\right)\right\} + \rho_B\left(-r_A\right)\left(-\Delta H\right) \qquad \text{(Tube)} \quad (4\text{-}6)$$

$$\text{B.C.} \quad \begin{bmatrix} z = 0\,, & T_t = T_{t0} \\ r_t = 0\,, & \dfrac{\partial T_t}{\partial r_t} = 0 \\ r_t = R_1\,, & k_{eff}\dfrac{\partial T_t}{\partial r_t} = h_T\left(T_m - T_t\right) \end{bmatrix} \quad (4\text{-}7)$$

$$\frac{1}{r_m}\frac{\partial}{\partial r_m}\left(r_m \frac{\partial T_m}{\partial r_m}\right) = 0 \qquad \text{(Membrane support)} \quad (4\text{-}8)$$

$$\text{B.C.} \quad \begin{bmatrix} r_m = R_1 , & k_m \dfrac{\partial T_m}{\partial r_m} = h_T \left(T_m - T_t \right) \\ r_m = R_2 , & k_m \dfrac{\partial T_m}{\partial r_m} = h_S \left(T_s - T_m \right) \end{bmatrix} \tag{4-9}$$

$$\frac{\partial \left(u_S \rho_S C_S T_s \right)}{\partial z} = k_{gas} \left\{ \frac{1}{r_s} \frac{\partial}{\partial r_s} \left(r_s \frac{\partial T_s}{\partial r_s} \right) \right\} \qquad \text{(Shell)} \tag{4-10}$$

$$\text{B.C.} \quad \begin{bmatrix} z = 0 , & T_s = T_{s0} \\ r_s = R_2 , & k_{gas} \dfrac{\partial T_s}{\partial r_s} = h_s \left(T_s - T_m \right) \\ r_s = R_3 , & k_{gas} \dfrac{\partial T_s}{\partial r_s} = h_w \left(T_w - T_s \right) \end{bmatrix} \tag{4-11}$$

Here T represents temperature, k_{eff} is effective thermal conductivity in packed bed and k_{gas} is thermal conductivity of sweep gas. The ρ and C_p denote average density and heat capacity respectively, and h refers to the heat transfer coefficient. The coupled mass and heat transfer equations are solved simultaneously along the radial and axial directions. I apply the same heat transfer parameters as used in Chapter 3. I combine Finite Difference Method (FDM) for radial direction and Euler method for axial direction. I solve radial profile using FDM, the concentrations, flow rates and temperature profiles are then updated at each axial position.

4.2.3. Membrane reactor configuration: multiple hollow fiber membrane reactor

The PBMR configuration reported in the literature generally consists of the membrane with packed bed catalyst and a sweep gas on the shell side, as presented and

discussed in Chapters 1 and 2. The membrane supports can be macroporous ceramic tubes (e.g. 8 mm ID). These ceramic tubes lead to a large overall reactor volume, due to low surface are per unit volume. The characteristic length for this PBMR configuration was already suggested in Chapter 3, where it decreases with more number of tubes and smaller size of membrane and leads to more membrane surface area to catalytic volume ratio. Thus I suggest the use of closely packed hollow fiber membrane tubes for scaled-up PBMR as represented in **Fig. 4-2.** In this PBMR configuration, the catalysts are placed in the shell side instead of the membrane tubes so that unlimited number of small size of hollow fiber membranes can be simply added without concerns regarding the packing of catalyst inside the small-radius fibers [174-180]. The sweep gas then flows through the bore side of the fibers.

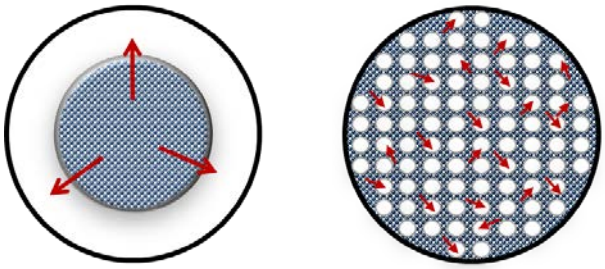

Fig. 4-2. Schematic of PBMR configuration using a tubular membrane with packed catalyst in the bore side (left), and a hollow fiber membrane bundle with catalyst on the shell side (right). The shaded areas and arrows represent packed catalyst and the direction of gas permeation respectively.

4.2.4. Operating conditions for scaled up PDH process

I calculate and compare the PDH performance using different radius of multiple

membrane tubes, ranging from conventional ceramic tubes (8 mm OD) to hollow fibers (0.5 mm OD). I fix the propane feed flow rate of 4000 kmol.hr^{-1} which corresponds to 550 KTA (kilotons per annum) of propylene production in a conventional commercial-scale PDH process (such as Oleflex) with approximately 45% conversion and 90% propylene selectivity are assumed [20]. I use a H_2-selective membrane (permeance of 3e-7 mol.s^{-1}.m^{-2}.Pa^{-1} at the temperature range of operation) and assumed that other components such as propane, propylene, and sweep gas have low permeances (~1e-10 mol.s^{-1}.m^{-2}.Pa^{-1}). When different numbers and sizes of tubes/fibers are considered, the distance between the tubes is adjusted in order to have a fixed WHSV, and hence the amount of catalyst remains constant. I also use steam as a sweep gas since it is abundant in a typical chemical plant and can be easily removed by condensation downstream. The sweep/feed (S/F) molar flow ratio is varied from 1 to 3.

I assume that the tubes are uniformly packed, and that the feed, sweep flow rate, and the catalyst are also evenly distributed to each tube region. I assume that there is negligible heterogeneity in composition and temperature in the spaces between the tubes on the shell side. This assumption is valid if the radial Pe_{tube} is much smaller than the axial Pe_{tube} so that the deleterious effects from radial dispersion can be minimized, as already discussed in Chapter 3. For the PBMR configuration using the hollow fibers with $R_1/L \sim 10^{-2}$ as considered, the effects of radial dispersion can be reasonably small enough to validate the assumption. Also, the heat transfer Pe ($=\alpha/uL$ in Chapter 3) is very large (~10,000) in this system, and therefore radial temperature distribution and axial heat conduction will be negligibly small. As a result, I can perform calculations on a single tube or fiber and simply multiply by the total number of tubes in order to obtain the total

output of the membrane reactor system.

4.2.5. Design of PDH PBMR plant using ASPEN

Modeling studies on PBMRs have generally focused membrane reactor unit itself, and have not considered the larger process that includes high-cost downstream separations. Process simulations using a flowsheeting package such as ASPEN simulation would be a valuable tool for understanding the impact of the membrane reactor system on the overall process and provide guidance for industrial process design. The technical challenge here is to incorporate our specialized membrane reactor model into the ASPEN process simulator. To do so, the membrane reactor simulation module (written in FORTRAN code) is first prepared as a tool for reading input parameters, calculating the reactor performance, and generating output results. This has been done by creating a PBMR model block in the model library and combining our FORTRAN module with the ASPEN subroutine usrus2.f (provided by the manufacturer) that allows integration of user-supplied system models with the process simulator. I thus obtain a customized PDH process simulator that incorporates the 2D non-isothermal PBMR model.

The flowsheet of the PBMR PDH plant is shown in **Fig. 4-3**. The input parameters for the PBMR block are reactor dimensions, feed, sweep flow rates, kinetic parameters for PDH reaction, and the membrane properties such as permeance and selectivity. In the PBMR module, I consider multiple membrane tubes/fibers with catalyst on the shell side as previously discussed. I suggest using three adiabatic PBMRs with

inter-stage heaters in systems with or without a recycle loop as depicted in **Fig. 4-3a and 4-3b**. Based upon input from Dow Chemical, I also consider a second type of recycle configuration that performs product separation after each reactor stage followed by recycling of feed and sweep streams as shown in **Fig. 4-3c**. The feed flow rate to the overall process is 4000 $kmol.hr^{-1}$ for the no-recycle system while I use 2000 $kmol.hr^{-1}$ for the recycle configurations since the overall conversion in recycle system reaches 100 %. For H_2 separation, I use a simple distillation column with 10 equilibrium stages and reflux ratios in the range of 1.5-5. PSA (pressure swing adsorption) can also be used for the downstream H_2 separation [181-183]. However, I do not focus substantially on the H_2 separation since H_2 can be easily removed from a mixture with C_3 due to large volatility differences. A distillation column for the downstream C_3 splitter is used, with 200 equilibrium stages and large values of reflux ratio, (30-70 depending on the feed composition at the C_3 splitter entrance).

4.2.6. Calculation of required energy for downstream separation

I expect that the PBMR using hollow fiber membranes provides benefits in terms of not only improving the PDH conversion but also requiring less reactor volume. I then focus on how the enhancement of PDH performance affects the downstream separation processes by determining the changes in required energy duties for a fixed purity of the product. Inter-stage heaters with three adiabatic reactors are applied as described in **Fig. 4-3**. I focus on the C_3 splitter, which is one of the most energy intensive separation processes in the chemical industry [22-24]. Also the preheating, reheating and cooling of outlet streams are considered.

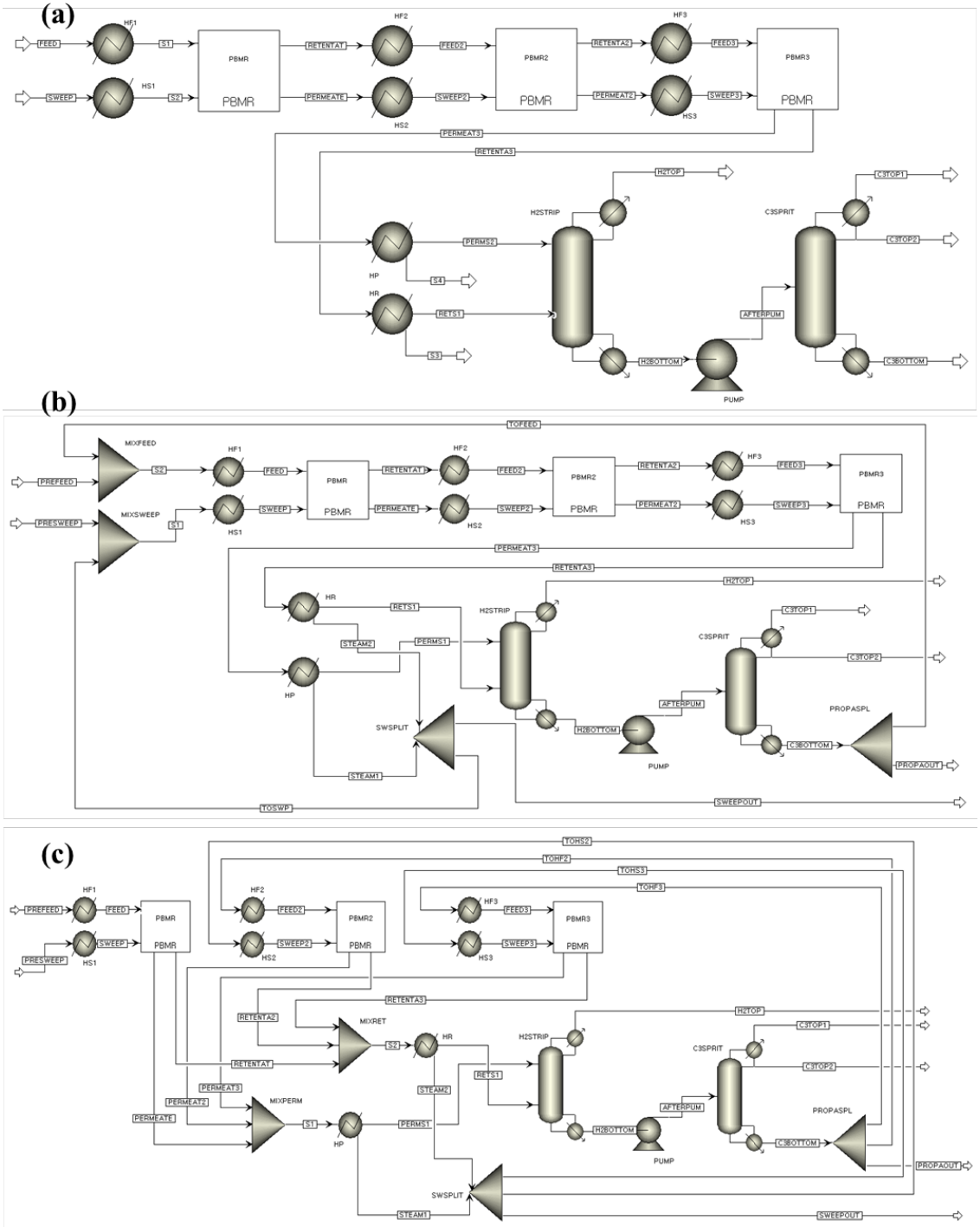

Fig. 4-3. ASPEN flowsheet of PDH plant using 2D non-isothermal PBMR model with downstream separation. (a) non-recycled system (b) simple recycled system (c) recycled system with product separation at each stage.

4.3. Results and discussion

4.3.1. Effect of radial mass dispersion

From dimensional analysis in the 1D model, the Pe_{mem} is used as the ratio of convective transport and membrane diffusive transport rates [62]. Similarly the Pe_{mem} can be also defined in the 2D model as follows:

$$Pe_{mem} = \frac{u_{T0}}{q_{H_2} R_g T} \frac{R_t}{2L} \tag{4-12}$$

In addition to Pe_{mem} in the 1D model, Pe_{tube} can be used as the ratio of convective and radial transport rate in the tube side in order to assess the mass dispersion effect inside the packed bed catalyst. Based on the 2D mass transfer model, another Pe_{tube} is defined as follows:

$$Pe_{tube} = \frac{u_{T0} / L}{D_r / R_t^2} \tag{4-13}$$

When the Pe_{tube} increases, the convective transport from feed flow will dominate the system and the membrane transport will only affect vicinity of the membrane boundary. Therefore increasing the effect of convective transport leads to a decrease in membrane permeation and PBMR performance. In the opposite case when the Pe_{tube} decreases, membrane transport will be important throughout the radial distance and further decreasing the Pe_{tube} will take the system close to the 1D model. Since the radial dispersion coefficient (D_r) determines the Pe_{tube}, I investigate its effect on the axial dimensionless molar flow rate profiles of propane at the outlet of the tube side (**Fig. 4-4**).

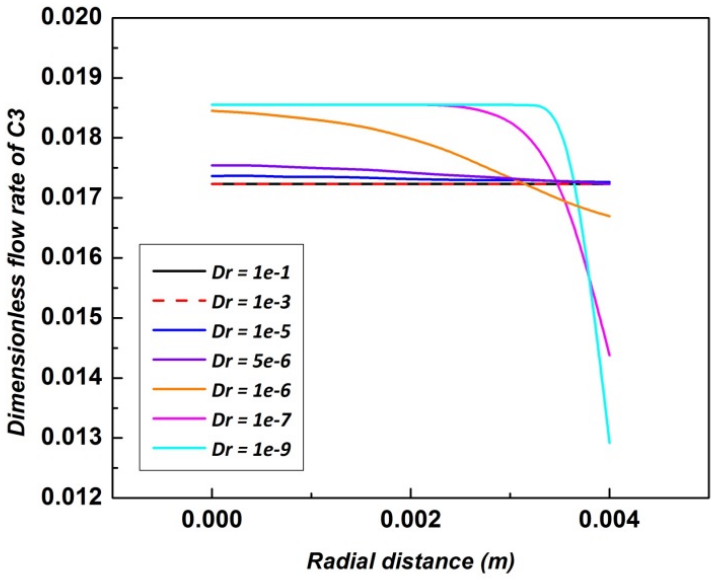

Fig. 4-4. Effect of dispersion coefficient on axial dimensionless molar flow rate of C_3H_8 as a functional of radial distance from the central axis of the tubular membrane.

A H_2 selective zeolite membrane is used with permeance of 1e-7 ($mol.s^{-1}.m^2.Pa^{-1}$). The SAPO-34 (~0.38 nm pore size) zeolite membrane can be one of the examples for this property [27]. The decrease in the propane flow rate is due to its consumption from the PDH reaction. The flow profile is mainly affected by bulk convective transport as decreasing D_r and the H_2 permeation is limited in the vicinity of the membrane boundary. As a result, more consumption of propane from the PDH reaction is only expected near the membrane layer with the sharp decrease as shown in **Fig. 4-4**. Therefore the enhancement of PBMR conversion is lowered. As D_r, is increased, however, the effect of membrane transport is felt throughout the radial distance and much flatter radial profiles

are observed with D_r values more than 10^{-5} $m^2.s^{-1}$. I also compare the distribution of the dimensionless molar flow rate for different membrane tube/fiber radius. The dimensionless flow rates of propane at the reactor exit are plotted in **Fig. 4-5** for a fixed dispersion coefficient, 5e-5 $m^2.s^{-1}$. Decreasing the tube radius leads to more uniform profiles as shown in **Fig. 4-5**.

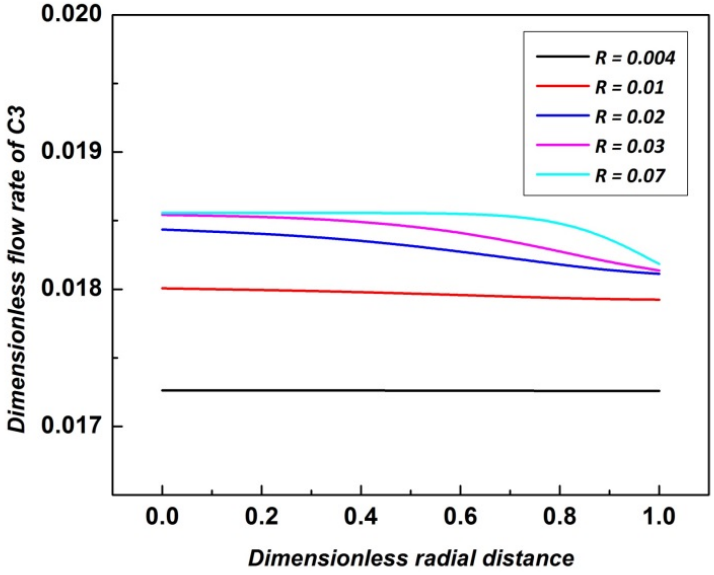

Fig. 4-5. Effect of membrane radius on dimensionless molar flow rate of C_3H_8.

The different flow profiles with respect to the dispersion coefficient and radius of the membranes are attributed to the Pe_{tube}. More uniform profiles are generally expected with increasing Pe_{tube} in case of plug flow reactors, since the profiles are more dominated by convective flow over radial dispersion. However, in the PBMR configuration, a large Pe_{tube} means that the effect of membrane permeation is limited in the vicinity of the membrane layer (as observed in **Fig. 4-4**) due to the dominant effect of convective flow. When lower Pe_{tube} is applied in the tube side, membrane permeation plays an important

role throughout the radial distance. Combining with PDH reaction and membrane permeation, lower Pe_{tube} leads to more uniform radial profile of propane feed flow rate, which has lower level than what was obtained at high Pe_{tube} since more PDH reaction takes place due to the H_2 permeation. In order for the membrane permeation to be more effective, I suggest that lower Pe_{tube} less than ~1 should be applied.

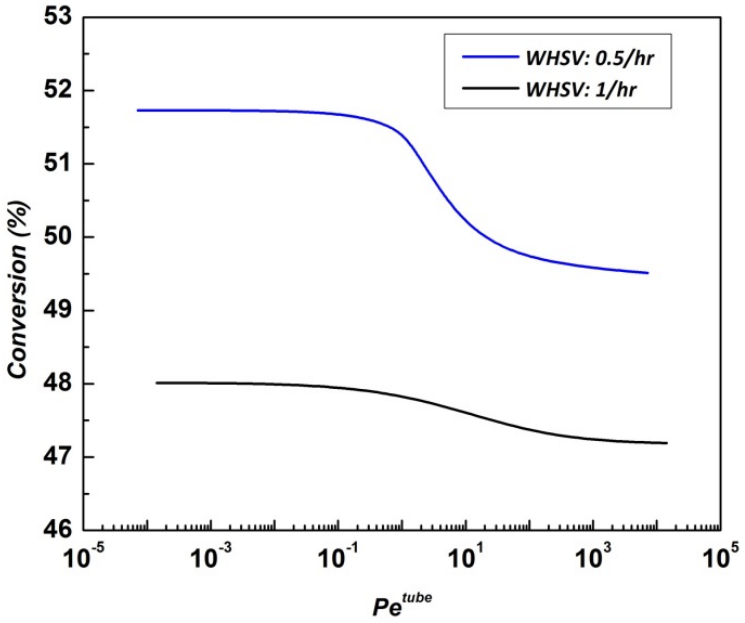

Fig. 4-6. Relation between Pe_{tube} and conversion.

Based on the definition of Pe_{tube}, a longer membrane of smaller radius is a better candidate material for PDH PBMR applications. The PDH conversions with respect to the Pe_{tube} are plotted for two weight hourly space velocity (WHSV, hr^{-1}) values in **Fig. 4-6**, clearly showing the relation between the PDH conversion and the Pe_{tube}. As discussed above, increasing the Pe_{tube} allows domination of bulk convective flow and causes a decrease in conversion. For both WHSV conditions, lowering the Pe_{tube} increases the

conversion as it approaches the plateau level of conversion, which is the same conversion obtained from the 1D model.

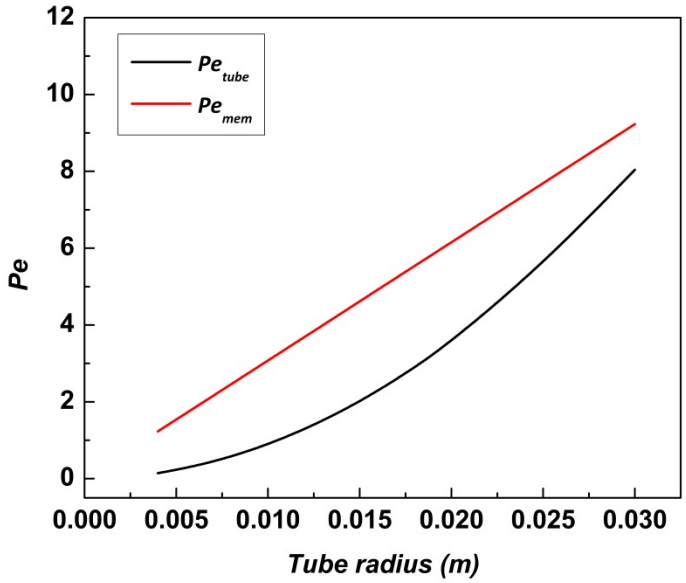

Fig. 4-7. Relation between membrane radius and Pe_{tube}.

Increasing membrane radius leads to higher Pe_{tube} and Pe_{mem}, as can be seen in **Fig. 4-7**. The Pe_{mem} is inversely proportional to the ratio of membrane surface area and catalyst volume. Hence, more enhancement of PBMR performance is expected with lower Pe_{mem}. The decreasing trend of the conversion with respect to the membrane radius in **Fig. 4-8** is attributed to increase in both *Pe* numbers. Therefore a large membrane permeance or a larger number of membrane tubes should be considered. If I keep Pe_{mem} fixed while Pe_{tube} is still increasing due to larger membrane radius, the decreasing trend of conversion with respect to the membrane size is somewhat improved as shown in **Fig. 4-9**. Hollow fiber membranes of small radius should be considered so that Pe_{tube} can be

small enough to minimize the negative effect of radial dispersion.

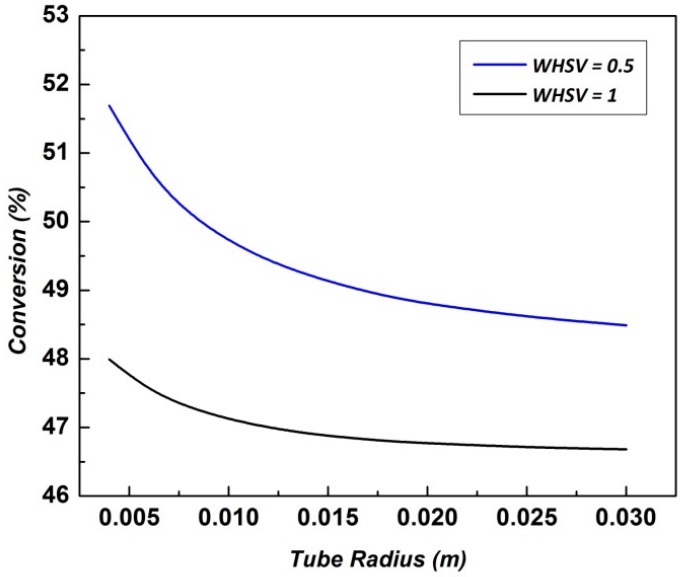

Fig. 4-8. Relation between membrane radius and conversion.

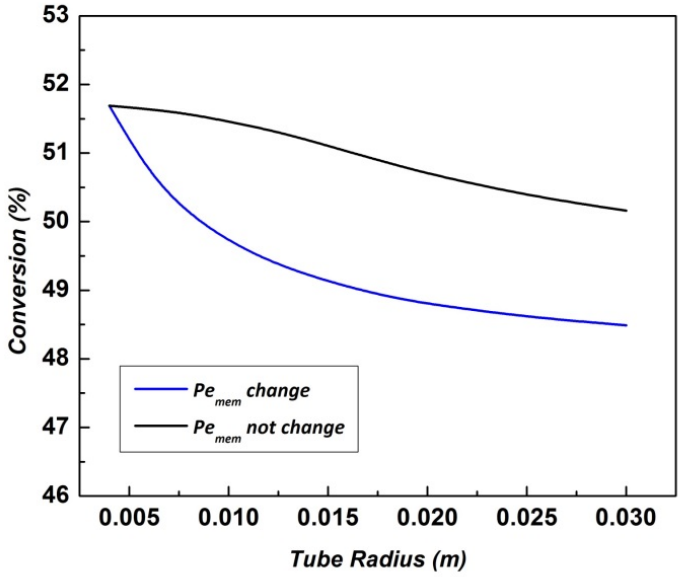

Fig. 4-9. Effect of the Pe_{mem} on the relation between membrane radius and conversion.

4.3.2. Total volume of PBMR

The PDH performances with different numbers and radii of tubes are calculated and compared with three 2D adiabatic PBMRs and inter-stage heaters. Each reactor has 5 m total length. The inlet temperatures of both feed and sweep gas are 650°C and the outlet streams are reheated by the inter-stage heaters after temperature drop of the endothermic PDH reaction. The main difference between large and small membrane radius is the membrane surface area relative to the fixed catalyst volume. I defined a membrane packing density, 'a' value as follows:

$$a = \frac{membrane\ surface\ area}{catalytic\ volume} = \frac{2R_t}{(R_s\text{-}R_t)^2(1\text{-}void)\rho_{cat}} \qquad (4\text{-}14)$$

Here, R_t represents the radius of membrane tube, R_s denotes the shell radius which is adjusted for each size of the membrane as mentioned. The *void* and ρ_{cat} is the void fraction and density of the catalyst respectively. The smaller the membrane size, the larger *a* value I can achieve. The $Pe_{mem}$is linearly proportional to *a* at the same WHSV and therefore more effective membrane permeation is expected with larger *a* values. I calculated conversion and corresponding propylene production as a function of *a* in **Fig. 4-10.** Although each condition predicted different PDH performances, they can be overlapped as a function of *a* at each S/F ratio. In **Fig. 4-10**, the larger-radius membranes (8 or 4 mm) are positioned in the lower range of *a* while the small-radius membranes (1 or 0.5 mm) enable us to achieve high performance with large *a* values. The increasing trend of conversion with respect to *a* is more clearly observed at large S/F ratio since it involves larger membrane permeation.

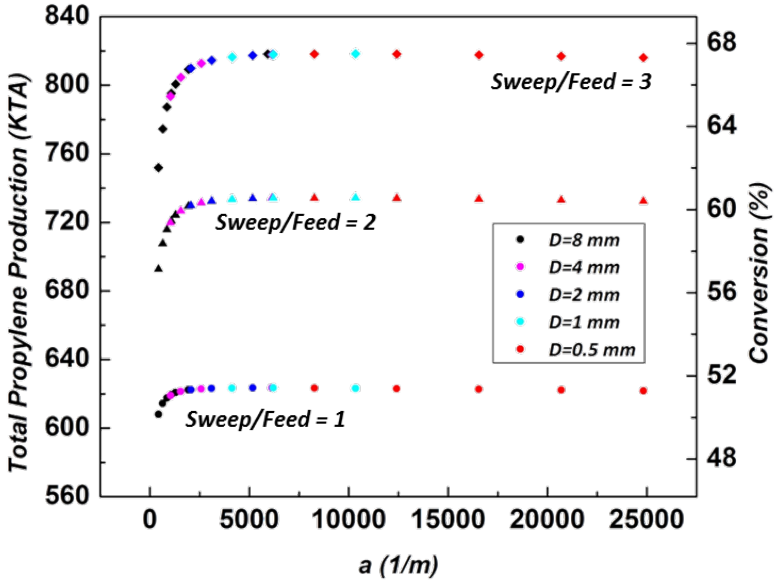

Fig. 4-10. Propylene production rate and conversion as a function of 'a' values.

It should be noted that the enhancement of PDH performance by addition of the membranes reaches a plateau in **Fig. 4-10**, which means that very large membrane surface areas do not provide additional benefit. I also calculate the required volume of the PBMR based on the number of membrane tubes for a target propylene production. At each S/F ratio the target production is assumed to be located at the onset of the plateau region in **Fig. 4-10**, e.g., ~800 KTA at S/F = 3. Then the required number of tubes at each condition can be back-calculated and plotted in **Fig. 4-11**. The total PBMR volume is then estimated as a summation of the fixed catalytic volume and the total membrane volume, as shown in **Fig. 4-12**. The **Table 4-1** tabulates in detail the PBMR parameters for the target production when hollow fiber membranes (radius: 0.25 mm) are used. In **Fig. 4-12**, the black bar represents the fixed catalytic volume, and the gray bar is the addition of the membrane volume. The total volume of this PBMR is even less than the

total catalytic volume in the conventional PBR estimated with 45% conversion and 90% propylene selectivity for the same target production rate. This study clearly demonstrates the advantage of using the hollow fiber membrane reactor, which requires a much smaller PBMR volume while making a large enhancement in propylene production from 550 to 800 KTA.

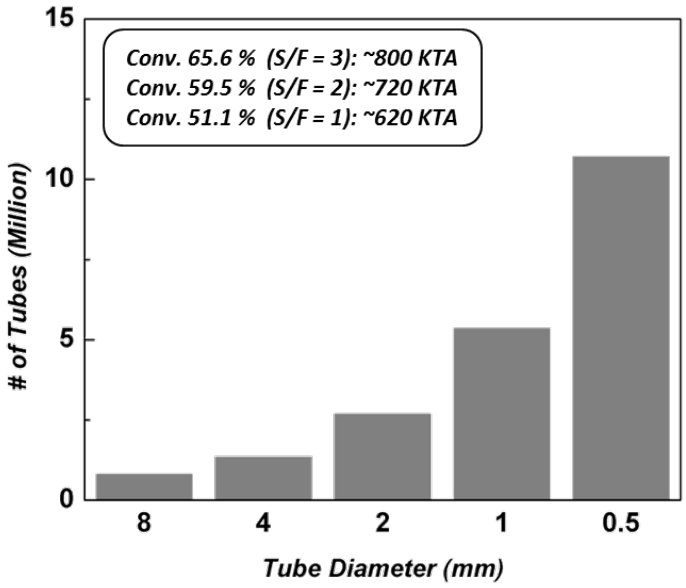

Fig. 4-11. Comparison of required number of membrane tubes for target conversions.

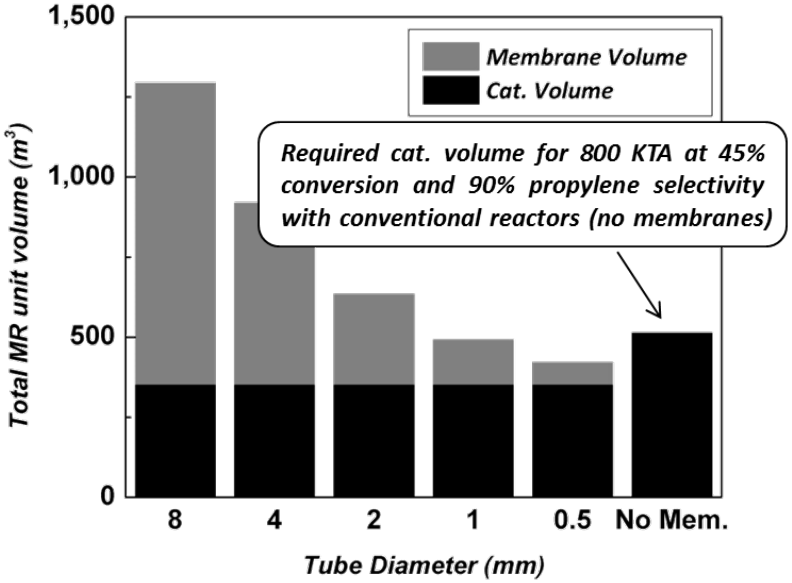

Fig. 4-12. Comparison of required membrane reactor volume for target conversions.

Table 4-1. The PBMR configuration for 800 KTA of propylene production (S/F = 3).

Membrane radius (mm)	0.25
Membrane thickness (mm)	0.125
# of membrane tubes (million)	10.7
Catalyst volume (shell volume, m^3)	350
Catalyst amount (ton)	525
Feed flow rate ($kmol.hr^{-1}$)	4000
Preheat temperature (°C)	650
WHSV (hr^{-1})	0.34
Total membrane reactor volume (m^3)	421

4.3.3. Adiabatic operation in PBMR with multiple hollow fiber membranes

The temperature profiles of the PBMR are calculated and compared with the PBR using the same 2D adiabatic reaction zones with inter-stage heaters. The temperature profiles of the catalytic side are shown in **Fig. 4-13a**. Less temperature drop is observed with higher sweep flow rates in the PBMR configuration, thus leading to more conversion as can be seen in **Fig. 4-13b**. Based on the non-isothermal equations, the adiabatic temperature drop in a hollow fiber PBMR configuration is mainly determined by convective heat transport and heat of reaction. At the fixed WHSV, effects of convective heat transport are similar for all the cases. Therefore the difference in the temperature drop is due to heat transfer from the sweep gas to the catalytic side. Since I use high temperature steam as a sweep gas, it should be elucidated how the sweep gas itself affect the PDH performance. The same PBMR configuration is applied with different S/F ratios without membrane permeation and compared with a conventional PBR. Since membrane permeation is not involved in the latter case, the sweep gas only affects the heat transfer from the sweep gas to the catalytic side. The temperature profiles of this condition at each reactor stage are plotted in **Fig. 4-14**. In **Fig. 4-14**, it is clear that main difference in the temperature drop between PBR and PBMR arises from the high temperature sweep gas. More heat is provided by high temperature sweep gas as increasing the sweep flow rate and hence the hollow fiber itself works as an internal heat exchanger inside the packed bed catalysts.

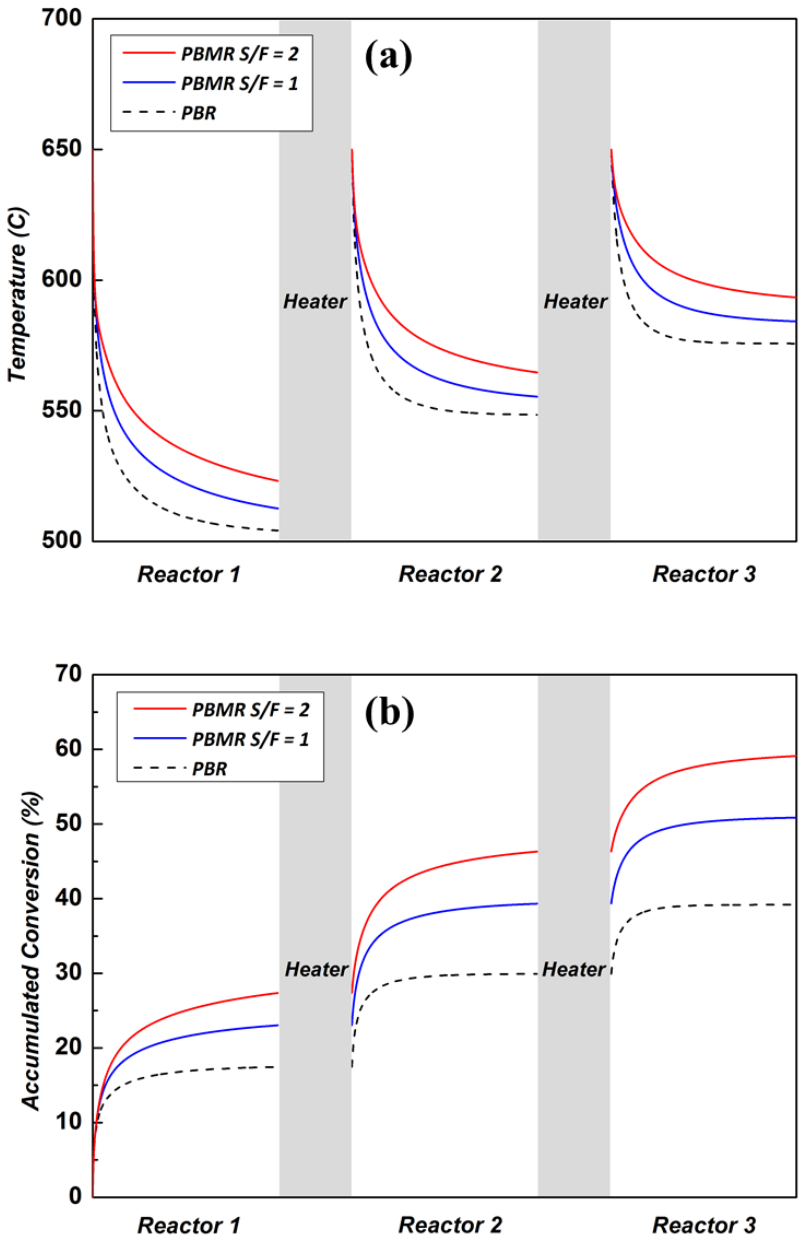

Fig. 4-13. (a) Temperature profiles and (b) accumulated conversion of three reactor stages (Reactor1, Reactor2, Reactor3) for PBR and PBMR conditions.

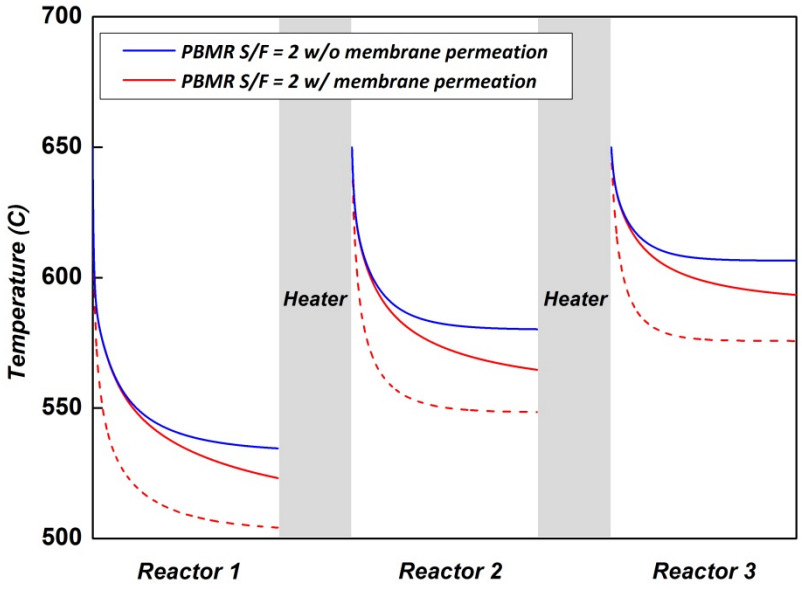

Fig. 4-14. Temperature profiles of PBMR with and without membrane permeation (S/F = 2). The dashed lines indicate the profiles of PBR.

Due to the heat supply, the conversion level also increases by the sweep flow rates as represented in **Fig. 4-15**. In addition to the accumulated conversion, the equilibrium conversion at each temperature value is also plotted. For both PBR and PBMR without membrane permeation, equilibrium limited conditions were reached at the end of each reactor stage. The PBMR configuration without membrane permeation is compared with the PBMR with membrane permeation at the same sweep flow rate. The initial temperature drops are almost the same in **Fig. 4-14**, which means the region near the reactor entrance is mostly governed by kinetics rather than membrane transport. After the initial temperature drop, the membrane permeation leads to more conversion and breaks the equilibrium as shown in **Fig. 4-16**. The adiabatic operating lines in **Fig. 4-17** more

clearly showed the difference in each configuration. Higher conversions were reached with the high temperature sweep gas even without membrane permeation in **Fig. 4-17a and 4-17b**, but still following the equilibrium line. In contrast, further enhancements can be achieved by breaking the equilibrium when there is membrane permeation, as shown in **Fig. 4-18**.

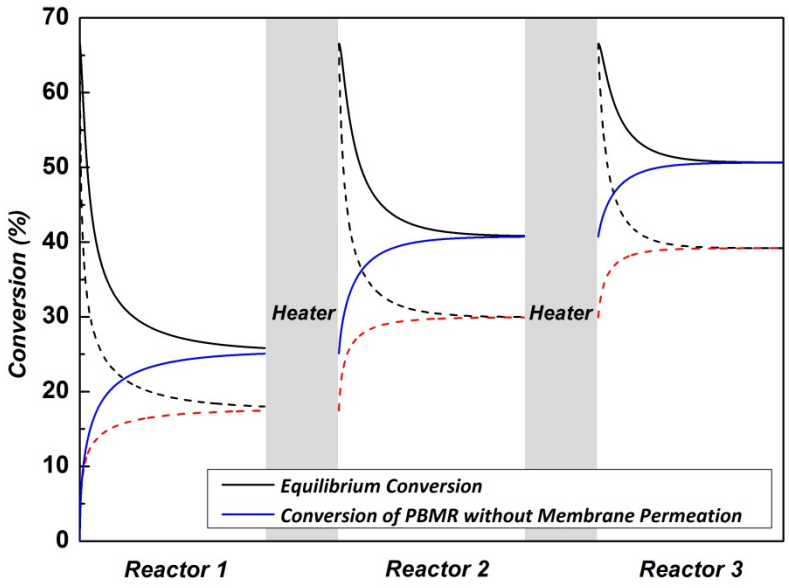

Fig. 4-15. Equilibrium and accumulated conversions along the three reactors using PBMR configuration without membrane permeation (S/F = 2).

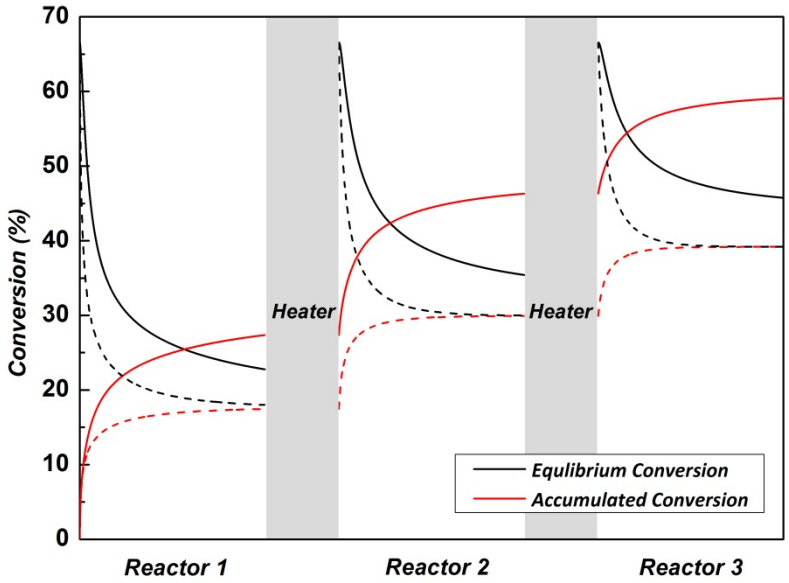

Fig. 4-16. Equilibrium and PBMR accumulated conversions along the three reactors (S/F = 2). The dashed lines indicate the equilibrium and accumulated conversions of PBR.

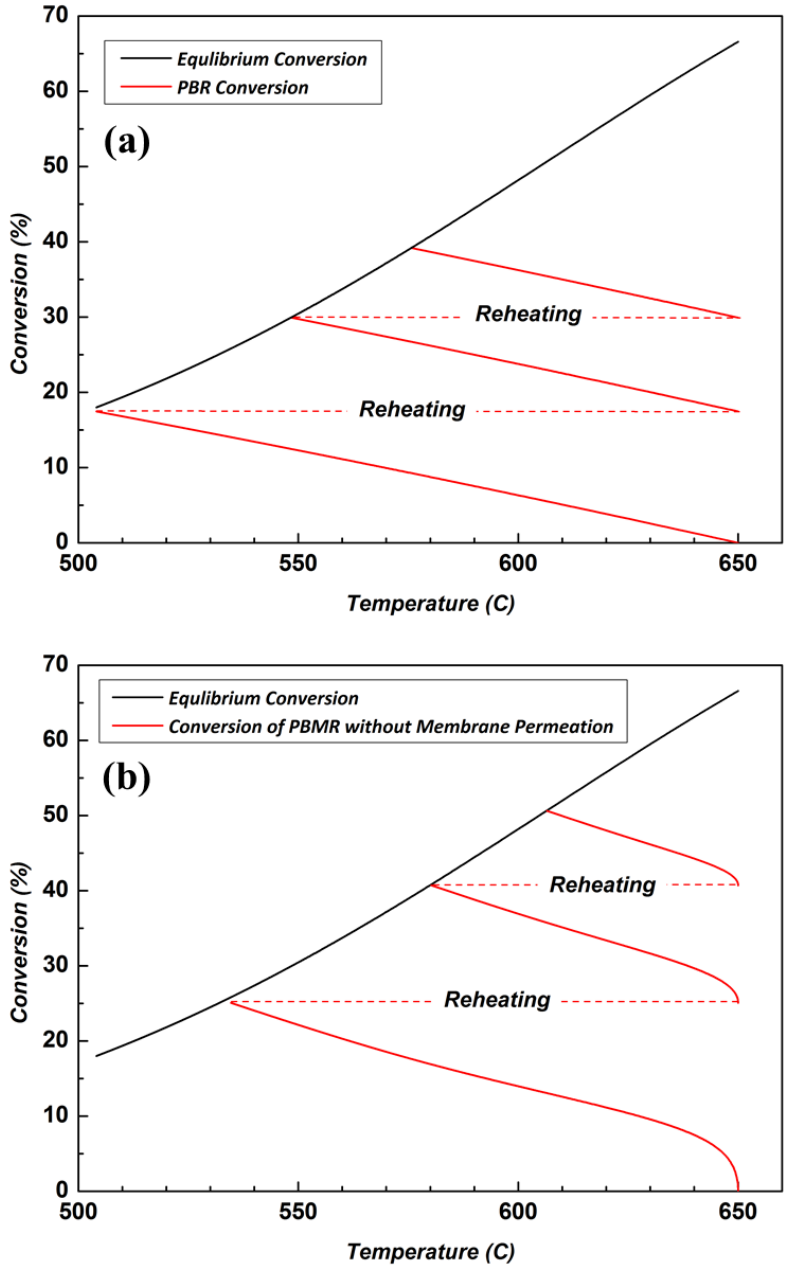

Fig. 4-17. Adiabatic operating line of (a) PBR, (b) PBMR configuration without membrane permeation (S/F = 2). The dashed lines depict the reheating of retentate streams in inter-stage heaters.

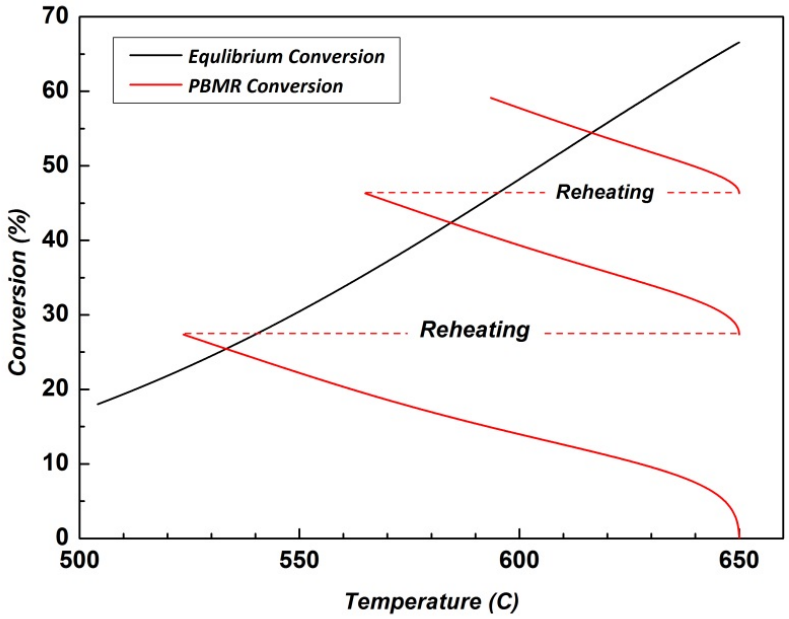

Fig. 4-18. Adiabatic operating line of PBMR (S/F = 2) along the three reactors. The dashed lines depict the reheating of retentate streams in inter-stage heaters.

4.3.4. Plant simulation: Non-recycled system

The PDH conversions of three adiabatic reactors in the PBR and PBMR system are plotted in **Fig. 4-19**. The feed flow rates were fixed at 4000 kmol.hr^{-1} and other operating conditions are the same as **Table 4-1**. The enhancement of conversion using PBMR with higher sweep flow rates is clearly observed and leads to a change in composition of propane and propylene at the C_3 splitter entrance as shown in **Fig. 4-20**. I compare the energy duty at the C_3 splitter for PBR and PBMR with different S/Fs. In the C_3 splitter, more energy duty is required with higher distillation rate and reflux ratio for the same purity of the product, which is 99.9% of propylene in this case. Although there are differences in the compositions in the C_3 splitter feed at different PDH conversions in

Fig. 4-20, the energy duties do not show much difference as observed in **Fig. 4-21.** The energy duties were calculated by summation of absolute values of heating and cooling duty. The distillation rate and reflux ratio are adjusted for a target of 99.9% of propylene production at each condition. Although a lower reflux ratio is required at the splitter when using a PBMR with higher sweep flow rate (due to more propane conversion), the increasing production of propylene also needs a higher distillation rate. In addition to the energy in the C_3 splitter, other energy duties are also added in **Fig. 4-21,** which include preheating and reheating of inlet streams, cooling of outlet streams, and also H_2 separation column. The energy duties at each different condition of PBR and PBMR indicate a very important aspect of PBMR application. Although more enhancements can be made by using higher sweep flow rates, this also requires more energy for heating the sweep and permeate streams and removal of sweep gas from outlet mixtures. Therefore in the non-recycled system at the fixed flow rate, using the PBMR increases both propylene production and total energy load. The additional energy cost is compensated by enhancement of propylene production.

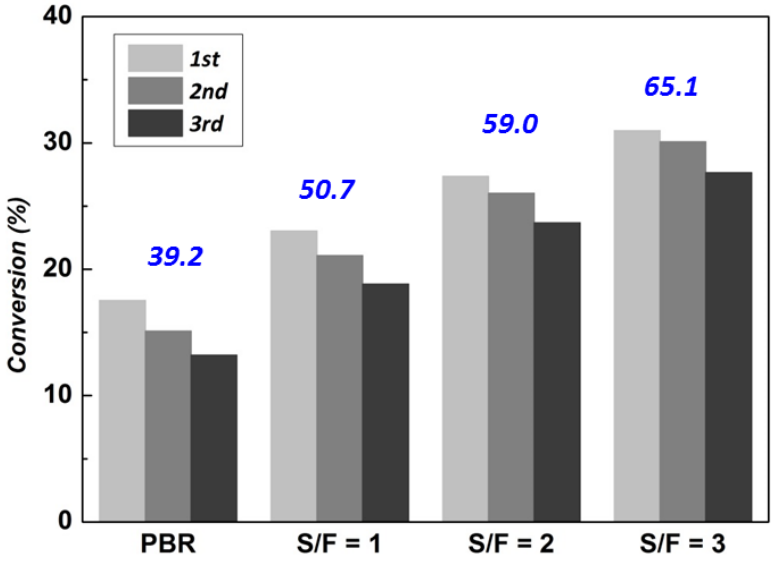

Fig. 4-19. PDH conversions of three reactors in a PBR and PBMRs with different S/F. The numbers in each condition indicate the overall conversions.

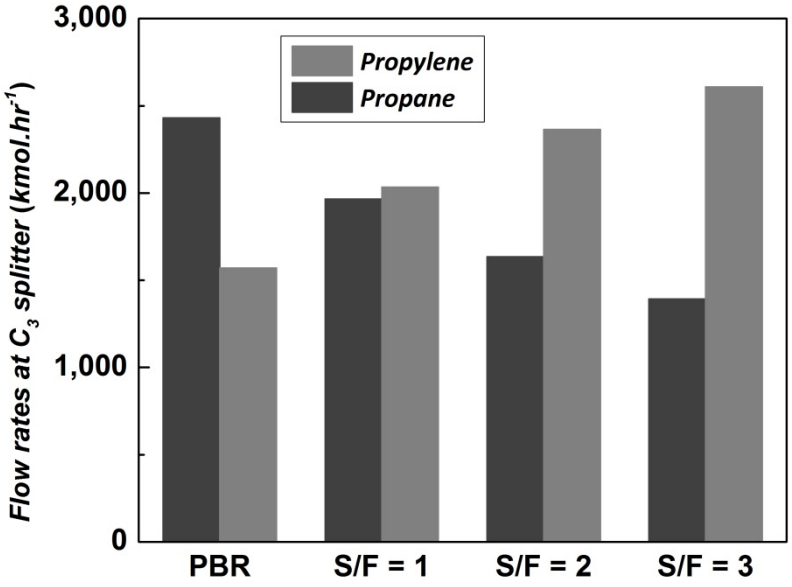

Fig. 4-20. Flow rates of propane and propylene at C_3 splitter entrance in a PBR and PBMR operations.

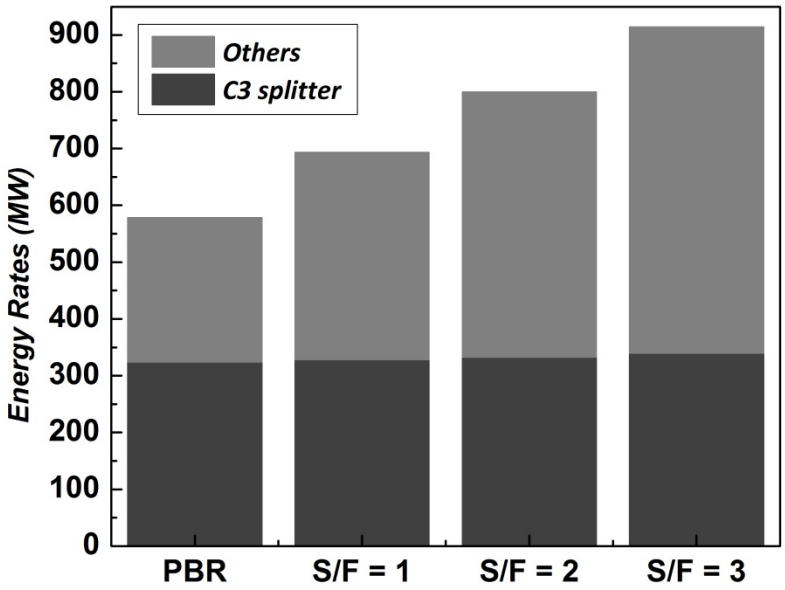

Fig. 4-21. Required energy duties in a PBR and PBMR operations.

For better comparison between the PBR and PBMR configuration on downstream separation, I adjusted the feed flow rate of the PBMR to 3000 kmol.hr^{-1} in order to make the same propylene production from the PBR with 4000 kmol.hr^{-1}. The enhancement of conversion using the PBMR allows us to have lower feed flow rates than PBR and both PBR and PBMR produce ca. 1500 kmol.hr^{-1} of propylene as shown in **Fig. 4-22**. The same propylene production with more conversion leads to less amount of propane entering the C_3 splitter and thus saving the energy duties as can be seen in **Fig. 4-23 and Fig. 4-24**. Although additional sweep and permeate streams increase the other energy requirements as previously discussed, the total overall energy duty of the PBMR configuration is lower than that of the PBR system. Therefore the same propylene production can be achieved by the PBMR operation with less propane feed and less total

energy duty. This indicates another important feature of the PBMR application for PDH, *i.e.* it provides more efficient energy use while enhancing the conversion.

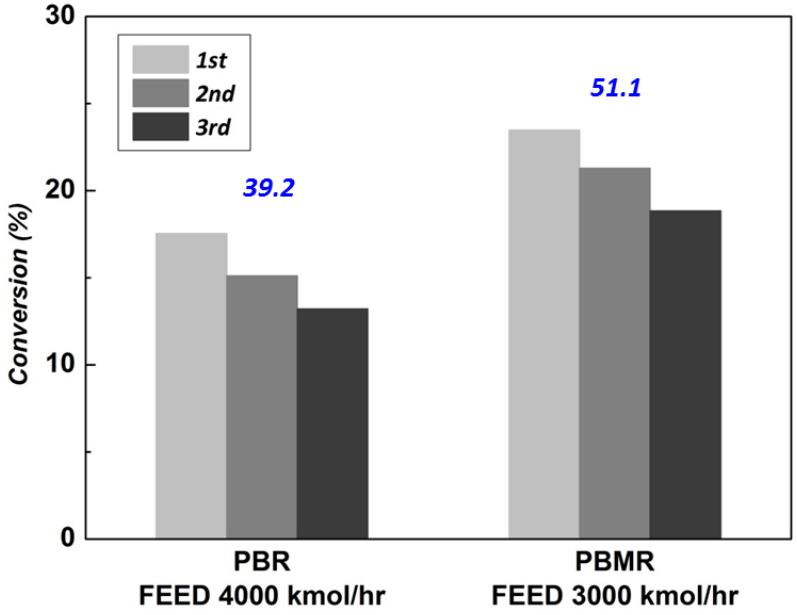

Fig. 4-22. PDH conversions of three reactors in a PBR (feed = 4000 kmol.hr^{-1}) and PBMR (S/F = 1, feed = 3000 kmol.hr^{-1}). The numbers in each configuration indicate the overall conversion.

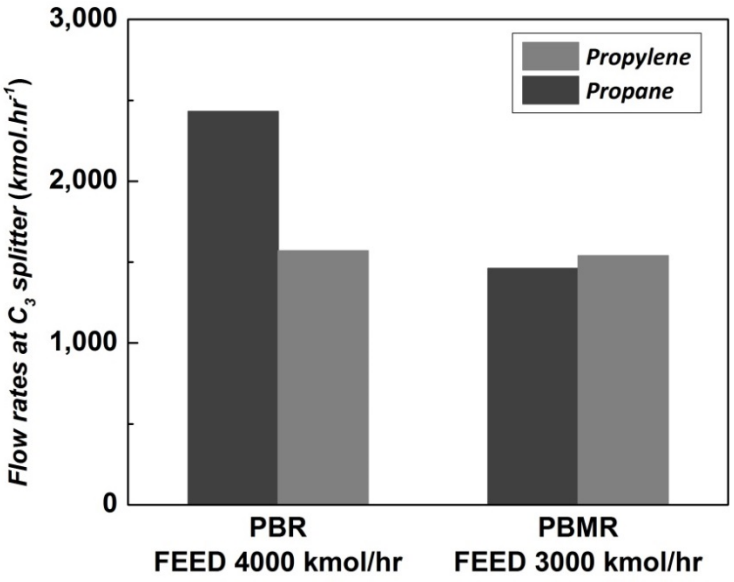

Fig. 4-23. Flow rates of propane and propylene at C_3 splitter entrance in a PBR (feed = 4000 kmol.hr^{-1}) and PBMR operation (S/F = 1, feed = 3000 kmol.hr^{-1}).

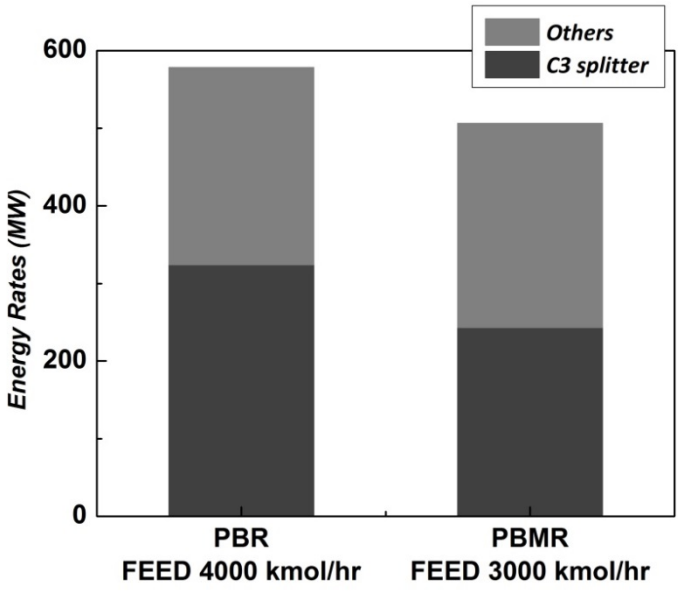

Fig. 4-24. Required energy duties in a PBR (feed = 4000 kmol.hr^{-1}) and PBMR (S/F = 1, feed = 3000 kmol.hr^{-1}).

4.3.5. Plant simulation: Simple recycled system

Modeling simulation for simple recycled system is carried out for the same PBR and PBMR. In this configuration, the outlet stream of propane from the bottom of the C_3 splitter is recycled and added to the fresh propane feed before it is preheated to 650°C as shown in **Fig. 4-3b**. Since all the unreacted propane is recycled, 100% overall propane conversion is achieved at steady state in all recycled configurations. The fresh propane flow rate is fixed at 2000 $kmol.hr^{-1}$, which corresponds to about 600 KTA of total propylene production, and use the same operating conditions for both PBR and PBMR. The recycled amount of propane to the fresh feed at steady state is shown in **Fig. 4-25** at each PBR and PBMR condition. The single pass conversion at each condition is also plotted in **Fig. 4-26**. It can be seen from **Fig. 4-25 and Fig. 4-26** that lower amounts of propane are recycled in the system as the conversion increases. As previously discussed, the amount of propane remaining in the system affects the energy duty at the C_3 splitter. In the conventional PBR, more propane is recycled in the system such that more propane concentration is expected at the entrance of the C_3 splitter. This difference affects the performance of the C_3 splitter where more reflux ratio is required for the target propylene purity (99.9%) when the large propane/propylene composition of stream enters the C_3 splitter. The gray bar at each condition in **Fig. 4-25** is the propane flow rate at the C_3 splitter entrance while the amount of propylene was fixed at 2000 $kmol.hr^{-1}$. The energy duties at the C_3 splitter were summarized in **Table 4-2**. More reboiler and condenser duties are required while less heat duties are needed for the PBMR configuration as incorporating membrane permeation and increasing sweep flow rates. Even for a heat integrated column where the net duty would be more important, the same trend is

observed as tabulated in **Table 4-2**.

The PBMR configuration uses considerable amounts of sweep gas and therefore separation of sweep gas at the outlet stream should be taken into a consideration similar to the previous case. Other energy duties are also separately calculated, which includes preheating and reheating the feed and sweep streams and cooling of retentate and permeate streams. More heating and cooling energies are needed with increasing sweep gas flow rates which may not be an issue for conventional PBR system. However, considering the significant amount of propane recycled in the PBR plant, more heating and cooling may be also added for the recycled streams in PBR. In **Table 4-3**, I summarize the heating and cooling duties for those energies other than C_3 splitter. As expected, more heating and cooling duties for feed and retentate stream are predicted for the conventional PBR system due to increasing amount of recycled propane while more energy is needed to handle the sweep gas streams in the PBMR configuration. The overall energy for C_3 splitter and other processes are estimated from the summation of absolute values of heating and cooling duties and display with different sweep flow rates in **Fig. 4-27.** This clearly indicates a trade-off relation between advantage and disadvantage of adding membrane with sweep gas. The PBMR configuration with sweep gas decreases the energy duty at C_3 splitter by more propylene production. Other than the C_3 splitter, the PBMR configuration with more sweep gas clearly requires more energy for heating/cooling and removing the sweep gas, which should be considered in plant design of PBMR configuration.

However, considering the overall energy including C_3 splitter as well as heating and cooling of other streams, less energy is required with the PBMR configuration with more sweep flow rates as shown in **Fig. 4-28.** This overall energy shows a decreasing trend with more sweep gas but levels off starting at ca. S/F = 2, indicating that the sweep gas flow does not need to be increased after a certain level of S/F. I also consider total net duty, which is difference between heating and cooling energies and probably provides the ideal value for the best optimized system. The total net duty is also decreasing with more sweep flow rate with less net heating duty but then it turns to more net cooling duty after the sweep gas reaches S/F = 1.5 as can be seen **Fig. 4-29**. Based on the overall energy and net duties, the optimal range of values of S/F are 1.5 - 2 in this study. In all cases, using the PBMR hollow fiber configuration can save a large amount of energy cost, which is significant if the hundreds KTA of annual propylene production is considered.

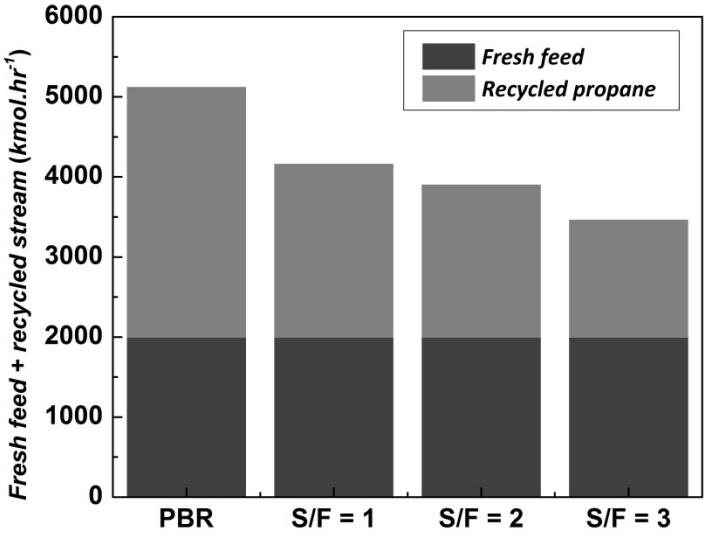

Fig. 4-25. Total flow rates entering PBR and PBMR reactor stages at steady state.

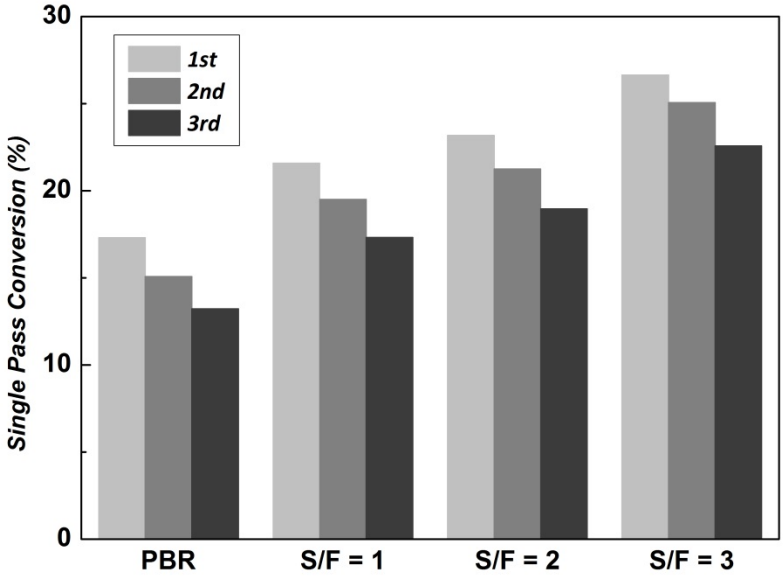

Fig. 4-26. Single pass conversions of each reactor stage in simple recycled PDH plant.

Table 4-2. Reboiler and condenser heat duties of C_3 splitter (200 stages).

	Sweep/Feed	Reboiler (MW)	Condenser (MW)	Net duty (MW)	Reflux ratio
Conventional PBR	-	221	205	16	30
PBMR	1	186	172	14	25
	2	164	152	12	22
	3	150	139	10	20

Table 4-3. Heating and cooling duties for feed/sweep and retentate/permeate streams.

	Sweep/Feed	Heating (MW)		Cooling(MW)	
		Feed	Sweep	Retentate	Permeate
Conventional PBR	-	169	-	106	-
PBMR	1	146	16	90	42
	2	126	63	78	82
	3	110	92	69	123

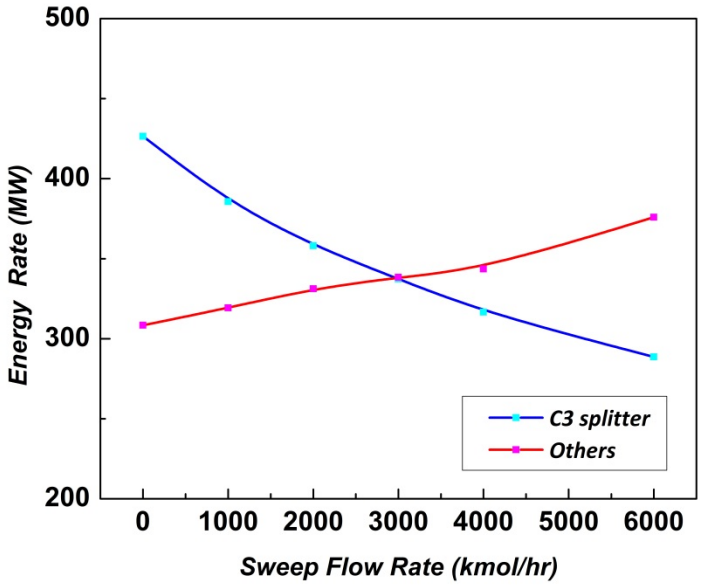

Fig. 4-27. Required energy duties of C_3 splitter and other streams with respect to sweep flow rates.

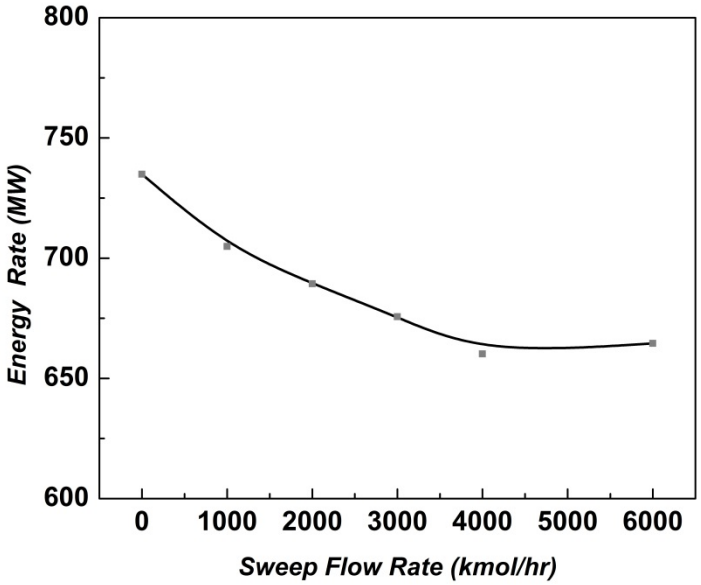

Fig. 4-28. Total energy duty with respect to sweep flow rates.

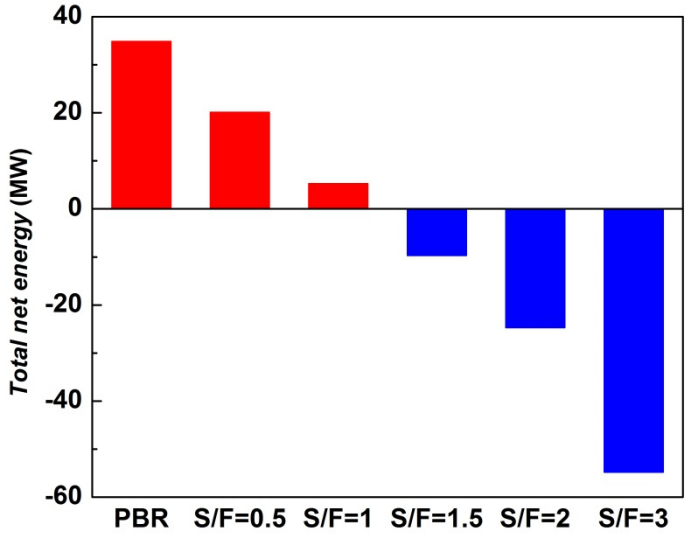

Fig. 4-29. Total net energy duty in PBR and PBMRs.

4.3.6. Plant simulation: Recycled system with product separation at each stage

In the non-recycled or simple recycled system, I considered a series of reactors with inter-stage heaters. Although the retentate and permeate streams are reheated to 650 °C, the products still remain in the streams and decreases the conversion at the next stage. Here I suggest another configuration which carries out separation of products at each stage as described in **Fig. 4-3c**. In addition to the product separation at each stage, it also adopts recycling feature of propane at the bottom of the C_3 splitter followed by distribution to 2^{nd} and 3^{rd} reactor stages. Therefore the fresh propane feed enters the 2^{nd} and 3^{rd} reactor stages. The recycle process keeps running so that overall 100% of propane conversion can be achieved for all conditions similar to the simple recycled system. The difference in the PDH conversion of each PBR and PBMR condition has clear effects on the downstream separation processes. As shown in **Fig. 4-30**, the propane flow rates at the feed stream of the C_3 splitter, which is the same as the recycled propane amount, show the most with the PBR condition. The energy duties for C_3 splitter and other heating/cooling energies are also calculated and summarized in **Table 4-4 and 4-5.** I observed the same trend of C_3 splitter and overall energy duties as increasing sweep flow rates in the PBMR system. However, when the results are compared with the simple recycled system, it is found that carrying out the product separation at each reactor stage requires more energy for both C_3 splitter and other heating/cooling streams. Although the fresh propane can be used for the 2^{nd} and 3^{rd} reactor stages, each propane feed undergoes only one reactor stage in parallel. Since all outlet streams of each stage go to downstream separation for product removal, the separation load should increase. On the other hand, the simple recycle system provides continuous PDH reaction in series, which gives more

propylene production and less propane is recycled and thus decreasing the separation energy and reheating the streams. This provides the important fact that reactors in series with a simple recycle system should be better than the use of parallel reactors.

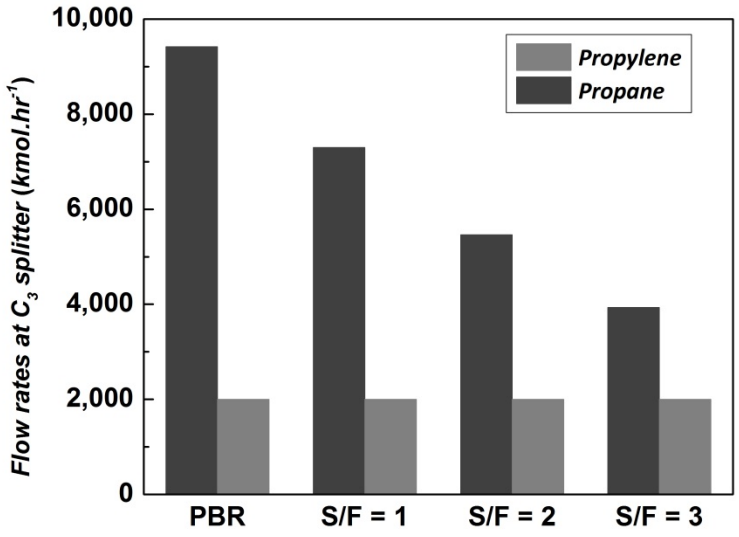

Fig. 4-30. Flow rates entering C3 splitter in recycled system with product separation at each stage.

Table 4-4. Reboiler and condenser heat duties of C_3 splitter (200 stages).

	Sweep/Feed	Reboiler (MW)	Condenser (MW)	Net duty (MW)	Reflux ratio
Conventional PBR	-	507	470	37	70
PBMR	1	400	371	30	55
	2	322	298	24	44
	3	251	232	19	34

Table 4-5. Heating and cooling duties for feed/sweep and retentate/permeate streams.

	Sweep/Feed	Heating (MW)		Cooling(MW)	
		Feed	Sweep	Retentate	Permeate
Conventional PBR	-	283	-	182	-
PBMR	1	205	32	158	113
	2	165	63	127	227
	3	131	95	101	342

4.5. Conclusions

The modeling studies using a 2D PBMR PDH model were carried out. The different types of mass and heat transport *Pe* play important roles in radial dispersion, membrane permeation, and temperature drop. Hollow fiber type ceramic supports should be considered for scaled-up system to achieve high PDH performance by minimizing the deleterious effect of radial dispersion, increasing the membrane surface area to catalytic volume ratio, and thus having more effective membrane permeation. Also the total volume of the PBMR is greatly reduced when the hollow fiber type membranes are used, compared with conventional ceramic tube-supported membranes. This PBMR volume is even lower than the volume of the PBR for the same target propylene production. The PBMR system also enhances the PDH performance by removal of the product through the membrane permeation as well as providing additional heat from the high temperature sweep gas to the catalytic site.

ASPEN-FORTRAN simulations of PBMR PDH plant were carried out. The 2D PBMR PDH model is incorporated into ASPEN flowsheet where three adiabatic PBMRs are used with the inter-stage heaters and downstream separation processes. I compared non-recycled and recycled system of PDH plant configuration. For the non-recycled system in the PBMR, less propane feed with less overall energy can be used for the same propylene production as the PBR with more propane feed. In the simple recycled system, the PBMR provides less separation energy with more sweep flow rate, but it levels off at higher sweep flow range. Considering the overall net energy duty of this system, there should exist better operating condition with the sweep gas range of 1.5 ~ 2 of S/F ratio. I also suggest another recycled system where it carries out product removal at the downstream separation after each reactor stage. Although this configuration shows the same trend of energy saving with increasing sweep flow rates, it requires more energy for separation and other heating/cooling processes than the simple recycled system.

This modeling study clearly demonstrates that PBMR configuration has benefit in terms of both PDH performance and savings in energy cost of downstream separation in a less volume of the reactor. The enhancement of conversion leads to saving more energy for downstream separations although the PBMR system requires additional energy for handling the use of sweep gas. Overall the PBMR system requires considerably less energy compared with PBR system. This modeling study reveals that the PBMR system using hollow fiber type membranes should provide excellent opportunities for a novel PDH process.

CHAPTER 5

NEW CATALYSTS FOR PROPANE DEHYDROGENATION: A GALLOSILICATE MFI ZEOLITE WITH PERTURBED ACIDITY

5.1. Introduction

Ga-containing zeolites have been extensively studied as discussed in Chapter 1. It is evident that there are many reports describing the development and characterization of Ga containing MFI catalysts for propane conversion, although most of the work has focused on maximizing aromatic selectivity. Several reports addressed the initial PDH step in the propane aromatization sequence, but limited to low propane conversions. For instance, Mériaudeau et al. performed propane dehydrogenation at ~1% conversion levels, applying HZSM-5 and gallosilicate [145]. Hart et al. studied selective dehydrogenation catalysts with few or no zeolite protonic sites via Ga and In addition to HZSM-5 [184]. One may surmise that Ga modified MFI catalysts have not been widely recognized for PDH itself due to the low propylene selectivities observed at high conversions, with the catalysts favoring propane aromatization under these conditions. Here, I develop a synthesis method that creates Ga Lewis acid sites in aluminum-free, gallosilicate MFI without post treatments such as Ga impregnation, ion-exchange or heat treatment. Specifically, 3-mercaptopropyl-trimethoxy silane (MPS) is used as a functional silane during the gallosilicate MFI zeolite synthesis. Previously, MPS has been demonstrated to

incorporate metal clusters in the zeolite channels during zeolite synthesis [185-187]. It was proposed that the Si species in MPS is embedded into the zeolite framework after hydrolysis of the trimethoxy groups while preserving the Si-mercaptopropyl linkage. At the same time, the thiol group on the 3-mercaptopropyl moiety interacts with metallic ions (such as Pt^{2+} or Cd^{2+}) in the zeolite synthesis solution, thereby facilitating their incorporation into the zeolite pores during crystallization. Here I extend this approach to the use of Ga additives during the synthesis of MFI zeolites and report a detailed structural and catalytic (PDH) characterization of the Ga-MFI catalysts prepared by this technique. This work is based upon the hypothesis that the altered mechanism(s) of Ga incorporation induced by the addition of MPS would lead to a different acid site profile and catalytic behavior. In this regard, the new gallosilicate MFI catalysts prepared here have lower Brønsted acid site concentrations, enhanced Lewis acid sites concentrations, and give high propylene selectivities at elevated conversions with concomitant high propane conversion rates.

5.2. Experimental methods

5.2.1. Catalyst preparation

Gallosilicate MFI with MPS (MG05, MG11, MG16): MPS-Ga MFI was prepared based on a typical hydrothermal zeolite MFI synthesis with the addition of 3-mercaptopropyl-trimethoxysilane (MPS, Sigma-Aldrich) and Ga nitrate as a metal source. First, 10.2 g of tetraethylorthosilicate (TEOS, 98% reagent grade, Sigma-Aldrich) was added to 16 g of tetrapropylammonium hydroxide (TPAOH, 1 M Sigma-Aldrich) solution

with 27 g of DI water, followed by stirring overnight. Then, MPS was added to the solution and stirred for 3 h. Subsequently, 0.5 g of Ga nitrate (Ga(NO3)3.xH2O, 99.9%, Sigma-Aldrich) was added and the mixture was kept stirring an additional 3 h. The final molar composition was 1 SiO_2: 0.32 TPAOH: 45.4 DI water, with the MPS amount adjusted to achieve different MPS/Ga ratios. Three gallosilicates were synthesized, namely MG05, MG11, and MG16 for which MPS/Ga ratios in the synthesis gel were 0.54, 1.1 and 1.6 respectively. The solution was heated at 423 K for 4 days in a Tefron-lined autoclave. The obtained zeolite crystals were washed with DI water, recovered by centrifuge and dried overnight at 343 K, followed by calcination at 823 K for 10 h under static air conditions with a heating rate of 1.5 K/min.

Gallosilicate MFI without MPS (MG0, HG): For a comparison, two types of Ga-MFI with no addition of MPS were also synthesized. H-form gallosilicate (H-gallosilicate, HG) was prepared by a typical hydrothermal synthesis to form the sodium exchanged gallosilicate (Na-gallosilicate). The Ga nitrate was added to TPAOH solution and stirred for 3 h. Then, TEOS and NaOH were subsequently added dropwise to the solution. The hydrothermal synthesis conditions, drying and calcination steps of the Na gallosilicate were the same as for MPS-gallosilicate MFI samples described above. The obtained Na-gallosilicate powder samples were then ion-exchanged in 1M NH_4NO_3 solution at 353 K for 3 h, followed by washing and drying. The ion-exchange was repeated 3 times. The NH_4 form gallosilicate was then calcined at 823 K for 4 h to remove NH_3, producing the catalyst HG. Another type of gallosilicate MFI (MG0) was also prepared by the same method as MPS-Ga MFI but without the MPS addition step and with no further ion-exchange.

Ga impregnated pure-silica MFI (Ga/pure-silica MFI, GS): Ga impregnated into the pure-silica MFI zeolite was also prepared. Pure-silica MFI was synthesized with the same synthesis method as the MPS-gallosilicate MFI without addition of Ga nitrate and MPS. Then, Ga impregnated pure-silica MFI was prepared by wet impregnation of Ga nitrate in an ethanol solution, followed by drying in a rotary evaporator and calcination under the conditions noted above. For a comparison with a Cr catalyst similar to those applied commercially, a Na doped chromia on alumina catalyst was prepared by incipient wetness impregnation with a composition of 20 wt % Cr and 1 wt % Na, which was provided by The Dow Chemical Company.

The catalysts used in this study are listed in **Table 5-1**. All samples were calcined at 823 K for 10 h under static air conditions with a heating rate of 1.5 K/min prior to use as catalysts.

Table 5-1. List of catalysts. All samples were calcined at 823 K for 10 h

Catalyst	Type	As-synthesized	MPS/Ga	Post treatment
MG05	MPS-Gallosilicate	TPA-Gallosilicate	0.54	None
MG11	MPS-Gallosilicate	TPA-Gallosilicate	1.1	None
MG16	MPS-Gallosilicate	TPA-Gallosilicate	1.6	None
MG0	Gallosilicate	TPA-Gallosilicate	No MPS addition	None
HG	Gallosilicate	Na-Gallosilicate	No MPS addition	Ion-exchange
GS	Ga/pure-silica MFI	TPA-silica MFI	No MPS addition	Ga impregnation

5.2.2. Catalyst characterization

Powder X-ray diffraction (XRD) measurements were carried out using a PANalytical XPert PRO diffractometer using a Cu Kα radiation with a scan step size of 0.0167 ° in the 2θ range of 5 – 50 °. The shape and size of the particles were characterized by a Hitachi SU8010 cold field emission scanning electron microscopy (SEM). The surface area, micro- and meso- pore volumes were obtained from N_2-physisorption measurements at 77 K using a Micromeritics ASAP 2020. The samples were degassed at 473 K for 12 h and free space analysis was performed using He prior to N_2 adsorption-desorption isotherm measurements for more accurate micro-pore analysis. The samples were re-degassed at 473 K to remove entrapped He before micro-pore analysis. The strength and concentration of the acid sites were determined by temperature programmed desorption of NH_3 (NH_3-TPD) in a U-shape fixed bed reactor using a Micromeritics Autochem II. The sample (about 0.11 g) was preheated at 773 K for 1 h followed by NH_3 injection at 373 K. Helium was used as the carrier gas a 25 mLSTP/min. The temperature was then elevated to 873 K and the desorbed NH_3 was detected by a thermal conductivity detector (TCD). Elemental analysis for Ga and Si was carried out by inductively coupled plasma-optical emission spectroscopy (ICP-OES, ALS Environmental, AZ) to ascertain the composition of each catalyst sample. For the samples synthesized in the presence of MPS, analysis for S was also completed by combustion at 1573 K followed by infrared spectroscopy detection (ALS Environmenal, AZ). Solid-state nuclear magnetic resonance (NMR) spectra of ^{29}Si and ^{71}Ga were obtained on a Bruker Avance III 400 spectrometer at a sample spinning speed 10 kHz. The ^{29}Si-NMR spectra were referenced with respect to 3-(trimethylsilyl)-1-propanesulfonic acid at 0

ppm. For the ^{71}Ga-NMR spectra, aqueous $Ga(NO_3)_3$ solution at 0 ppm was used for calibration.

The ratios of Brønsted to Lewis acid sites were estimated by Fourier transform infrared spectroscopy (FT-IR) of samples containing adsorbed pyridine on a Thermo Scientific Nicolet 8700 spectrometer. The catalysts were activated at 773 K under vacuum for 6 h. A background spectrum was measured after cooling down to 423 K and then pyridine was admitted to the catalyst at the same temperature. The FT-IR spectra of the hydroxyl stretching region were also obtained before dosing of pyridine. The pyridine was adsorbed for 1 h to allow equilibration, and the physisorbed pyridine was removed under vacuum at 10^{-6} mbar overnight. The FT-IR spectra of the pyridine adsorbed samples were measured after evacuation at different temperatures, specifically 423, 523, 623, and 723 K. The concentration of Brønsted acid sites was also measured by temperature programmed desorption of isopropylamine (IPA-TPD) [188-190]. A sample (0.1 g) was loaded in a fixed bed and activated at 773 K for 3 h with 100 mL/min of N_2 flow to remove remaining water. After cooling to 373 K, 50 μL of IPA was introduced into the N_2 carrier gas flow followed by overnight continuous N_2 flow to remove physisorbed IPA. Then, the TPD measurements were carried out at a heating rate of 10 K/min and the concentration of desorbed propylene resulting from decomposed from IPA on the Brønsted acid sites was recorded using Pfeiffer Vacuum mass spectrometer (MS).

5.2.3. Catalytic measurements

Catalytic PDH was performed at 873 K under atmospheric pressure. The catalyst (212-400 μm pellet size) was placed in a quartz tube fixed bed reactor and heated under N_2 flow to the reaction temperature. The concentration of C_3H_8 in the feed was 5 % with the balance N_2. The total feed flow rate was 20 mLSTP/min. During the PDH reaction, the product stream was analyzed by an on-line GC (Shimadzu GC2014) using a flame ionization detector (FID) for hydrocarbon products and thermal conductivity detector (TCD) for H_2. The propane conversion and product selectivities were calculated based on the feed conditions and the concentration of the products as follows:

$$C_3H_8 \text{ conversion } (\%) \equiv \frac{C_3H_8^{in} - C_3H_8^{out}}{C_3H_8^{in}} \times 100$$

$$\text{Product selectivity } (\%) \equiv \frac{Product^{out}}{C_3H_8^{in} - C_3H_8^{out}} \times 100$$

5.3. Results and discussion

5.3.1. Physical properties

The MFI structure was confirmed by XRD for all the samples used in this study. Comparing the pure-silica and gallosilicate MFI samples, the intensities of the diffraction peaks decreased with Ga incorporation, as observed in **Fig. 5-1**. All the gallosilicate MFI samples in **Fig. 5-2** showed similar crystallinity, although MPS addition slightly decreased peak intensities. Most of the gallosilicate MFI catalysts showed small spherical crystallite shapes, (**Fig. 5-3)**, which is typical for gallosilicate samples, being similarly

observed in past studies [140, 150, 191]. The GS material formed particles with very similar shape to the pure-silica MFI (**Fig. 5-3**). The particle sizes were mostly ca. 200 nm for all the samples, with no significant difference caused by different amounts of MPS added.

The physical properties of the samples are summarized in **Table 5-2**. No significant qualitative trend was observed in micropore volume and surface area of the MG samples. A slightly different range of pore volume and surface area was observed for the HG and GS samples compared with the MG samples, which is probably due to the different preparation methods employed. The Si/Ga ratio was obtained by ICP-OES analysis and all of the catalysts showed similar total Ga content.

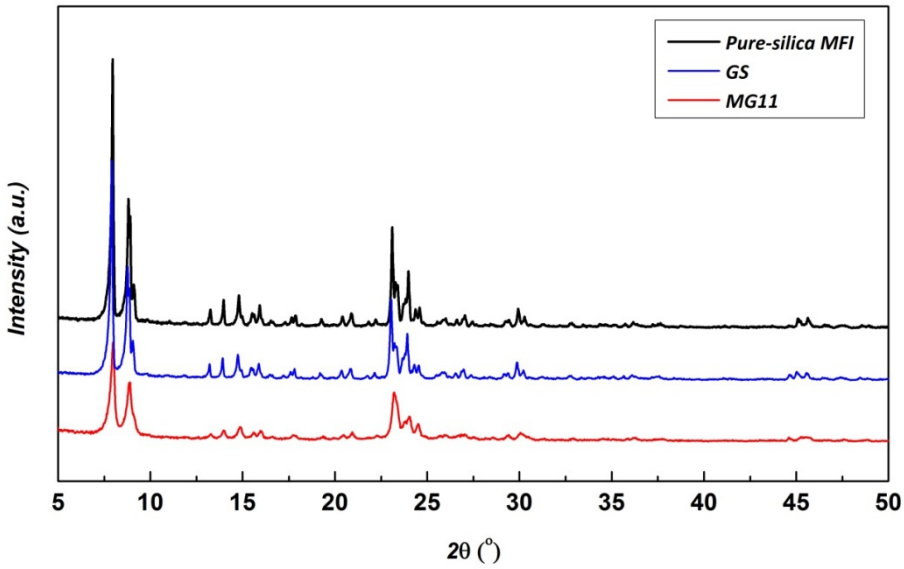

Fig. 5-1. XRD patterns of silicalite-1, GS and MG11. Pure-silica MFI, GS, MG11 from top to bottom.

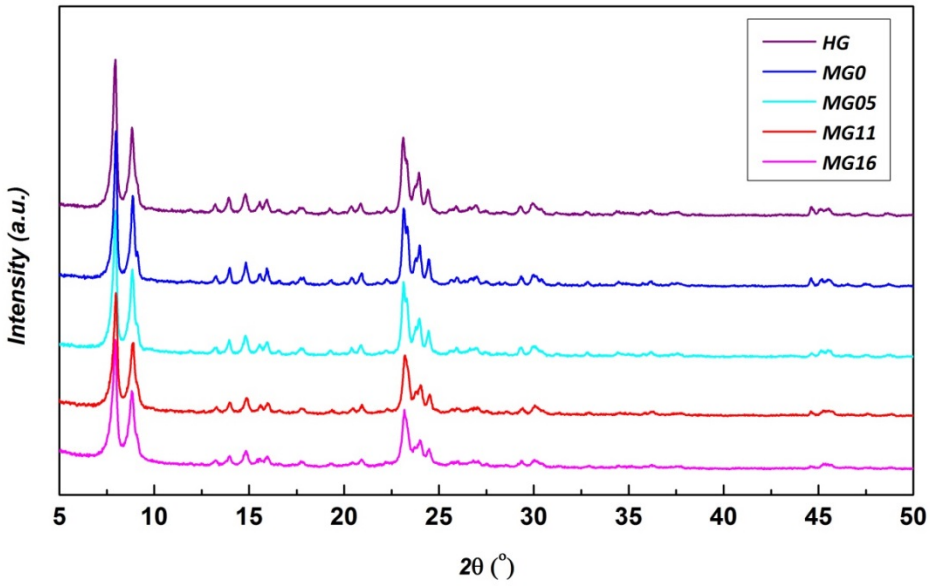

Fig. 5-2. XRD patterns of gallosilicate MFI samples including HG, MG0, MG05, MG11, MG16, from top to bottom.

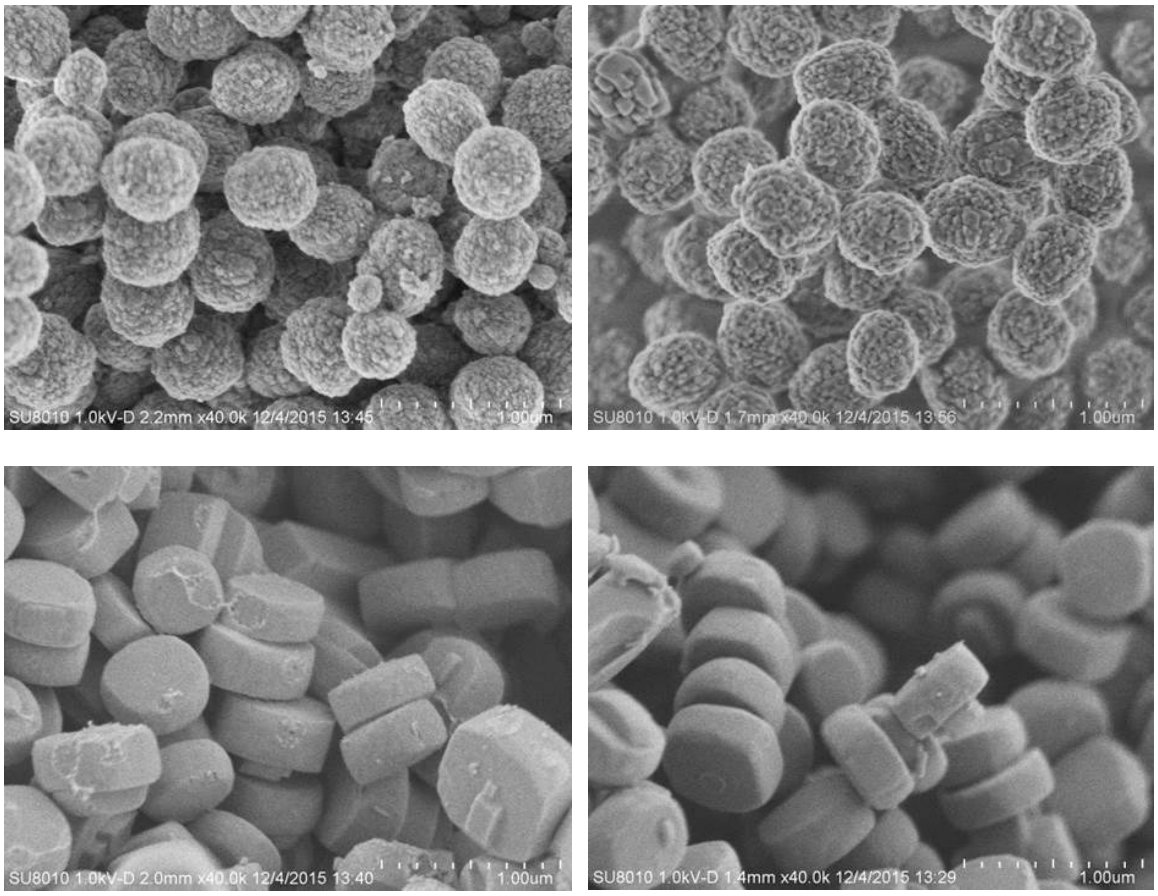

Fig. 5-3. SEM images of MG11 (left top), MG0 (right top), GS (left bottom), and pure-silica MFI (right bottom).

Table 5-2. Physical properties of catalysts.

Catalyst	V_{micro}[a] (cm^3/g)	V_{meso}[b] (cm^3/g)	S_{micro}[a] (m^2/g)	S_{total}[c] (m^2/g)	Si/Ga[d]
MG16	0.13	0.12	273	500	35
MG11	0.15	0.08	315	470	37
MG05	0.13	0.08	289	402	34
MG0	0.14	0.05	306	383	36
HG	0.10	0.09	220	365	33
GS	0.11	0.11	213	388	42
Pure-silica MFI	0.12	0.09	245	318	∞

[a] Calculated by t-plot method. [b] Calculated by BJH method. [c] Calculated by BET method. [d] Obtained by ICP-OES

5.3.2. Acid site measurements

The NH_3-TPD profiles of the Na and H form gallosilicate MFI samples were compared to confirm the presence of protonic acid sites after ion-exchange. In **Fig. 5-4,** both low temperature (*l*-peak at 450 K) and high temperature (*h*-peak at 580 K) features were observed for H-gallosilicate MFI (HG) while the *h*-peak was overlapped with *l*-peak for the Na-gallosilicate MFI. The *l*-peak is attributed to physisorbed, weakly held ammonia rather than representing acid sites [150, 157]. The *h*-peak corresponds to Brønsted acid sites generated after ion-exchange. The NH_3-TPD profiles of the gallosilicate MFI materials (MG) synthesized without alkali metal also show an *h*-peak at 550 K (**Fig. 5-5)**. Similar to the HG sample, this *h*-peak can be also considered as Brønsted acid sites generated after TPA ions were removed during calcination. However,

the peak intensities were much lower than for HG, indicating fewer protonic sites formed without the ion-exchange step.

Furthermore, additional peak shoulders at higher temperatures, ca. 700 K, were observed. This peak shoulder at high temperature was also reported in past studies and assigned to strong Lewis acidic Ga species [137, 150]. Miyamoto et al. observed a similar peak shoulder during NH_3-TPD at 700 – 900 K of samples with increased Ga content, and also found an additional *h*-peak when Ga was impregnated into the gallosilicate. Similarly Rodrigues et al. confirmed the presence of strong Lewis acid sites in Ga impregnated HZSM-5 in which a significant TCD signal in the NH_3-TPD experiment still remained at temperatures of more than 800 K, whereas the signal returned to the baseline in the case of HZSM-5. Ga impregnated into pure-silica MFI did not yield a material with strong Lewis acidity in two previous papers [137, 150], indicating that the presence of Brønsted acid sites was necessary to generate the strong Lewis acid sites during Ga incorporation. Rodrigues et al. suggested from their EXAFS spectra of Ga/HZSM-5 that atomically dispersed oxidic Ga species in ion-exchange positions should be ascribed to the strong Lewis acid sites, whose concentration increased with the number of framework Al sites. From the TPD profiles of the MG materials in this study, the intensity of the high temperature peak shoulder increased with the amount of MPS added in the synthesis gel. This suggests that the thiol group in the MPS ligand interacts with Ga in the zeolite synthesis gel and this can influence the speciation of Ga in the final material. Specifically, MPS-induced formation of extra-framework Ga sites is hypothesized. Based on the fact that the TPD peak intensities at 550 K showed almost no difference with and without MPS addition, it appears that the MPS ligand had little effect on the formation of

framework Ga Brønsted sites. This is consistent with the proposed mechanism of metal incorporation *via* MPS, which is expected to result in enhanced incorporation in the pores rather than in the framework. Considering the proposed bifunctional reaction mechanism of PDH requiring both Brønsted and Lewis acid sites, where Lewis acid sites play a crucial role, the MG samples in this study were thought to be good candidates for PDH, providing a greater number of strong Lewis acid sites even without post impregnation or heat treatment steps.

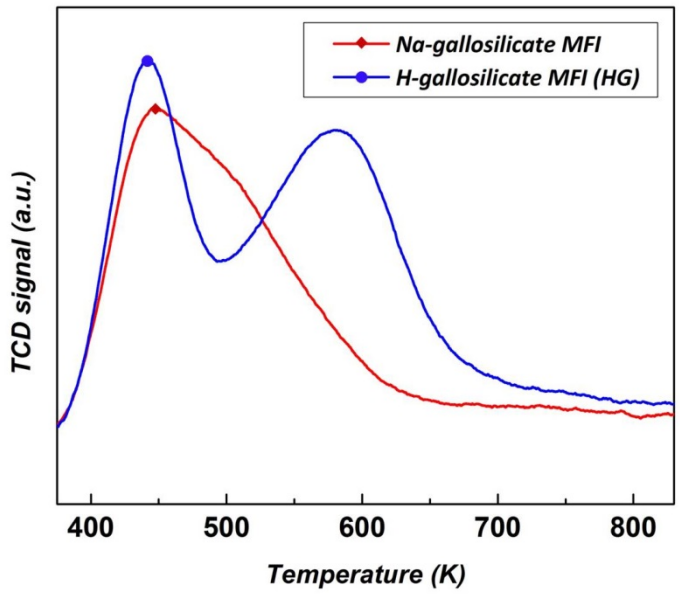

Fig. 5-4. TPD profiles of Na-gallosilicate MFI (before ion-exchange) and H-gallosilicate MFI (HG, after ion-exchange).

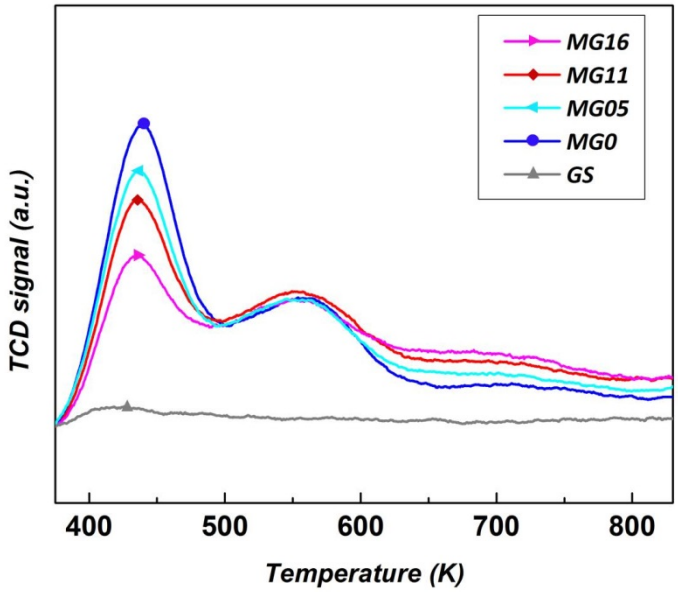

Fig. 5-5. TPD profiles of MG samples synthesized in the absence of alkali metal ions.

Ammonia TPD analysis does not provide any information distinguishing Lewis vs. Brønsted acid sites. To this end, the acid site distribution of an MG catalyst (MG11) containing adsorbed pyridine was analyzed by FT-IR spectroscopy alongside the spectrum of the sample made without MPS addition, MG0. The FT-IR spectra of the samples before pyridine dosing are displayed in **Fig. 5-6**. The peaks at 2100 – 1500 cm^{-1} are assigned as overtone bands of the zeolite framework [150, 192]. In the hydroxyl stretching region from 3000 – 3750 cm^{-1}, a peak at 3617 cm^{-1} was observed for both catalysts, indicating that they both have bridged Brønsted acid sites from framework Ga [91, 145, 151]. The higher frequency of these Brønsted acid sites than typical Al bridged protonic sites is consistent with the less acidic character of the Ga bridged sites[91]. For both samples, there was a broad band between 3000 – 3600 cm^{-1} corresponding to

hydrogen bonded silanol groups on the external surface or hydrogen bonding in hydroxyl nests in defect sites associated with missing T atoms [151]. Another peak for a hydroxyl group attached to extra-framework Ga at 3660 – 3670 cm^{-1} was also observed [93, 137, 147, 151], but the peak overlapped with internal and terminal silanol groups at 3720 and 3740 cm^{-1} [137, 151].

FT-IR spectra of the catalysts containing adsorbed pyridine were also measured after evacuation at temperatures of 423, 523, 623, and 723 K. The peak at ca. 1540 cm^{-1} corresponds to the pyridinium ion, PyH^{+}, formed after pyridine interacts with Brønsted acid sites. Pyridine adsorbed on Lewis acid sites gives a characteristic band at ca. 1450 cm^{-1} [137, 150]. The band at ca. 1445 cm^{-1} has been assigned to hydrogen bonded pyridine [150]. As shown in **Fig. 5-7**, significant intensity of the 1458 cm^{-1} band associated with Lewis acid sites still remained after evacuation at high temperatures up to 723 K, indicating the presence of some very strong Lewis acid sites, which is consistent with the profiles (**Fig. 5-5**) from NH_3-TPD. Similar results were previously observed when Ga was impregnated into HZSM-5 and the strong Lewis acid sites were assigned to highly dispersed Ga species [137, 150]. The above findings clearly confirm key differences in the acid site distribution between gallosilicate MFI materials prepared with and without MPS addition (**Fig. 5-8)**. The ratio of the concentrations of Brønsted and Lewis acid sites (B/L) was obtained for each sample by using molar extinction coefficients for MFI zeolites from the literature [193]. **Fig. 5-8** quantifies the difference in B/L ratio between the two types of gallosilicate MFI materials. MPS addition led to more strong Lewis acid sites, thus decreasing the B/L ratio.

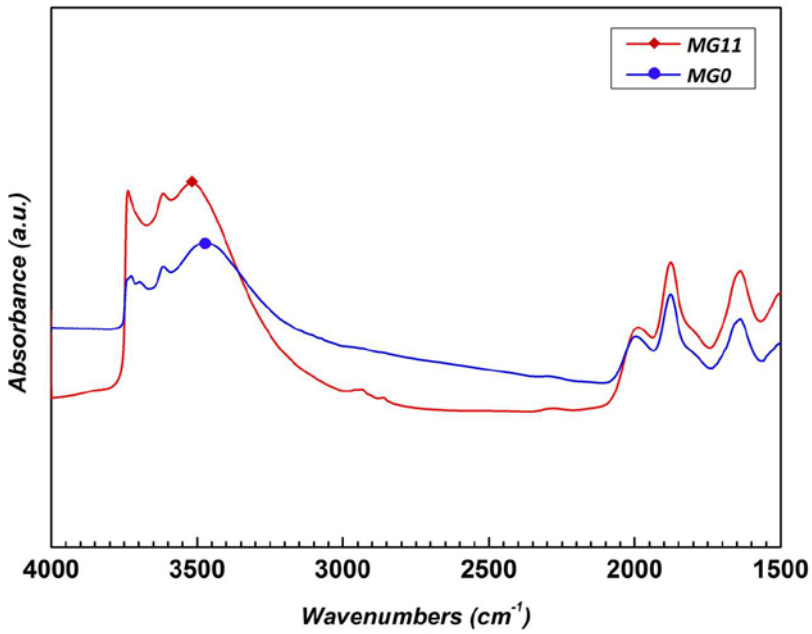

Fig. 5-6. FT-IR spectra of gallosilicate MFI materials prepared with and without MPS addition (MG11, MG0).

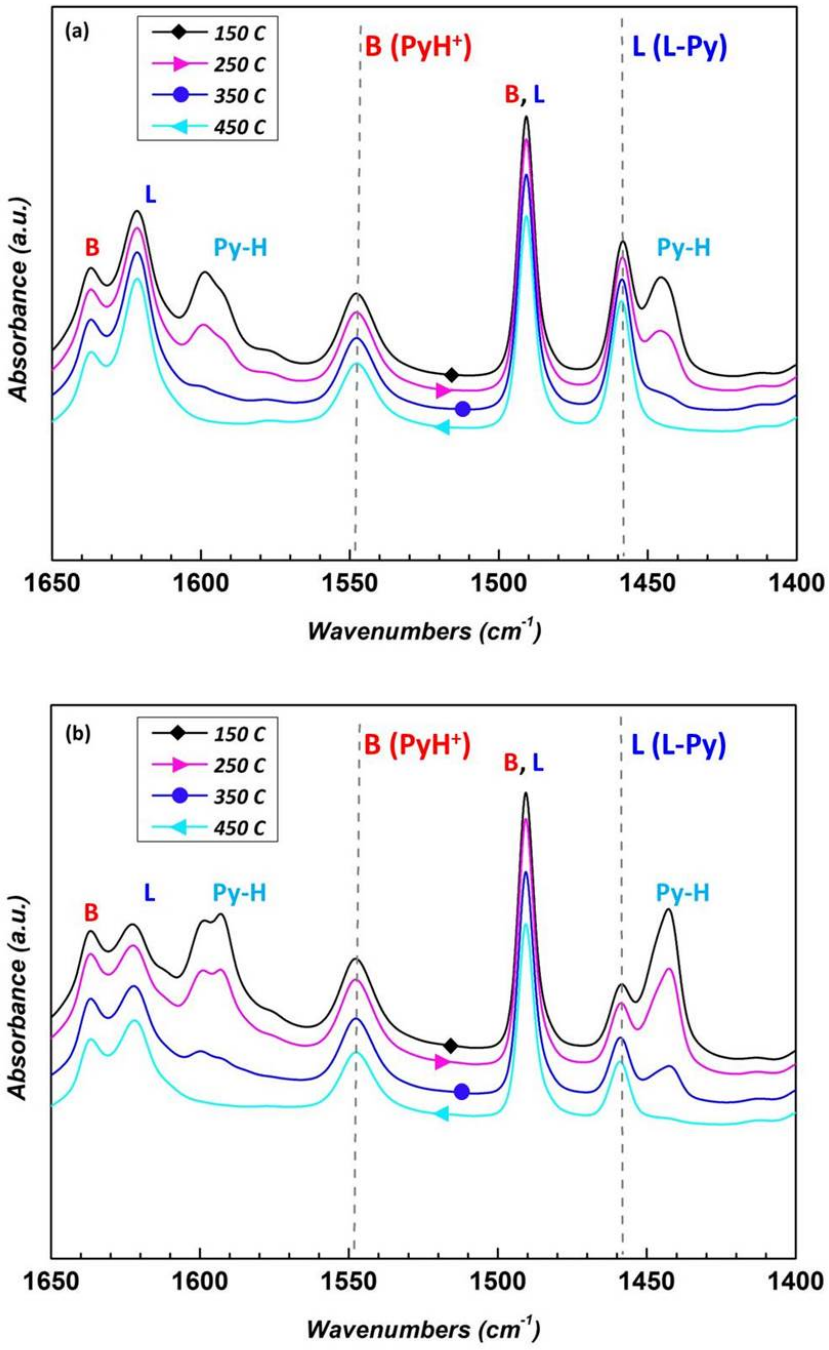

Fig. 5-7. FT-IR spectra of pyridine adsorbed (a) MG11 and (b) MG0 at different evacuation temperatures. The B, L, and Py-H at each peak position represent Brønsted acid sites, Lewis acid sites and hydrogen bonded pyridine, respectively.

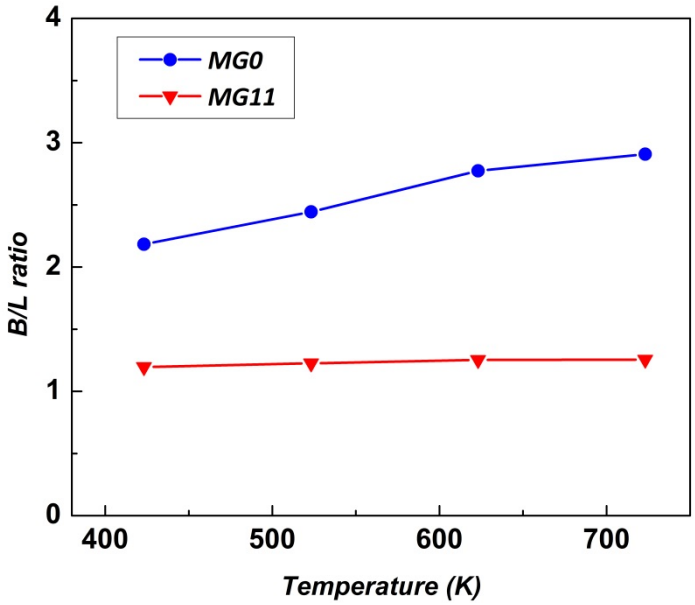

Fig. 5-8. Comparison of B/L ratio obtained from FT-IR spectra of pyridine adsorbed gallosilicate MFI samples.

Temperature programmed desorption of isopropylamine (IPA-TPD) was also carried out to assess the concentration of Brønsted acid sites present at low and moderate desorption temperatures, independent of the Lewis acid sites. In **Fig. 5-9**, the main peak in the temperature range 600 – 700 K is assigned to propylene from adsorbed IPA on the Brønsted acid sites [188-190], while the peak below 600 K is assigned to propylene from weakly held IPA adsorbed on internal or external silanol groups [194]. There was an additional peak shoulder at high temperature, above 700 K, which was not observed in the HG sample. The same peak at high temperature was also previously reported for the reduced form of Ga impregnated HZSM-5 [195, 196]. According to Ausavasukhi et al., the new peak at high temperature was observed after reduction of Ga/HZSM-5 in H_2

while no peak was seen in the same temperature range without H_2 treatment. The authors suggested that the peak can be associated with hydroxyl groups on extra-framework Ga sites. Considering that the peak shoulder intensities of the MG samples increased with MPS content in the synthesis gel, the MG samples may have these extra-framework Ga species interacting with decomposed IPA, where the liberated propylene from IPA decomposition at low temperature at a Brønsted site re-adsorbed on these strong extra-framework Ga Lewis sites. It should be noted that even without MPS addition, some amount of these Ga sites were generated, considering the small peak shoulder in MG0.

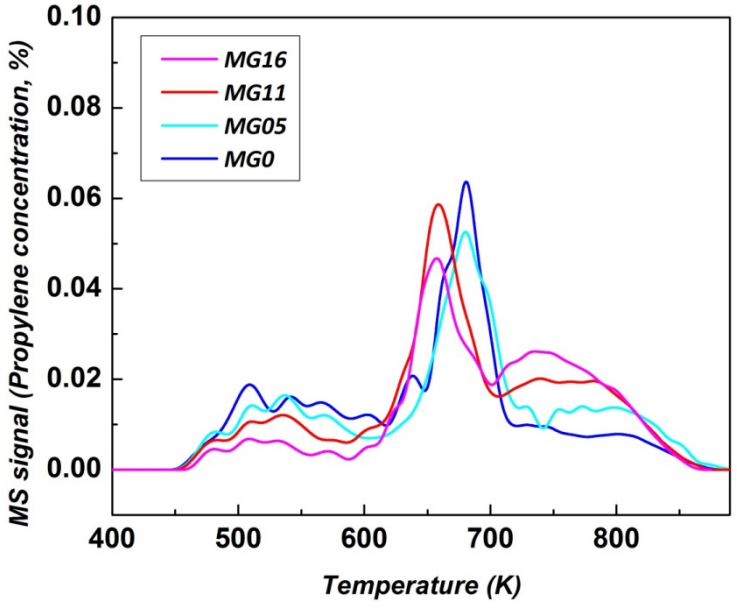

Fig. 5-9. IPA-TPD results for the MG catalyst samples.

The acid site measurements are summarized in **Table 5-3**. The acid site concentrations were determined by a combination of IPA-TPD-MS, pyridine IR, and NH_3-TPD, as mentioned above. The acid site concentrations were also quantitatively estimated from NH_3-TPD by calibrating NH_3 concentrations in the TCD after deconvolution of the *h*-peak1 and *h*-peak2. Assuming the *h*-peak1 was from the adsorbed NH_3 on the Brønsted acid sites and the *h*-peak2 was from the strong Lewis acidic Ga sites, the concentrations and distributions of the acid sites were qualitatively well matched with the results of IPA-TPD and the B/L ratios from pyridine FT-IR. The lower level of Brønsted acid sites from IPA-TPD compared to NH_3-TPD can be attributed to the re-adsorption of propylene liberated from Brønsted acid sites at low temperatures on extra-framework Ga species at higher temperature, as discussed above. The Brønsted acid site concentrations of the MG samples were lower than for the HG sample, likely due to the combined effects of the absence of alkali cations (e.g. Na^+) during the gallosilicate synthesis and the presence of MPS in the synthesis, as observed from comparison of the IPA-TPD and NH_3-TPD results of MG0 to MG16. In parallel, the MPS addition generated more Lewis acid sites, as suggested by the high temperature peak shoulders in the NH_3-TPD and B/L ratios in the pyridine FT-IR results.

Table 5-3. Summary of acid site analysis results.

Catalyst	Brønsted acid sites from IPA-TPD (μmol/g)	Acid sites (B/L)[a] from NH_3-TPD (μmol/g)	B/L ratio from NH_3-TPD
MG16	94	133/108	1.2
MG11	107	135/91	1.5 (1.3[b])
MG05	113	143/75	1.9
MG0	113	143/43	3.3 (2.9[b])
HG	349	370/64	5.8

[a] B indicates concentration of Brønsted acid sites derived from the first high temperature peak, L is the concentration of Lewis acid sites from the peak shoulder at high temperature range. [b] B/L ratios are from pyridine FT-IR at high temperature (723 K) data in Fig. 5-8.

The Si and Ga species present in the catalysts were analyzed by NMR measurements. **Fig. 5-10** shows the ^{29}Si-NMR spectra of the four MG samples. The peak at ca. -113 ppm is assigned to framework Si(0Ga) species, while the signal at -105 ppm is from framework Si(1Ga) atoms, indicating the presence of framework Ga in the gallosilicate MFI samples [126, 140, 197]. The MG samples showed almost the same relative intensities of these two peaks, suggesting that the MG samples have similar levels of framework Ga. Additionally, in the NMR spectrum of the as-synthesized MG11 sample, there was an additional peak at ca. -70 ppm, which was not observed in MG0 (**Fig. 5-11**). This peak can be assigned to T_3 species [R-Si-$(OSi)_3$], which was also reported in Wong et al. for samples synthesized in the presence of MPS [186, 198-200]. This confirms the condensation of the methoxysilane groups in MPS with the MFI framework during the synthesis, as separate amorphous phases were not observed by SEM or XRD. This T_3 species then disappeared after calcination.

The presence of framework Ga was also confirmed by the large peak at ca. +150 ppm in the ^{71}Ga-NMR spectra (**Fig. 5-12**), representing Ga species in tetrahedral coordination [144, 201-203]. For the gallosilicate MFI samples used in this study, the peaks associated with extra-framework Ga were not routinely observed. Indeed, small concentrations of extra-framework Ga are difficult to detect by ^{71}Ga-NMR, especially if they are not symmetric species, as previously discussed. However, for the MG16 sample, which has the largest amount of Lewis acidic Ga sites based on acidity analysis, a small peak at ca. 0 ppm was observed. This confirms the presence of extra-framework Ga in this sample, with the amount likely just above the threshold of detection in the NMR measurements. The NMR and pyridine FT-IR results indicate that although the MPS itself was likely cross-linked into the zeolite framework during the synthesis, it did not affect the incorporation of Ga in tetrahedral framework sites but instead it generated additional Lewis acidic Ga sites.

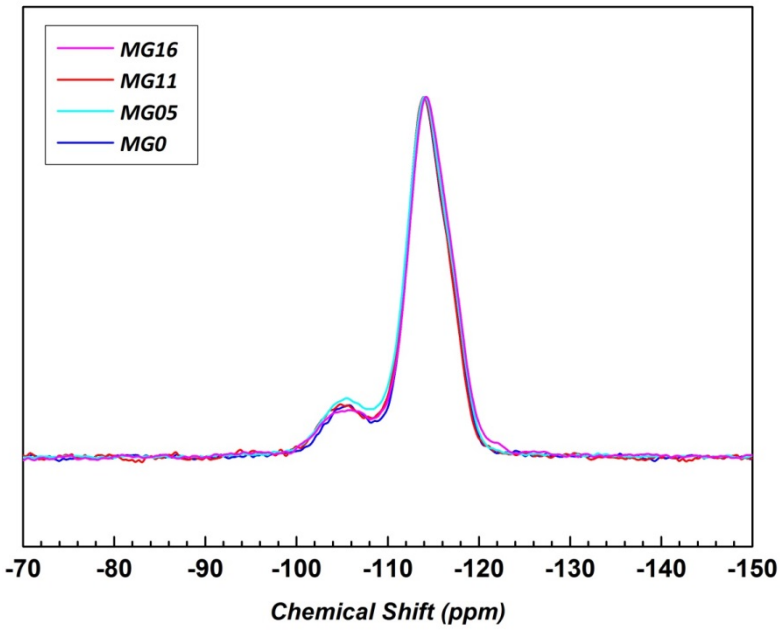

Fig. 5-10. ^{29}Si-NMR spectra of the MG catalysts.

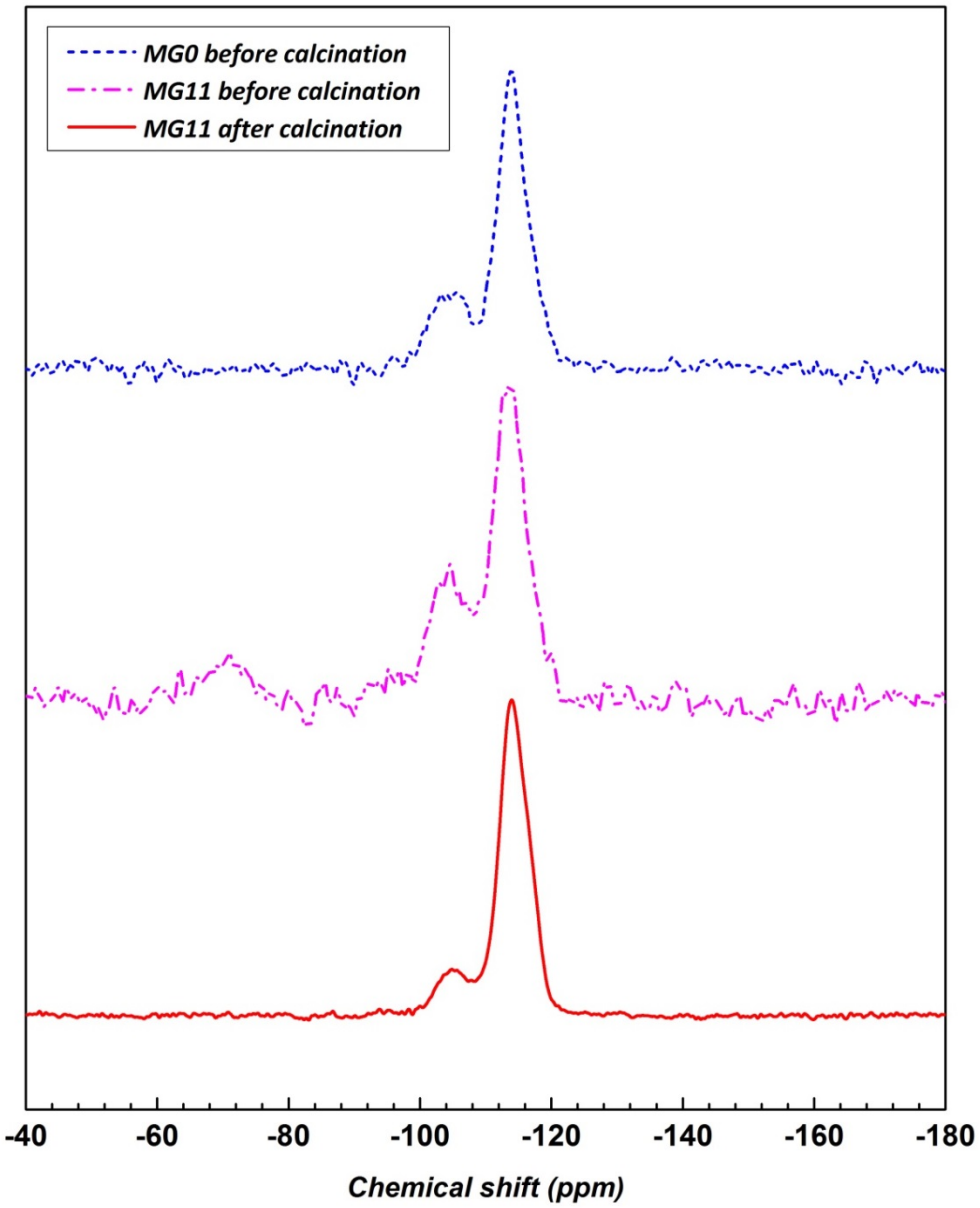

Fig. 5-11. 29Si-NMR spectra of MG samples before and after calcination. NMR s pectrum of MG0 after calcination looks similar to MG11 after calcination, as sho wn in Fig. 5-10.

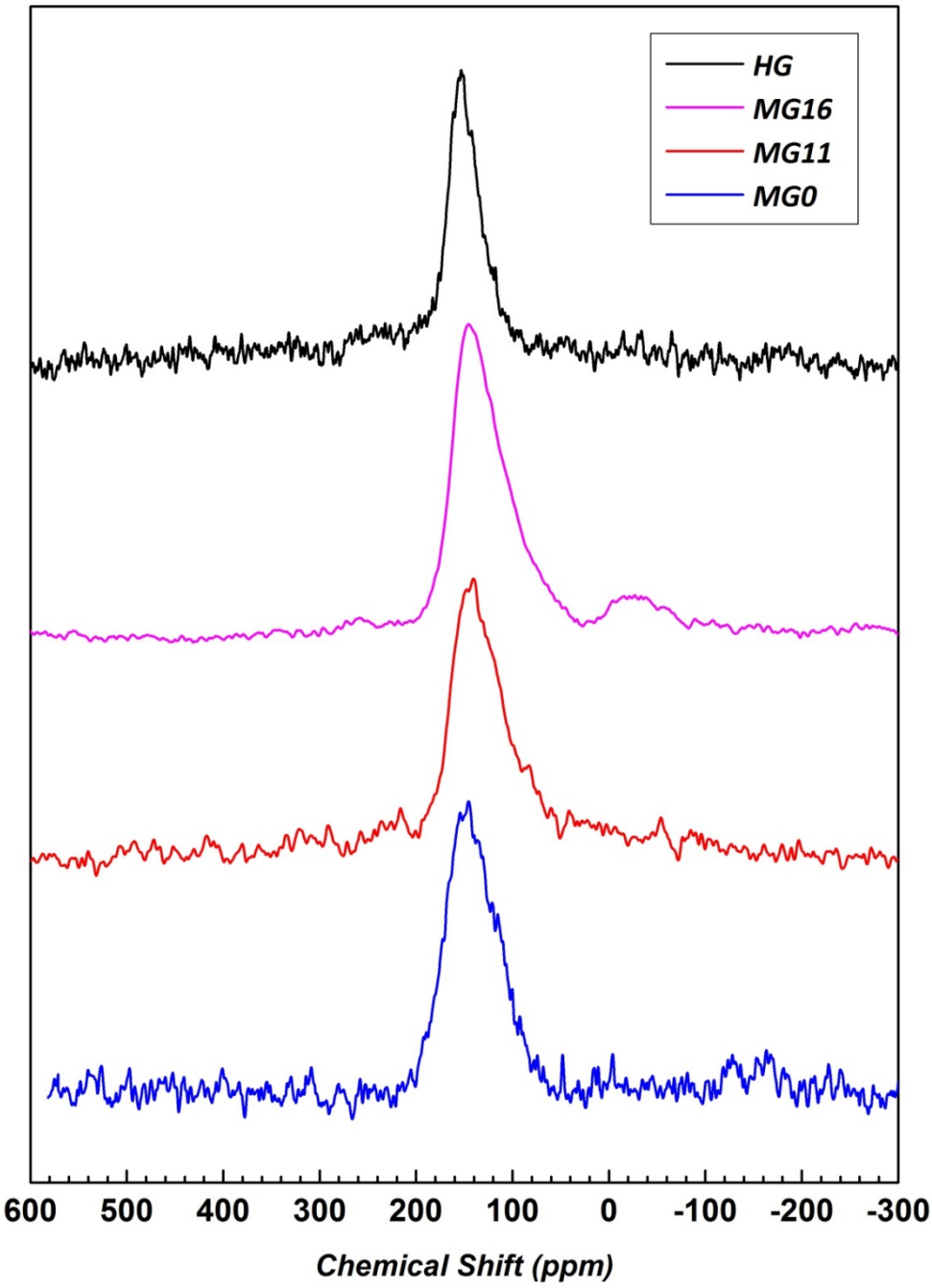

Fig. 5-12. 71Ga-NMR spectra of four gallosilicate MFI samples.

5.3.3. PDH performance

The catalytic PDH performance of the gallosilicate MFI catalysts was first compared at a common low conversion level of ca. 10%. The catalytic measurements were performed at 873 K and atmospheric pressure in a continuous quartz tube reactor, which was connected to an on-line GC. The W/F values (W, weight of catalyst, g: F, feed flow rate, mL/s) were adjusted for each catalyst to compare activity and selectivity at similar propane conversions. The time on stream data for propane conversion and the propylene selectivities for each catalyst were recorded for 5.5 h, as shown in **Fig. 5-13**. Different ranges of propylene selectivities were observed for the catalysts in a common propane conversion level of 9 - 13%. The on-stream propylene selectivities are shown in **Fig. 10b**, whereas the average propylene selectivities and dehydrogenation to cracking ratios (D/C) are compared in **Fig. 5-14**. It is clear that there is an increasing propylene selectivity with less cracking in the MPS-gallosilicate MFI samples compared to the catalyst made without MPS addition. Furthermore, the propylene selectivity increased with increasing MPS content in the catalyst synthesis gel. The initial propane conversion rates (expressed as TOFs) also increased from MG0 to MG16 (**Fig. 5-15)** where the MG16 catalyst shows more than a three-fold increase in activity compared to the MG0 catalyst. The propane activity was calculated based on Brønsted acid sites (**Fig. 5-15a**) or the total acid sites from NH_3-TPD experiments (**Fig. 5-15b**). In **Fig. 5-15a**, different propane conversion rates were observed for the MG catalysts with MG16 showing the highest activity per Brønsted acid site, which may be attributed to its large numbers of strong Lewis acid sites. These data suggest that the presence of lower Brønsted acid site concentrations coupled with the presence of strong Lewis acid sites

(associated with the high temperature TPD shoulder) lead to both increased propane conversion activity and propylene selectivity. This supports previous hypotheses that strong Lewis acid sites are key active sites for PDH. Although catalysts made using MPS showed clear enhancements compared to MG0, there was no significant difference between MG11 and MG16 in propane conversion rate calculated based on the total number of acid sites (**Fig. 5-15b),** suggesting that the number of strong Lewis acid sites may reach its maximum level between MPS/Ga=1.1 and MPS/Ga=1.6 compositions. There was almost no activity detected for both the pure-silica MFI and Ga impregnated pure-silica MFI (GS) catalysts. This was expected, since they did not show significant acidity during the NH_3-TPD measurements.

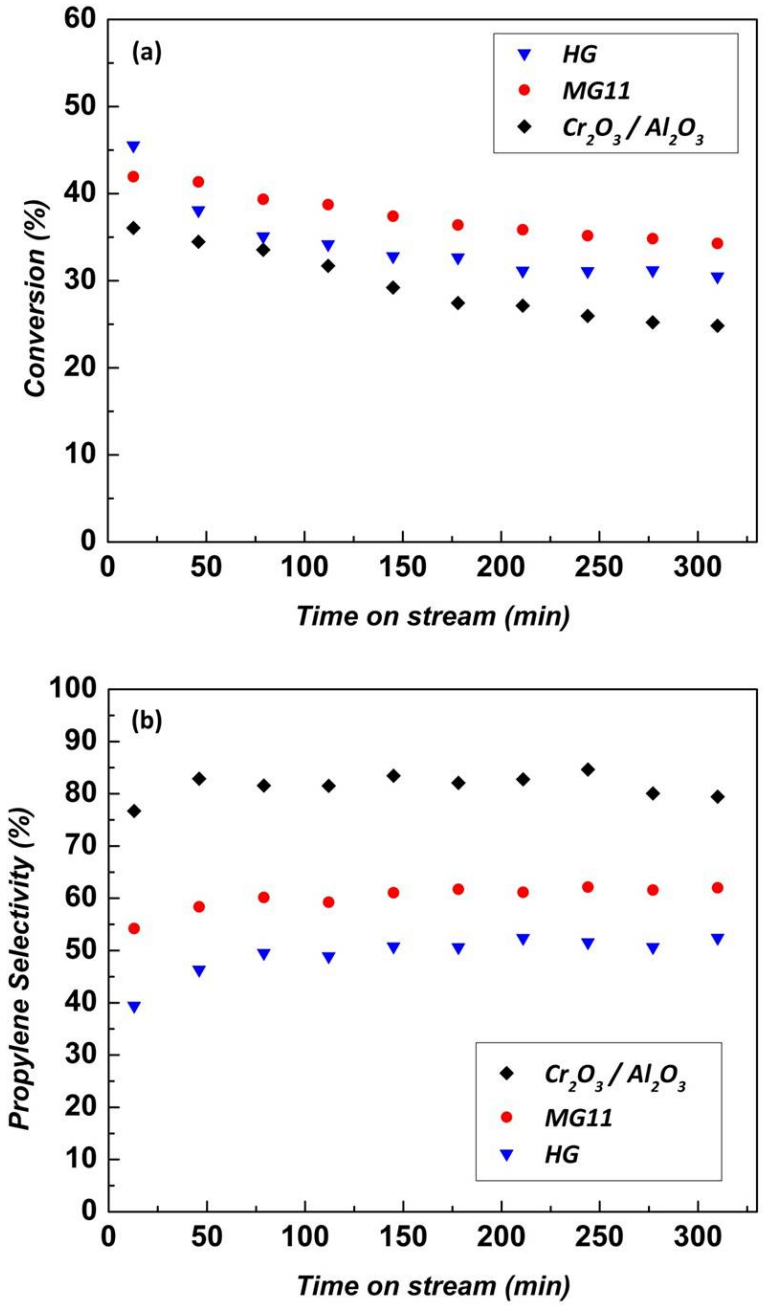

Fig. 5-13. (a) Propane conversion and (b) propylene selectivity of MG samples at 873 K and atmospheric pressure. (W/F = 0.066 g.s.cm^{-3} (MG16), 0.09 g.s.cm^{-3} (MG11), 0.12 g.s.cm^{-3} (MG05), 0.3 g.s.cm^{-3} (MG0), C_3H_8 5%)

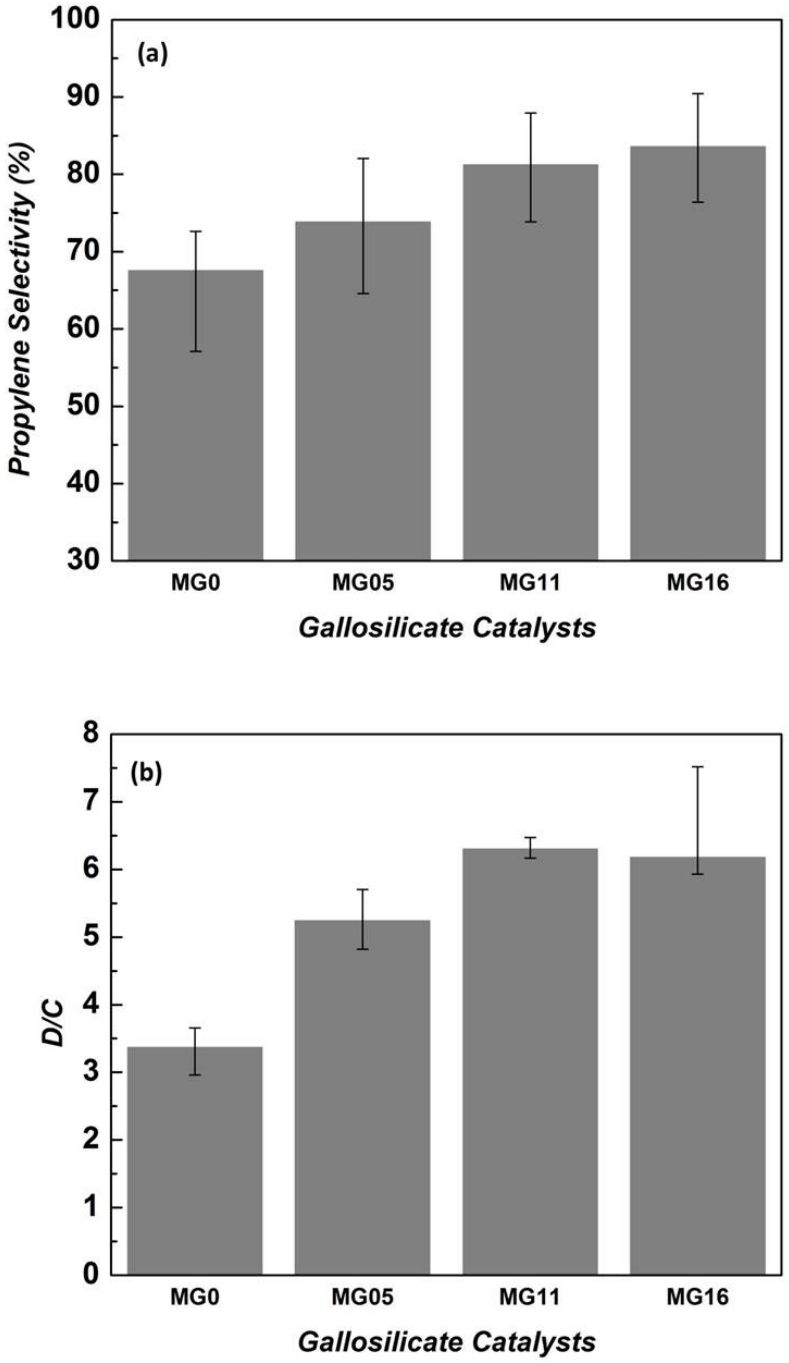

Fig. 5-14. (a) Propane selectivity and (b) ratio of dehydrogenation to cracking of MG samples at 873 K and atmospheric pressure.

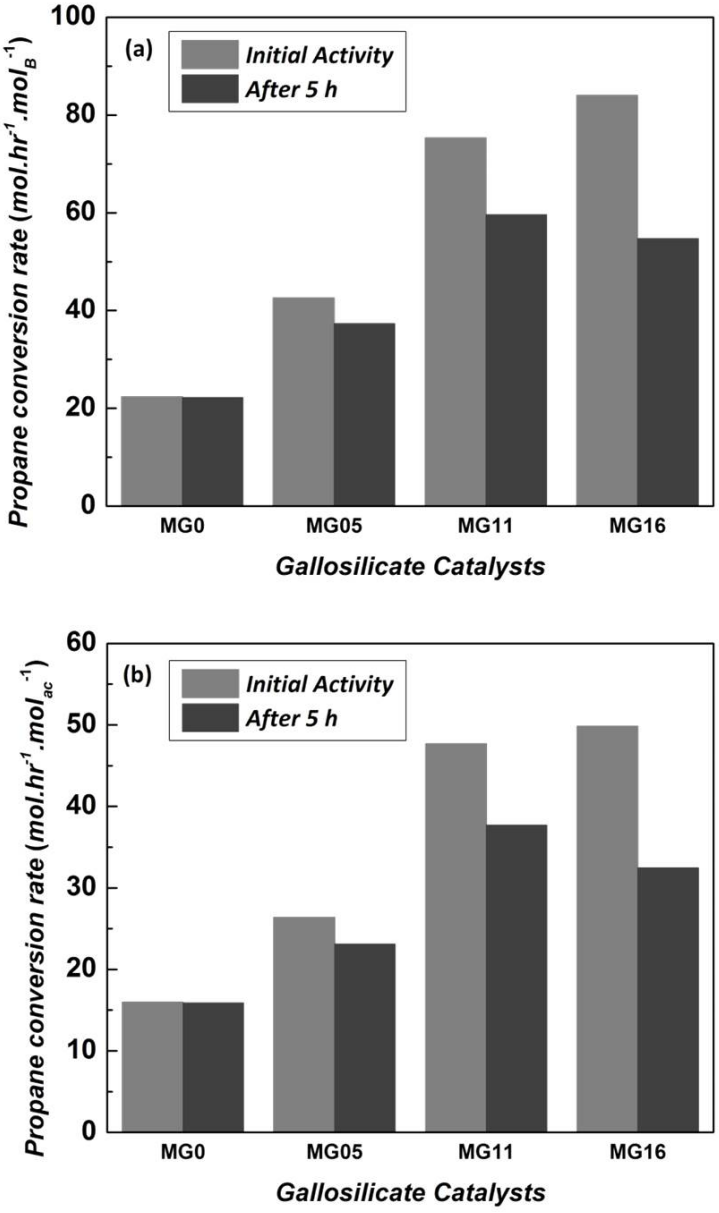

Fig. 5-15. Comparison of propane conversion rate and stability of the different MG catalysts. The propane conversion rate is calculated based on (a) the concentration of Brønsted acid sites (mol_B), (b) the concentration of total acid sites (mol_{ac}) from NH_3-TPD.

The optimal gallosilicate MFI made with MPS addition (MG11) was also compared with ion-exchanged H-gallosilicate MFI (HG) and a prototypical chromia-alumina catalyst. The catalytic measurements were done at 873 K and atmospheric pressure for 5.5 h at a higher conversion level (~40 %). Lower propylene selectivities are expected in this conversion range for the conventional Ga catalysts, based on literature reports [156]. In **Fig. 5-16**, however, it is clear that MG11 retained high propylene selectivity even in this elevated conversion range. While both Ga containing catalysts gave lower propylene selectivities than the Cr catalyst, the MG11 catalyst had a significantly higher propylene selectivity (ca. 60%) than the conventional catalyst (ca. 50%). This may be due to the lower concentration of Brønsted acid sites in MG11 compared to HG, since it is believed that Brønsted acid sites are active in the oligomerization and cyclization steps in alkane aromatization [137]. The dehydrogenation to cracking and aromatics ratios (D/C, D/A) of MG11 and HG are compared in **Fig. 5-17,** where it is clear that more dehydrogenation reactions took place over the MG11 catalysts. The HG sample, with its higher concentration of Brønsted acid sites, leads to more aromatics formation as well as cracking reactions compared to MG11, and thus showed less propylene selectivity. Furthermore, the HG catalyst deactivated faster than MG11 from similar initial conversions. This suggests that the Brønsted acidity was more affected than the Lewis acidity by carbon deposition, consistent with previous reports [133]. During the deactivation of MG11 and HG, an increase in propylene selectivity was observed, while the aromatic selectivities decreased, consistent with observations in the literature [139, 143]. However, HG showed a more significant decrease in aromatic selectivity during deactivation, as shown in **Fig. 5-18,** which also implies more

deactivation of Brønsted acid sites and subsequent reduction of aromatization efficiency. Among the three catalysts, the chromia-alumina catalyst provided the highest propylene selectivity but this catalyst also showed more deactivation than MG11, even with a slightly lower initial conversion. This indicates that the MPS-gallosilicate MFI catalyst offers better resistance to coke formation than this benchmark Cr_2O_3 catalyst under the conditions studied. Hence, for long exposure catalytic tests, MG11 provides less deactivation and better propylene yield can potentially be achieved.

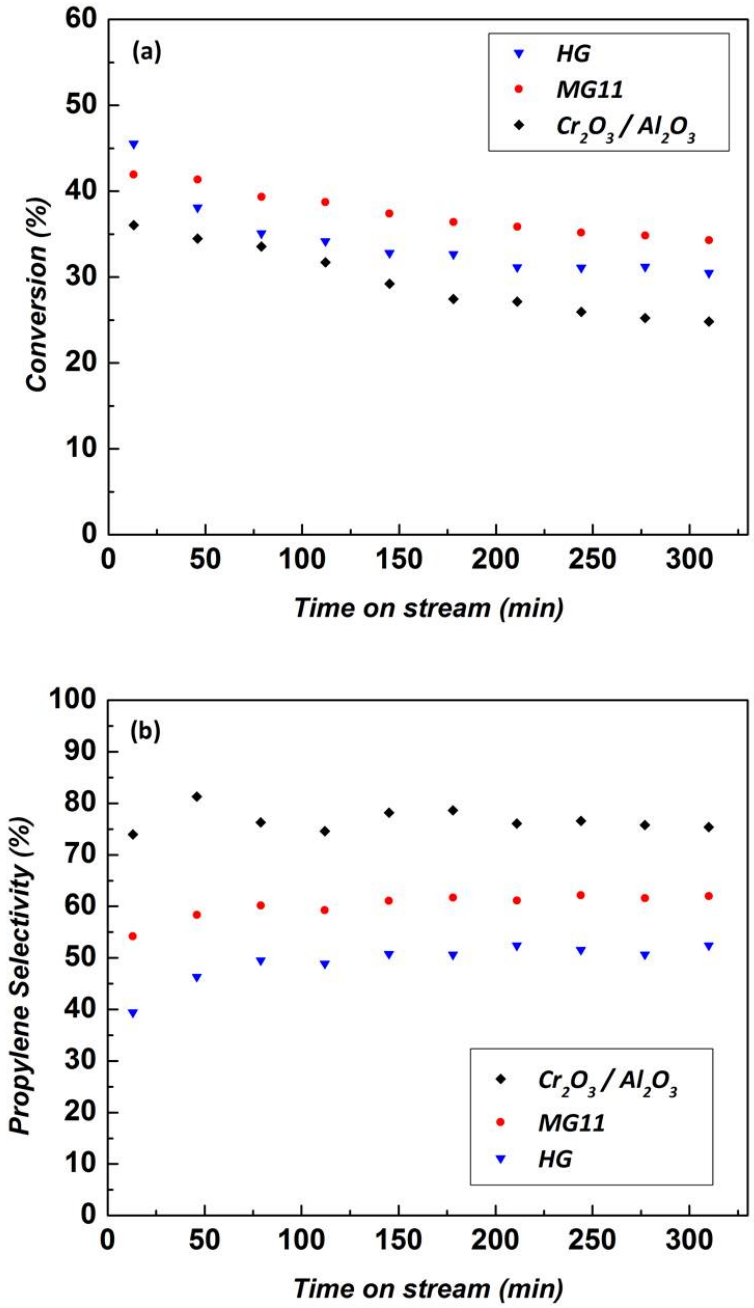

Fig. 5-16. (a) Propane conversion (b) propylene selectivity vs. time on stream of MG11, HG and chromia-alumina catalysts. (W/F = 0.6 g.s.cm^{-3} (MG11 and Cr_2O_3), 0.12 g.s.cm^{-3} (HG), C_3H_8 5%)

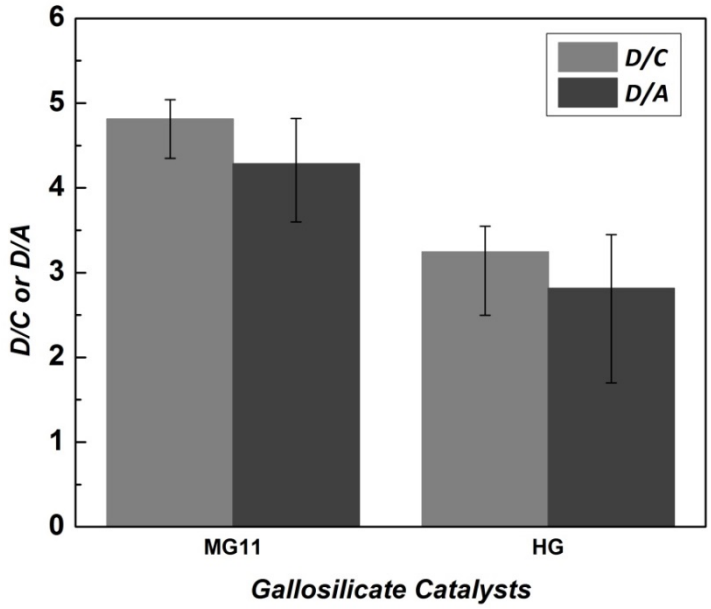

Fig. 5-17. Comparison of D/C and D/A ratio between MG11 and HG.

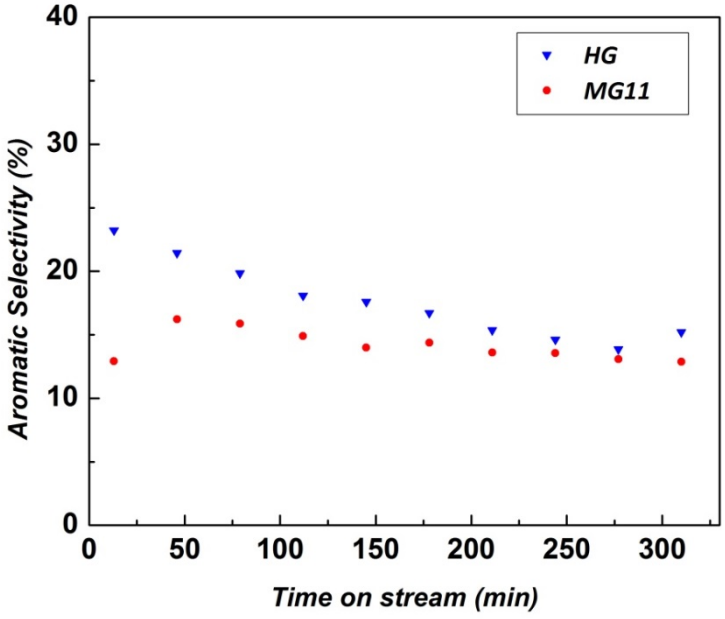

Fig. 5-18. Aromatic selectivity of MG11 and HG catalysts.

5.4. Conclusions

Gallosilicate MFI zeolite catalysts having perturbed acidities were prepared *via* the addition of MPS to the zeolite synthesis gel. These catalysts are shown to have fewer Brønsted acid sites than conventional Ga-MFI catalysts, and a greater number of Lewis acid sites. The perturbed acidities of the gallosilicate catalysts were analyzed and confirmed by NH_3-TPD, IPA-TPD and pyridine IR. The concentration of strong Lewis acid sites was increased by more MPS addition without post-synthesis impregnation or high temperature heat treatments, and therefore correlates with the amount of MPS addition to the molecular sieve synthesis.

The PDH selectivity of gallosilicate molecular sieves is known to be strongly affected by the concentration of strong Lewis acid sites, with the most effective catalysts having a small concentration of Brønsted acid sites coupled with strong Lewis acidity. Decreasing the B/L ratio leads to better performance in PDH with higher activity and propylene selectivity. Therefore, the new gallosilicates prepared by MPS addition have acidities that are well-aligned with selective PDH catalysis. The reactivity of the catalysts prepared in the presence of MPS demonstrates that these catalysts are more effective for PDH than gallosilicate catalysts prepared via conventional methods, having good propane conversion rates and higher selectivity to propylene. The concentration of strong Lewis acid sites correlates with the amount of MPS added to the molecular sieve synthesis, and the new family of catalysts prepared here have reduced cracking and aromatization selectivity. Compared with a benchmark chromia-alumina catalyst, a gallosilicate MFI catalyst prepared using MPS showed lower rate of deactivation than the benchmark catalyst, though it had slightly reduced propylene selectivity. Overall this work

demonstrates that use of functional silane during the crystallization of zeolite synthesis leads to tuning the reactivity and therefore enhanced PDH performance can be achieved.

CHAPTER 6: CONCLUSIONS AND FUTURE WORK

6.1. Main findings and conclusions

In this thesis, I have conducted detailed studies of propane dehydrogenation in membrane reactors. The work has spanned from experimental and modeling studies of membrane reactors, to a modeling study of the overall membrane reactor system, to the development of novel PDH catalysts having good propane conversion and propylene selectivity, as well as high stability with low coke formation. Overall, this work significantly advances the conceptual and practical aspects of membrane reactor processes in propylene production by dehydrogenation.

As a first objective of this thesis, experimental and modeling studies on PBMRs using tubular MFI and SAPO-34 zeolite membranes were carried out for high-temperature PDH reaction using a benchmark commercial Cr_2O_3 catalyst. The PBMR model was based on a 1D PBR model plus incorporation of membrane permeation. The PDH catalytic measurements were performed in a fixed bed reactor to obtain kinetic parameters for the Cr_2O_3 catalyst. Several kinetic models were suggested based on a rate determining step of PDH reaction mechanism on the catalytic surface, e.g., adsorption of a propane molecule or dissociation of the propane molecule through a surface reaction step. Our parameter fitting studies on experimental data suggested that the adsorption of propane molecule on the catalytic surface would be the rate determining step. In addition to the kinetic parameters obtained from the catalytic measurements, thermal cracking

parameters were also updated and used in the model to predict their contributions during PBMR operations. The modeling studies showed that the thermal cracking contribution is negligibly small (1~2 %) for a typical PBMR experiment due to competitive kinetics between the catalytic reactions and thermal cracking. I also carried out studies comparing the PBMR performance using both experiments and modeling. Although the 1D isothermal PBMR model does not consider temperature variation and mass transfer resistance on the membrane boundary, the modeling predictions and experimental results showed good agreement. Therefore the 1D PBMR model can be widely used for demonstration of PBMR performance to investigate the interplay between various operating conditions and different membrane properties.

I also carried out dimensionless analysis of our model predictions using Damköhler (*Da*) and Péclet (*Pe*) numbers to investigate the influence of reaction and transport parameters such as reaction rate, space velocity and membrane permeance on PBMR performance, and thereby determined the desired 'operating windows' for these PBMRs. An increased *Da* and a decreased *Pe* are found to be generally helpful for conversion enhancement in the PBMR. However, these effects were found to be much more beneficial in the case of highly H_2-selective (small-pore zeolite) membranes in comparison to higher-flux, lower-selectivity (medium-pore zeolite or mesoporous ceramic) membranes. H_2-selective membranes showed a plateau region of conversion at low *Pe* and high *Da*. This limit can be overcome by using a larger sweep flow rate or countercurrent operation. However, the countercurrent mode showed a complex trade-off between the reaction kinetics and forward/back-permeation across the membrane and can

be recommended only in a limited operating window. While low-selectivity, high-flux membranes can provide moderate enhancement of PBMR performance at low weight-hourly space velocity (WHSV< 1 hr^{-1}), small-pore zeolite membranes showed better performance over a wide range of operating conditions. The use of small-pore H_2-selective zeolitc membranes will greatly benefit from the fabrication of thin (~1 μm or thinner) membranes to achieve adequate transport flux for significantly higher conversion.

I then investigated a two-dimensional (2D) non-isothermal model of packed bed membrane reactor (PBMR) for the propane dehydrogenation (PDH) process. The effect of radial dispersion and membrane properties were examined using two types of Péclet (*Pe*) numbers in the PBMR system. The study revealed that large *Pe* numbers led to less enhancement of the PBMR due to dominant convective transport relative to membrane permeation. I also conducted a 2D non-isothermal PBMR model while applying multiple membrane tubes and inter-stage heaters. Use of ceramic hollow fibers are highly recommended for the membrane support material, which requires less volume of PBMR compared to using conventional scale of ceramic supported membranes. Process simulation of a PDH plant is carried out using the PBMR model, which also included the downstream separation process. The PBMR is compared with conventional packed bed reactor (PBR) for the design of a PDH plant. I focused on the effect of different PDH performance between the PBMR and PBR on the energy duties of downstream separation process in both non-recycled and recycled systems at different sweep/feed ratios. This study also demonstrated that a simple recycled system was better than a recycled system with product separation at each reactor stage. The enhancement of PDH performance

using the PBMR helps to decrease the energy load in the C_3 splitter. However, reheating and separation of the sweep gas also require higher energy duties. Therefore there exists an optimal sweep/feed ratio of the PBMR for minimal energy use.

In the area of new catalytic materials for PDH, I investigated the synthesis of gallosilicate MFI catalysts via the addition of MPS during the zeolite synthesis, with the MPS removed after synthesis by calcination. The resulting gallosilicate MFI materials had reduced concentrations of Brønsted acid sites and more Lewis acid sites, with significant concentrations of strong Lewis acid sites, as confirmed by NH_3-TPD, IPA-TPD and pyridine IR. These strong Lewis acid sites were achieved without post-synthesis impregnation of extraframework Ga or high temperature heat treatments. The concentration of strong Lewis acid sites can be controlled by adjusting the amount of MPS added, with more MPS generating more strong Lewis acid sites. The strong Lewis acidity is known to strongly affect the PDH selectivity of gallosilicate catalysts. The enhanced performance in PDH with higher activity and propylene selectivity was achieved by decreasing B/L ratio in catalytic measurements. Hence the new family of gallosilicates prepared in the presence of MPS provides well-aligned acidities and are more effective for selective PDH catalysis than gallosilicate catalysts prepared via conventional methods, having reduced cracking and aromatization selectivity. Also a new gallosilicate MFI catalyst showed lower deactivation than a benchmark chromia-alumina catalyst, although slightly reduced propylene selectivity was observed. This work demonstrates that creation of zeolite based catalysts with good PDH performance may be achieved by tuning the reactivity via use of functional silane additives added during the

crystallization of the molecular sieve.

6.2. Future research directions

Much progress has been made through this thesis work. The study can be applied to a wide range of process and material design problems, and hence I expect this work to open up more opportunities for investigation of the advanced membrane reactor system and the design of new catalysts. Here I suggest several objectives for the future research directions.

The PBMR concept in other dehydrogenation reactions: It should be possible to integrate the H_2 selective zeolite membranes into other thermodynamic limited reactions. Future research direction should therefore include investigating membrane reactors for other olefin production routes such as ethane and butane dehydrogenation. The findings and methodology in PDH PBMR studies would be useful to develop both process and material design strategies for those reaction systems.

Finding enhanced PDH process configuration along with techno-economic analysis: I have demonstrated that use of a PBMR for PDH application is beneficial in term of both propylene production and improved energy efficiency. For the whole PDH plant design, this work notably represents the first attempt to establish combining PBMRs and downstream separation. The results are encouraging and should be validated in an

optimized heat integrated system with detailed techno-economic analysis, considering the heating and cooling costs from different energy sources. This analysis can also be explored with downstream membrane separation. The current distillation column used as the C_3 splitter is still energy intensive and therefore can be integrated with additional membrane separations for addressing the propane/propylene mixture. This future modeling study would provide insight into the research areas of membranes and membrane reactors and lead to progress for robust and cost-effective chemical processes.

Finding new candidates for PDH zeolite catalysis: It is evident that using a functional silane group for the preparation of Ga containing zeolite catalysts provides an enhanced bi-functional catalyst for better PDH performance. An important question for future studies is to determine the relation between acid site distribution and zeolite structure, which also remains to be validated for other types of zeolites. Hierarchical zeolites can be one of the strong candidates for PDH catalysts since they may provide fast-exit of propylene through the mesopore structure, thereby suppressing side products and coke formation. It would be interesting to know if controlling the acid site distribution by the functional silane appears to be effective for hierarchical zeolites as well, e.g. hierarchical gallosilicates. Also, the scope of tuning of the zeolites can be expanded to other possible framework hetero-atoms such as Fe or In. This approach would provide many opportunities for the design of zeolite catalysts in terms of both enhanced activity and propylene selectivity.

APPENDIX

Derivation of dimensionless governing equations in Chapter 3

The 1D dimensionless governing equations in Chapter 3 can be derived from the 1D model in Chapter 2 as follows:

$$\frac{dF_t}{dz} = rg_{cat}' - Q\cdot\left(P_t - P_s\right)2\pi R_1 \qquad \text{(Tube)} \qquad (2\text{-}1)$$

$$\frac{dF_s}{dz} = Q\cdot\left(P_t - P_s\right)2\pi R_1 \qquad \text{(Shell)} \qquad (2\text{-}2)$$

For the tube side,

$$\frac{dF_t}{dz} = rg_{cat}' - J\cdot 2\pi R_1 \qquad \text{(Tube)}$$

$$\frac{dF_t}{dz} = rg_{cat}' - Q\cdot\left(P_T y_t - P_S y_s\right)\cdot 2\pi R_1$$

$$\frac{P_T}{R_g T}\pi R_1^{\,2}\ \frac{d\left(v_t y_t\right)}{dz} = rg_{cat}' - Q\cdot P_T\left(y_t - \frac{P_S}{P_T}y_s\right)2\pi R_1$$

$$\frac{P_T}{R_g T}\pi R_1^{\,2}\ \frac{v_{t0}}{L}\frac{d\left(\tilde{v}_t y_t\right)}{d\tilde{z}} = k_1 P_T\frac{g_{cat}}{L}\left(\frac{y_A - 1/K\left(y_B y_C\right)P_T}{\left(1+K_{a2}P_B+\left(K_{a3}P_C\right)^{0.5}\right)^2}\right) - Q\cdot P_T\,2\pi R_1\ \left(y_t - R_p y_s\right)$$

$$\frac{d\left(\tilde{v}_t y_t\right)}{d\tilde{z}} = \frac{k_1 R_g T}{v_{t0}\pi R_1^{\,2}}g_{cat}\left(\frac{y_A - 1/K\left(y_B y_C\right)P_T}{\left(1+K_{a2}P_B+\left(K_{a3}P_C\right)^{0.5}\right)^2}\right) - \frac{Q_{H_2}\cdot R_g T}{v_{t0}}\frac{2L}{R_1}\alpha\ \left(y_t - R_p y_s\right)$$

$$\frac{d\left(\tilde{v}_t y_t\right)}{d\tilde{z}} = \frac{k_1 R_g T}{v_{t0}\pi R_1^{\,2}}\left(1-\varepsilon\right)\pi R_1^{\,2} L\rho_{cat}\left(\frac{y_A - 1/K\left(y_B y_C\right)P_T}{\left(1+K_{a2}P_B+\left(K_{a3}P_C\right)^{0.5}\right)^2}\right) - \frac{Q_{H_2}\cdot R_g T}{v_{t0}}\frac{2L}{R_1}\alpha\ \left(y_t - R_p y_s\right)$$

$$\frac{d\left(\tilde{v}_t y_t\right)}{d\tilde{z}} = \frac{k_1 R_g T\left(1-\varepsilon\right)L\rho_{cat}}{v_{t0}}\left(\frac{y_A - 1/K\left(y_B y_C\right)P_T}{\left(1+K_{a2}P_B+\left(K_{a3}P_C\right)^{0.5}\right)^2}\right) - \frac{Q_{H_2}\cdot R_g T}{v_{t0}}\frac{2L}{R_1}\alpha\ \left(y_t - R_p y_s\right)$$

$$\frac{d\left(\tilde{v}_t y_t\right)}{d\tilde{z}} = Da\left(\frac{y_A - 1/K\left(y_B y_C\right)P_T}{\left(1+K_{a2}P_B+\left(K_{a3}P_C\right)^{0.5}\right)^2}\right) - \frac{1}{Pe}\alpha\ \left(y_t - R_p y_s\right)$$

For the shell side,

$$\frac{dF_s}{dz} = Q\cdot\left(P_T y_t - P_S y_s\right)\cdot 2\pi R_1 \qquad \text{(Shell)}$$

$$\frac{P_S}{R_g T}\pi\left(R_2 - R_1\right)^2 \frac{d\left(v_s y_s\right)}{dz} = Q\cdot P_T\left(y_t - R_p y_s\right)2\pi R_1$$

$$\frac{P_S}{R_g T}\pi\left(R_2 - R_1\right)^2 \frac{v_{s0}}{L}\frac{d\left(\tilde{v}_s y_s\right)}{d\tilde{z}} = Q\cdot P_T\left(y_t - R_p y_s\right)2\pi R_1$$

$$\frac{P_S}{R_g T}\pi\left(R_2 - R_1\right)^2 \frac{v_{t0}}{L}\frac{R_s}{R_p}\frac{R_1^{\,2}}{\left(R_2 - R_1\right)^2}\frac{d\left(\tilde{v}_s y_s\right)}{d\tilde{z}} = Q\cdot P_T\left(y_t - R_p y_s\right)2\pi R_1$$

$$\left(\begin{array}{l} R_s = \dfrac{\dfrac{P_S}{R_g T}\pi\left(R_2 - R_1\right)^2 v_{s0}}{\dfrac{P_T}{R_g T}\pi R_1^{\,2} v_{t0}} = \dfrac{P_S\left(R_2 - R_1\right)^2 v_{s0}}{P_T R_1^{\,2} v_{t0}} = \dfrac{\left(R_2 - R_1\right)^2 v_{s0}}{R_1^{\,2} v_{t0}} R_p \\ \\ \dfrac{R_s}{R_p}\dfrac{R_1^{\,2}}{\left(R_2 - R_1\right)^2} v_{t0} = v_{s0} \end{array}\right)$$

$$\frac{P_T}{R_g T}\pi R_1^{\,2}\frac{v_{t0}}{L}R_s\frac{d\left(\tilde{v}_s y_s\right)}{d\tilde{z}} = Q\cdot P_T\left(y_t - R_p y_s\right)2\pi R_1$$

$$\frac{d\left(\tilde{v}_s y_s\right)}{d\tilde{z}} = \frac{Q_{H_2}\cdot R_g T}{v_{t0}}\frac{2L}{R_1}\frac{\alpha}{R_s}\left(y_t - R_p y_s\right)$$

$$\frac{d\left(\tilde{v}_s y_s\right)}{d\tilde{z}} = \frac{1}{Pe}\frac{\alpha}{R_s}\left(y_t - R_p y_s\right)$$

Finite difference formulas in Chapter 4

The finite difference formulas for 2D governing equations in Chapter 4 are as follows (catalysts in shell side). Each side of the tube, membrane support and shell side are divided by n. The *j* is 1 ~ n+1 node at each side:

Mass transfer

For the tube side,

$j = 1,$

$$\frac{\partial\left(u_T C_i\right)}{\partial z} = D_t\left\{\frac{1}{r_t}\frac{\partial}{\partial r_t}\left(r_t\frac{\partial C_i}{\partial r_t}\right)\right\}$$

$$\frac{P_{total}^{\ R}}{R_g T}\frac{\partial u_T y_a}{\partial z} = \frac{P_{total}^{\ R}}{R_g T}D_r\left\{\frac{1}{r_t}\frac{\partial y_a}{\partial r_t} + \frac{\partial^2 y_a}{\partial r_t^2}\right\}$$

$$\frac{P_{total}^{\ R}}{R_g T}\frac{u_T y_a^{\ i,1} - u_T y_a^{\ i-1,1}}{\Delta l} - \frac{P_{total}^{\ R}}{R_g T}\frac{D_r}{u_t \Delta r_t}\frac{y_a^{\ i,3} - y_a^{\ i,1}}{2\Delta r_t} = 0$$

$$\left\{\frac{P_{total}^{\ R}}{R_g T}\left(\frac{1}{\Delta l} + \frac{D_r}{u_t 2\Delta r_t^2}\right)\right\}u_t y_a^{\ i,1} + \left(-\frac{P_{total}^{\ R}}{R_g T}\frac{D_r}{2u_t\Delta r_t^2}\right)u_t y_a^{\ i,3} = \left(\frac{P_{total}^{\ R}}{R_g T}\frac{1}{\Delta l}\right)y_a^{\ i-1,1}$$

$$\{AMO\}\, y_a^{\ i,1} + (BMO)\, y_a^{\ i,3} = (CMO)\, y_a^{\ i-1,1}$$

$j = 2\sim n,$

$$\frac{P_{total}^{\ R}}{R_g T}\frac{\partial u_T y_a}{\partial z} = \frac{P_{total}^{\ R}}{R_g T}D_r\left\{\frac{1}{r_t}\frac{\partial y_a}{\partial r_t} + \frac{\partial^2 y_a}{\partial r_t^2}\right\}$$

$$\frac{P_{total}^{\ R}}{R_g T}\frac{u_T y_a^{\ i,j} - u_T y_a^{\ i-1,j}}{\Delta l} = \frac{P_{total}^{\ R}}{R_g T}\frac{D_r}{u_T}\left\{\frac{1}{r_t}\frac{u_T y_a^{\ i,j+1} - u_T y_a^{\ i,j-1}}{2\Delta r_t} + \frac{u_T y_a^{\ i,j+1} - 2u_T y_a^{\ i,j} + u_T y_a^{\ i,j-1}}{\Delta r_t^2}\right\}$$

$$\left\{\frac{P_{total}^{\ R}}{R_g T}\frac{D_r}{u_T}\left(\frac{1}{r_t 2\Delta r_t} - \frac{1}{\Delta r_t^2}\right)\right\}u_T y_a^{\ i,j-1} + \left\{\frac{P_{total}^{\ R}}{R_g T}\left(\frac{1}{\Delta l} + \frac{2D_r}{u_T\Delta r_t^2}\right)\right\}u_T y_a^{\ i,j}$$

$$+ \left\{-\frac{P_{total}^{\ R}}{R_g T}\frac{D_r}{u_T}\left(\frac{1}{r_t 2\Delta r_t} + \frac{1}{\Delta r_t^2}\right)\right\}u_T y_a^{\ i,j+1} = \frac{P_{total}^{\ R}}{R_g T}\frac{1}{\Delta l}u_T y_a^{\ i-1,j}$$

$$\{ATM\}\, y_a^{\ i,j-1} + \{BTM\}\, y_a^{\ i,j} + \{CTM\}\, y_a^{\ i,j+1} = (DTM)\, y_a^{\ i-1,j}$$

$j = n+1,$

$$\frac{P_{total}{}^{R}}{R_g T}\frac{\partial u_T y_a}{\partial z} = \frac{P_{total}{}^{R}}{R_g T}\frac{D_r}{u_T}\left\{\frac{1}{r_t}\frac{\partial u_T y_a}{\partial r_t} + \frac{\partial^2 u_T y_a}{\partial r_t^2}\right\}$$

$$\left\{-\frac{P_{total}{}^{R}}{R_g T}\frac{D_r}{2u_T \Delta r_t^2}\right\}u_T y_a{}^{i,n-1} + \left\{\frac{1}{u_T R_1}q_a + \frac{1}{u_T \Delta r_t}q_a + \frac{P_{total}{}^{R}}{R_g T}\left(\frac{1}{\Delta l} + \frac{D_r}{2u_T \Delta r_t^2}\right)\right\}u_T y_a{}^{i,n+1}$$

$$+ \left\{-\frac{1}{R_1}q_a - \frac{1}{\Delta r_t}q_a\right\}y_a{}^{i,m1} = \frac{P_{total}{}^{R}}{R_g T}\frac{1}{\Delta l}u_T y_a{}^{i-1,j}$$

$$\{ANM\}\, y_a{}^{i,n-1} + \{BNM\}\, y_a{}^{i,n+1} + \{CNM\}\, y_a{}^{i,m1} = (DNM)\, y_a{}^{i-1,j}$$

For the membrane side,

$j = 1$

$$\frac{1}{r_m}\frac{\partial}{\partial r_m}\left(r_m \frac{\partial y_a}{\partial r_m}\right) = \left\{\frac{1}{r_m}\frac{\partial y_a}{\partial r_m}\bigg|_{R1} + \frac{\partial}{\partial r_m}\left(\frac{\partial y_a}{\partial r_m}\bigg|_{2} - \frac{\partial y_a}{\partial r_m}\bigg|_{R1}\right)\right\} = 0$$

$$-\frac{1}{R_1}q_a\left(u_t y_a{}^{t,n+1}/u_t - y_a{}^{m,1}\right) + \frac{P_{total}{}^{p}}{R_g T}D_m \frac{y_a{}^{i,3} - y_a{}^{i,1}}{2\Delta r_m{}^2} + \frac{1}{\Delta r_m}q_a\left(u_t y_a{}^{t,n+1}/u_t - y_a{}^{m,1}\right) = 0$$

$$\left\{q_a\left(-\frac{1}{u_t R_1} + \frac{1}{u_t \Delta r_m}\right)\right\}u_t y_a{}^{t,n+1} + \left\{-\frac{P_{total}{}^{p}}{R_g T}\frac{D_m}{2\Delta r_m{}^2} - q_a\left(-\frac{1}{R_1} + \frac{1}{\Delta r_m}\right)\right\}y_a{}^{m,1}$$

$$+ \left(\frac{P_{total}{}^{p}}{R_g T}\frac{D_m}{2\Delta r_m{}^2}\right)y_a{}^{i,3} = 0$$

$$\{ABM1\}\, y_a{}^{t,n+1} + \{BBM1\}\, y_a{}^{m,1} + (CBM1)\, y_a{}^{i,3} = 0$$

$j = 2\sim n$

$$\frac{1}{r_m}\frac{\partial}{\partial r_m}\left(r_m \frac{\partial y_a}{\partial r_m}\right) = \left\{\frac{1}{r_m}\frac{\partial y_a}{\partial r_m}\bigg|_{j} + \frac{\partial^2 y_a}{\partial r_m{}^2}\right\} = 0$$

$$\left(\frac{-1}{r_m 2\Delta r_m} + \frac{1}{\Delta r_m{}^2}\right)y_a{}^{i,j-1} + \frac{-2}{\Delta r_m{}^2}y_a{}^{i,j} + \left(\frac{1}{r_m 2\Delta r_m} + \frac{1}{\Delta r_m{}^2}\right)y_a{}^{i,j+1} = 0$$

$$(AMM)\, y_a{}^{i,j-1} + (BMM)\, y_a{}^{i,j} + (CMM)\, y_a{}^{i,j+1} = 0$$

$$j = n+1$$

$$\frac{1}{r_m}\frac{\partial}{\partial r_m}\left(r_m \frac{\partial y_a}{\partial r_m}\right) = \left\{\frac{1}{r_m}\frac{\partial y_a}{\partial r_m}\bigg|_{R2} + \frac{\partial}{\partial r_m}\left(\frac{\partial y_a}{\partial r_m}\bigg|_{R2} - \frac{\partial y_a}{\partial r_m}\bigg|_{n}\right)\right\} = 0$$

$$\frac{1}{R_2}\frac{\partial y_a}{\partial r_m}\bigg|_{R2} + \left\{\frac{\partial}{\partial r_m}\left(\frac{\partial y_a}{\partial r_m}\bigg|_{R2} - \frac{\partial y_a}{\partial r_m}\bigg|_{n}\right)\right\} = 0$$

$$\left\{\frac{P_{total}{}^{p}}{R_g T}\frac{D_m}{2\Delta r_m{}^2}\right\} y_a{}^{i,n-1} + \left\{-q_a\left(\frac{1}{R_2} + \frac{1}{\Delta r_m}\right) - \frac{P_{total}{}^{p}}{R_g T}\frac{D_m}{2\Delta r_m{}^2}\right\} y_a{}^{m,n+1} + \left(q_a\left(\frac{1}{u_s R_2} + \frac{1}{u_s \Delta r_m}\right)\right) u_s y_a{}^{s,1} = 0$$

$$\{ABM2\}\, y_a{}^{t,n-1} + \{BBM2\}\, y_a{}^{m,n+1} + (CBM2)\, y_a{}^{s,1} = 0$$

For the shell side,

$$j = 1$$

$$\frac{P_{total}{}^{P}}{R_g T_s}\frac{\partial u_s y_a}{\partial z} = \frac{P_{total}{}^{P}}{R_g T_s} D_r \left\{\frac{1}{r_s}\frac{\partial}{\partial r_s}\left(r_s \frac{\partial y_a}{\partial r_s}\right)\right\} + \rho_B(-rA)$$

$$\frac{P_{total}{}^{P}}{R_g T_s}\frac{u_s y_a{}^{i,1} - u_s y_a{}^{i-1,1}}{\Delta l} = \frac{P_{total}{}^{P}}{R_g T_s}\frac{D_r}{u_s}\left\{\frac{1}{r_s}\frac{\partial y_a}{\partial r_s}\bigg|_{R2} + \frac{\partial^2 y_a}{\partial r_s{}^2}\right\} + \rho_B(-rA)$$

$$\left\{-q_a\left(-\frac{1}{R_2} + \frac{1}{\Delta r_s}\right)\right\} y_a{}^{m,n+1} + \left\{\frac{P_{total}{}^{P}}{R_g T_s}\left(\frac{1}{\Delta l} + \frac{D_r}{2u_s \Delta r_s{}^2}\right) + q_a\left(-\frac{1}{u_s R_2} + \frac{1}{u_s \Delta r_s}\right)\right\} u_s y_a{}^{i,1} + \left(-\frac{P_{total}{}^{P}}{R_g T_s}\frac{D_r}{2\Delta r_s{}^2}\right) y_a{}^{i,3} = \left(\frac{P_{total}{}^{P}}{R_g T_s}\frac{1}{\Delta l}\right) u_s y_a{}^{i-1,1} + \rho_B(-rA)$$

$$\{ASMB1\}\, y_a{}^{m,n+1} + \{BSBM1\}\, y_a{}^{i,1} + (CSBM1)\, y_a{}^{i,3} = (DSBM1)\, y_a{}^{i-1,1} + RXN$$

$j = 2 \sim n$

$$\frac{P_{total}{}^{P}}{R_g T_s}\frac{\partial u_s y_a}{\partial z} = \frac{P_{total}{}^{P}}{R_g T_s} D_r \left\{ \frac{1}{r_s}\frac{\partial}{\partial r_s}\left(r_s \frac{\partial y_a}{\partial r_s} \right) \right\} + \rho_B (-rA)$$

$$\left\{ \frac{P_{total}{}^{P}}{R_g T_s}\frac{D_r}{u_s}\left(\frac{1}{2r_s \Delta r_s} - \frac{1}{\Delta r_s{}^2} \right) \right\} u_s y_a{}^{i,j-1} + \left\{ \frac{P_{total}{}^{P}}{R_g T_s}\left(\frac{1}{\Delta l} + \frac{2D_r}{u_s \Delta r_s{}^2} \right) \right\} u_s y_a{}^{i,j}$$

$$+ \left\{ -\frac{P_{total}{}^{P}}{R_g T_s}\frac{D_r}{u_s}\left(\frac{1}{\Delta r_s{}^2} + \frac{1}{2r_s \Delta r_s} \right) \right\} u_s y_a{}^{i,j+1} = \left(\frac{P_{total}{}^{P}}{R_g T_s}\frac{1}{\Delta l} \right) u_s y_a{}^{i-1,1} + \rho_B (-rA)$$

$$\{ASM\} y_a{}^{i,j-1} + \{BSM\} y_a{}^{i,j} + \{CSM\} y_a{}^{i,j+1} = (DSM) y_a{}^{i-1,1} + RXN$$

$j = n+1$

$$\frac{P_{total}{}^{P}}{R_g T_s}\frac{\partial u_s y_a}{\partial z} = \frac{P_{total}{}^{P}}{R_g T_s} D_r \left\{ \frac{1}{r_s}\frac{\partial}{\partial r_s}\left(r_s \frac{\partial y_a}{\partial r_s} \right) \right\} + \rho_B (-rA)$$

$$\left\{ -\frac{P_{total}{}^{P}}{R_g T_s}\frac{D_r}{2u_s \Delta r_s{}^2} \right\} y_a{}^{i,j-2} + \left\{ \frac{P_{total}{}^{P}}{R_g T_s}\left(\frac{1}{\Delta l} + \frac{D_r}{2u_s \Delta r_s{}^2} \right) \right\} y_a{}^{i,j}$$

$$= \left(\frac{P_{total}{}^{P}}{R_g T_s}\frac{1}{\Delta l} \right) y_a{}^{i-1,j} + \rho_B (-rA)$$

$$\{ASBM2\} y_a{}^{i,j-1} + \{BSBM2\} y_a{}^{i,j} = (CSBM) y_a{}^{i-1,1} + RXN$$

Heat transfer

For the tube side,

$j = 1,$

$$\rho_T C_p u_T \frac{T_T^{i,1} - T_T^{i-1,1}}{\Delta l} = k_{gas}\left\{\frac{1}{r_t}\frac{\partial T_T}{\partial r}\bigg|_{r=1} + \frac{1}{\Delta r_t}\left(\frac{\partial T_T}{\partial r}\bigg|_{j=2} - \frac{\partial T_T}{\partial r}\bigg|_{j=1}\right)\right\}$$

$$\rho_T C_p u_T \frac{T_T^{i,1} - T_T^{i-1,1}}{\Delta l} = k_{gas}\left\{\frac{1}{\Delta r_t}\frac{T_T^{i,3} - T_T^{i,1}}{2\Delta r_t}\right\}$$

$$\left(\frac{\rho_T C_p u_T}{\Delta l} + \frac{k_{gas}}{\Delta r_t 2\Delta r_t}\right)T_T^{i,1} + \left(-\frac{k_{gas}}{\Delta r_t 2\Delta r_t}\right)T_T^{i,3} = \left(\frac{\rho_T C_p u_T}{\Delta l}\right)T_T^{i-1,1}$$

$$(A0)T_T^{i,1} + (B0)T_T^{i,3} = (C0)T_T^{i-1,1}$$

$j = 2\sim n,$

$$\rho_T C_p \frac{\partial u_T T_T}{\partial z} = k_{gas}\left\{\frac{1}{r_t}\frac{\partial T_T}{\partial r_t} + \frac{\partial^2 T_T}{\partial r_t^2}\right\}$$

$$\rho_T C_p u_T \frac{T_T^{i,j} - T_T^{i-1,j}}{\Delta l} = k_{gas}\left\{\frac{1}{r_t}\frac{T_T^{i,j+1} - T_T^{i,j-1}}{2\Delta r_t} + \frac{T_T^{i,j+1} - 2T_T^{i,j} + T_T^{i,j-1}}{\Delta r_t^2}\right\}$$

$$\left(\frac{k_{gas}}{r_t 2\Delta r_t} - \frac{k_{gas}}{\Delta r_t^2}\right)T_T^{i,j-1} + \left(\frac{\rho_T C_p u_T}{\Delta l} + \frac{2k_{gas}}{\Delta r_t^2}\right)T_T^{i,j} + \left(-\frac{k_{gas}}{r_t 2\Delta r_t} - \frac{k_{gas}}{\Delta r_t^2}\right)T_T^{i,j+1} = \left(\frac{\rho_T C_p u_T}{\Delta l}\right)T_T^{i-1,j}$$

$$(AT)T_T^{i,j-1} + (BT)T_T^{i,j} + (CT)T_T^{i,j+1} = (DT)T_T^{i-1,j}$$

$j = n + 1,$

$$\rho_T C_p u_T \frac{T_T^{i,n+1} - T_T^{i-1,n+1}}{\Delta l} = k_{gas}\left\{\frac{1}{r}\frac{dT_T}{dr}\bigg|_{r=R1} + \frac{1}{\Delta r_t}\left(\frac{dT_T}{dr}\bigg|_{j=R1} - \frac{dT_T}{dr}\bigg|_{j=n}\right)\right\}$$

$$\left(\frac{\rho_T C_p u_T}{\Delta l} + \frac{h}{R1} + \frac{h}{\Delta r_t} + \frac{k_{gas}}{2\Delta r_t^2}\right)T_T^{i,n+1} + \left(\frac{-k_{gas}}{2\Delta r_t^2}\right)T_T^{i,n-1} = \frac{\rho_T C_p u_T}{\Delta l}T_T^{i-1,n+1} + \left(\frac{h}{R1} + \frac{h}{\Delta r}\right)T_m^{i,1}$$

$$(AN)T_T^{i,n+1} + (BN)T_T^{i,n-1} = (CN)T_T^{i-1,n+1} + (DN)T_m^{i,1}$$

For the membrane side,

$$j = 1$$

$$K_m \frac{1}{r}\frac{d}{dr}\left(r\frac{dT_m}{dr} \right) = \frac{K_m}{r_m}\left.\frac{\partial T_m}{\partial r}\right|_{R1} + \frac{K_m}{\Delta r_m}\left(\left.\frac{\partial T_m}{\partial r}\right|_{j=2} - \left.\frac{\partial T_m}{\partial r}\right|_{R1} \right) = 0$$

$$\left(-\frac{h}{R1} + \frac{h}{\Delta r_m} \right) T_T^{\,i,n+1} + \left(\frac{h}{R1} - \frac{K_m}{2\Delta r_m^{\,2}} - \frac{h}{\Delta r_m} \right) T_m^{\,i,1} + \left(\frac{K_m}{2\Delta r_m^{\,2}} \right) T_m^{\,i,3} = 0$$

$$(AB1)\,T_T^{\,i,n+1} + (BB1)\,T_m^{\,i,1} + (CB1)\,T_m^{\,i,3} = 0$$

$$j = 2 \sim n,$$

$$\frac{1}{r_m}\frac{T_m^{\,i,j+1} - T_m^{\,i,j-1}}{2\Delta r_m} + \frac{T_m^{\,i,j+1} - 2T_m^{\,i,j} + T_m^{\,i,j-1}}{\Delta r_m^{\,2}} = 0$$

$$\left(\frac{-1}{2r_m\Delta r_m} + \frac{1}{\Delta r_m^{\,2}} \right) T_m^{\,i,j-1} + \left(\frac{-2}{\Delta r_m^{\,2}} \right) T_m^{\,i,j} + \left(\frac{1}{2r_m\Delta r_m} + \frac{1}{\Delta r_m^{\,2}} \right) T_m^{\,i,j+1} = 0$$

$$(AM)\,T_m^{\,i,j-1} + (BM)\,T_m^{\,i,j} + (CM)\,T_m^{\,i,j+1} = 0$$

$$j = n + 1,$$

$$K_m \frac{1}{r}\frac{d}{dr}\left(r\frac{dT_m}{dr} \right) = \frac{K_m}{r_m}\left.\frac{\partial T_m}{\partial r}\right|_{R2} + \frac{K_m}{\Delta r_m}\left(\left.\frac{\partial T_m}{\partial r}\right|_{R2} - \left.\frac{\partial T_m}{\partial r}\right|_{j=n} \right) = 0$$

$$\left(\frac{K_m}{2\Delta r_m^{\,2}} \right) T_m^{\,i,n-1} + \left(-\frac{h}{R2} - \frac{K_m}{2\Delta r_m^{\,2}} - \frac{h}{\Delta r_m} \right) T_m^{\,i,n+1} + \left(\frac{h}{R2} + \frac{h}{\Delta r_m} \right) T_s^{\,i,1} = 0$$

$$(AB2)\,T_m^{\,i,n-1} + (BB2)\,T_m^{\,i,n+1} + (CB2)\,T_s^{\,i,1} = 0$$

For the shell side,

$j = 1,$

$$\rho_S C_p u_S \frac{dT_s}{dz} = k_{eff}\left\{\frac{1}{r}\frac{d}{dr}\left(r\frac{dT_s}{dr}\right)\right\} + \rho_B\left(-rA\right)\left(-\Delta H\right)$$

$$\left(\frac{h}{R2} - \frac{h}{\Delta r_s}\right)T_m^{\,i,n+1} + \left(\frac{\rho_S C_p u_S}{\Delta l} - \frac{h}{R2} + \frac{h}{\Delta r_s} + \frac{k_{eff}}{2\Delta r_s^{\,2}}\right)T_s^{\,i,1}$$

$$+ \left(\frac{-k_{eff}}{2\Delta r_s^{\,2}}\right)T_s^{\,i,3} = \frac{\rho_S C_p u_S}{\Delta l}T_s^{\,i-1,1} + \rho_B\left(-rA\right)\left(-\Delta H\right)$$

$$\left(ASB1\right)T_m^{\,i,n+1} + \left(BSB1\right)T_s^{\,i,1} + \left(CSB1\right)T_s^{\,i,3} = \left(DSB1\right)T_s^{\,i-1,1} + RXN$$

$j = 2 \sim n,$

$$\rho_S C_p u_S \frac{T_s^{\,i,j} - T_s^{\,i-1,j}}{\Delta l} = k_{eff}\left\{\frac{1}{r_s}\frac{T_s^{\,i,j+1} - T_s^{\,i,j-1}}{2\Delta r_s} + \frac{T_s^{\,i,j+1} - 2T_s^{\,i,j} + T_s^{\,i,j-1}}{\Delta r_s^{\,2}}\right\}$$

$$+ \rho_B\left(-rA\right)\left(-\Delta H\right)$$

$$\left(\frac{k_{eff}}{r_s 2\Delta r_s} - \frac{k_{eff}}{\Delta r_s^{\,2}}\right)T_s^{\,i,j-1} + \left(\frac{\rho_S C_p u_S}{\Delta l} + \frac{2k_{eff}}{\Delta r_s^{\,2}}\right)T_s^{\,i,j} + \left(-\frac{k_{eff}}{r_s 2\Delta r_s} - \frac{k_{eff}}{\Delta r_s^{\,2}}\right)T_s^{\,i,j+1}$$

$$= \left(\frac{\rho_S C_p u_S}{\Delta l}\right)T_s^{\,i-1,j} + \rho_B\left(-rA\right)\left(-\Delta H\right)$$

$$\left(AS\right)T_s^{\,i,j-1} + \left(BS\right)T_s^{\,i,j} + \left(CS\right)T_s^{\,i,j+1} = \left(DS\right)T_s^{\,i-1,j} + RXN$$

$j = n+1,$

$$\rho_S C_p u_S \frac{dT_s}{dz} = k_{eff}\left\{\frac{1}{r_s}\frac{\partial T_s}{\partial r}\bigg|_{r=R3} + \frac{1}{\Delta r_s}\left(\frac{dT_T}{dr}\bigg|_{j=R3} - \frac{dT_T}{dr}\bigg|_{j=n}\right)\right\}$$

$$+ \rho_B\left(-rA\right)\left(-\Delta H\right)$$

$$\left(\frac{k_{eff}}{2\Delta r_s^{\,2}}\right)T_s^{\,i,n-1} + \left(\frac{\rho_S C_p u_S}{\Delta l} + \frac{k_{eff}}{2\Delta r_s^{\,2}}\right)T_s^{\,i,n+1} = \left(\frac{\rho_S C_p u_S}{\Delta l}\right)T_s^{\,i-1,n+1}$$

$$+ \rho_B\left(-rA\right)\left(-\Delta H\right)$$

$$\left(ASB2\right)T_s^{\,i,n-1} + \left(BSB2\right)T_s^{\,i,n+1} = \left(CSB2\right)T_s^{\,i-1,n+1} + RXN$$

REFERENCES

1. Biloen, P., F.M. Dautzenberg, and W.M.H. Sachtler, *Catalytic Dehydrogenation of Propane to Propene over Platinum and Platinum-Gold Alloys*. Journal of Catalysis, 1977. **50**(1): p. 77-86.

2. Suzuki, I. and Y. Kaneko, *Dehydrogenation of Propane over Chromia-Alumina Potassium Oxide Catalyst*. Journal of Catalysis, 1977. **47**(2): p. 239-248.

3. Derossi, S., et al., *Propane Dehydrogenation on Chromia Silica and Chromia Alumina Catalysts*. Journal of Catalysis, 1994. **148**(1): p. 36-46.

4. Barias, O.A., A. Holmen, and E.A. Blekkan, *Propane dehydrogenation over supported Pt and Pt-Sn catalysts: Catalyst preparation, characterization, and activity measurements*. Journal of Catalysis, 1996. **158**(1): p. 1-12.

5. Annaland, T.V., J.A.M. Kuipers, and W.P.M. van Swaaij, *A kinetic rate expression for the time-dependent coke formation rate during propane dehydrogenation over a platinum alumina monolithic catalyst*. Catalysis Today, 2001. **66**(2-4): p. 427-436.

6. Weckhuysen, B.M. and R.A. Schoonheydt, *Alkane dehydrogenation over supported chromium oxide catalysts*. Catalysis Today, 1999. **51**(2): p. 223-232.

7. Gascon, J., et al., *Propane dehydrogenation over a Cr2O3/Al2O3 catalyst: transient kinetic modeling of propene and coke formation*. Applied Catalysis a-General, 2003. **248**(1-2): p. 105-116.

8. Kumar, M.S., et al., *The nature of active chromium species in Cr-catalysts for dehydrogenation of propane: New insights by a comprehensive spectroscopic study*. Journal of Catalysis, 2009. **261**(1): p. 116-128.

9. Iglesias-Juez, A., et al., *A combined in situ time-resolved UV-Vis, Raman and high-energy resolution X-ray absorption spectroscopy study on the deactivation behavior of Pt and Pt-Sn propane dehydrogenation catalysts under industrial reaction conditions*. Journal of Catalysis, 2010. **276**(2): p. 268-279.

10. Baek, J., et al., *Preparation of Highly Dispersed Chromium Oxide Catalysts Supported on Mesoporous Silica for the Oxidative Dehydrogenation of Propane Using CO2: Insight into the Nature of Catalytically Active Chromium Sites*. Acs Catalysis, 2012. **2**(9): p. 1893-1903.

11. Wu, R.X., et al., *Hydrothermally prepared Cr2O3-ZrO2 as a novel efficient catalyst for dehydrogenation of propane with CO2*. Catalysis Communications, 2013. **39**: p. 20-23.

12. Jablonski, E.L., et al., *Effect of Ga addition to Pt/Al2O3 on the activity, selectivity and deactivation in the propane dehydrogenation*. Applied Catalysis a-General, 1999. **183**(1): p. 189-198.

13. Bhasin, M.M., et al., *Dehydrogenation and oxydehydrogenation of paraffins to*

olefins. Applied Catalysis a-General, 2001. **221**(1-2): p. 397-419.

14. Zhang, Y.W., et al., *Propane dehydrogenation on PtSn/ZSM-5 catalyst: Effect of tin as a promoter*. Catalysis Communications, 2006. **7**(11): p. 860-866.

15. Lobera, M.P., et al., *Transient kinetic modelling of propane dehydrogenation over a Pt-Sn-K/Al2O3 catalyst*. Applied Catalysis a-General, 2008. **349**(1-2): p. 156-164.

16. Li, Q., et al., *Coke Formation on Pt-Sn/Al2O3 Catalyst in Propane Dehydrogenation: Coke Characterization and Kinetic Study*. Topics in Catalysis, 2011. **54**(13-15): p. 888-896.

17. Sun, P.P., et al., *Novel Pt/Mg(In)(Al)O catalysts for ethane and propane dehydrogenation*. Journal of Catalysis, 2011. **282**(1): p. 165-174.

18. Vora, B.V., *Development of Dehydrogenation Catalysts and Processes*. Topics in Catalysis, 2012. **55**(19-20): p. 1297-1308.

19. Tan, S., et al., *Catalytic propane dehydrogenation over In2O3-Ga2O3 mixed oxides*. Applied Catalysis a-General, 2015. **498**: p. 167-175.

20. Sattler, J.J.H.B., et al., *Catalytic Dehydrogenation of Light Alkanes on Metals and Metal Oxides*. Chemical Reviews, 2014. **114**(20): p. 10613-10653.

21. Li, Q., et al., *Kinetics of propane dehydrogenation over Pt-Sn/Al(2)O(3) catalyst*. Applied Catalysis a-General, 2011. **398**(1-2): p. 18-26.

22. Alcantara-Avila, J.R., et al., *Optimal design of cryogenic distillation columns with side heat pumps for the propylene/propane separation*. Chemical Engineering and Processing, 2014. **82**: p. 112-122.

23. van Miltenburg, A., et al., *Adsorptive separation of light olefin/paraffin mixtures*. Chemical Engineering Research & Design, 2006. **84**(A5): p. 350-354.

24. Liao, B., et al., *New process for separating propylene and propane by extractive distillation with aqueous acetonitrile*. Chemical Engineering Journal, 2001. **84**(3): p. 581-586.

25. Sirkar, K.K., P.V. Shanbhag, and A.S. Kovvali, *Membrane in a reactor: A functional perspective*. Industrial & Engineering Chemistry Research, 1999. **38**(10): p. 3715-3737.

26. Coronas, J. and J. Santamaria, *State-of-the-art in zeolite membrane reactors*. Topics in Catalysis, 2004. **29**(1-2): p. 29-44.

27. McLeary, E.E., J.C. Jansen, and F. Kapteijn, *Zeolite based films, membranes and membrane reactors: Progress and prospects*. Microporous and Mesoporous Materials, 2006. **90**(1-3): p. 198-220.

28. Vital, J., et al., *The effect of alpha-terpineol on the hydration of alpha-pinene over zeolites dispersed in polymeric membranes*. Catalysis Today, 2001. **67**(1-3): p. 217-223.

29. Brinkmann, T., S.P. Perera, and W.J. Thomas, *An experimental and theoretical investigation of a catalytic membrane reactor for the oxidative dehydrogenation of methanol*. Chemical Engineering Science, 2001. **56**(6): p. 2047-2061.

30. Bottino, A., G. Capannelli, and A. Comite, *Catalytic membrane reactors for the oxidehydrogenation of propane: experimental and modelling study*. Journal of Membrane Science, 2002. **197**(1-2): p. 75-88.

31. Tsuru, T., et al., *Membrane reactor performance of steam reforming of methane using hydrogen-permselective catalytic SiO2 membranes*. Journal of Membrane Science, 2008. **316**(1-2): p. 53-62.

32. Fong, Y.Y., et al., *Development of functionalized zeolite membrane and its potential role as reactor combined separator for para-xylene production from xylene isomers*. Chemical Engineering Journal, 2008. **139**(1): p. 172-193.

33. Tuan, V.A., et al., *In situ crystallization of beta zeolite membranes and their permeation and separation properties*. Chemistry of Materials, 2002. **14**(2): p. 489-492.

34. Diakov, V. and A. Varma, *Reactant distribution by inert membrane enhances packed-bed reactor stability*. Chemical Engineering Science, 2002. **57**(7): p. 1099-1105.

35. Kim, S.J., et al., *Zeolite Membrane Reactor for High-Temperature Water-Gas Shift Reaction: Effects of Membrane Properties and Operating Conditions*. Energy & Fuels, 2013. **27**(8): p. 4471-4480.

36. Kim, S.J., et al., *Effect of Pressure on High-Temperature Water Gas Shift Reaction in Microporous Zeolite Membrane Reactor*. Industrial & Engineering Chemistry Research, 2012. **51**(3): p. 1364-1375.

37. Tang, Z., et al., *Modified zeolite membrane reactor for high temperature water gas shift reaction*. Journal of Membrane Science, 2010. **354**(1-2): p. 114-122.

38. Zhang, Y.T., et al., *Hydrogen-selective zeolite membrane reactor for low temperature water gas shift reaction*. Chemical Engineering Journal, 2012. **197**: p. 314-321.

39. Galuszka, J., T. Giddings, and G. Iaquaniello, *Membrane assisted WGSR - Experimental study and reactor modeling*. Chemical Engineering Journal, 2012. **213**: p. 363-370.

40. Chein, R.Y., Y.C. Chen, and J.N. Chung, *Sweep gas flow effect on membrane reactor performance for hydrogen production from high-temperature water-gas shift reaction*. Journal of Membrane Science, 2015. **475**: p. 193-203.

41. Champagnie, A.M., et al., *A High-Temperature Catalytic Membrane Reactor for Ethane Dehydrogenation*. Chemical Engineering Science, 1990. **45**(8): p. 2423-2429.

42. Gobina, E. and R. Hughes, *Ethane Dehydrogenation Using a High-Temperature*

Catalytic Membrane Reactor. Journal of Membrane Science, 1994. **90**(1-2): p. 11-19.

43. Gobina, E., K. Hou, and R. Hughes, *Ethane Dehydrogenation in a Catalytic Membrane Reactor Coupled with a Reactive Sweep Gas*. Chemical Engineering Science, 1995. **50**(14): p. 2311-2319.

44. van den Bergh, J., et al., *Isobutane dehydrogenation in a DD3R zeolite membrane reactor*. Chemical Engineering Journal, 2011. **166**(1): p. 368-377.

45. Kong, C.L., et al., *Catalytic dehydrogenation of ethylbenzene to styrene in a zeolite silicalite-1 membrane reactor*. Journal of Membrane Science, 2007. **306**(1-2): p. 29-35.

46. Wieland, S., T. Melin, and A. Lamm, *Membrane reactors for hydrogen production*. Chemical Engineering Science, 2002. **57**(9): p. 1571-1576.

47. Yu, W., et al., *Optimal design and operation of methane steam reforming in a porous ceramic membrane reactor for hydrogen production*. Chemical Engineering Science, 2007. **62**(18-20): p. 5627-5631.

48. Bernardo, P., G. Barbieri, and E. Drioli, *Evaluation of membrane reactor with hydrogen-selective membrane in methane steam reforming*. Chemical Engineering Science, 2010. **65**(3): p. 1159-1166.

49. Caravella, A., F.P. Di Maio, and A. Di Renzo, *Computational Study of Staged Membrane Reactor Configurations for Methane Steam Reforming. I. Optimization of Stage Lengths*. Aiche Journal, 2010. **56**(1): p. 248-258.

50. Saric, M., et al., *Steam reforming of methane in a bench-scale membrane reactor at realistic working conditions*. Catalysis Today, 2012. **193**(1): p. 74-80.

51. Di Marcoberardino, G., et al., *Fixed bed membrane reactor for hydrogen production from steam methane reforming: Experimental and modeling approach*. International Journal of Hydrogen Energy, 2015. **40**(24): p. 7559-7567.

52. Patrascu, M. and M. Sheintuch, *On-site pure hydrogen production by methane steam reforming in high flux membrane reactor: Experimental validation, model predictions and membrane inhibition*. Chemical Engineering Journal, 2015. **262**: p. 862-874.

53. Ziaka, Z.D., R.G. Minet, and T.T. Tsotsis, *Propane Dehydrogenation in a Packed-Bed Membrane Reactor*. Aiche Journal, 1993. **39**(3): p. 526-529.

54. Ziaka, Z.D., R.G. Minet, and T.T. Tsotsis, *A High-Temperature Catalytic Membrane Reactor for Propane Dehydrogenation*. Journal of Membrane Science, 1993. **77**(2-3): p. 221-232.

55. Collins, J.P., et al., *Catalytic dehydrogenation of propane in hydrogen permselective membrane reactors*. Industrial & Engineering Chemistry Research, 1996. **35**(12): p. 4398-4405.

56. Weyten, H., et al., *Dehydrogenation of propane using a packed-bed catalytic membrane reactor*. Aiche Journal, 1997. **43**(7): p. 1819-1827.

57. Weyten, H., et al., *Membrane performance: the key issues for dehydrogenation reactions in a catalytic membrane reactor*. Catalysis Today, 2000. **56**(1-3): p. 3-11.

58. Kotanjac, Z.S., M.V. Annaland, and J.A.M. Kuipers, *Demonstration of a packed bed membrane reactor for the oxidative dehydrogenation of propane*. Chemical Engineering Science, 2010. **65**(22): p. 6029-6035.

59. Teixeira, M., et al., *Improving propyne removal from propylene streams using a catalytic membrane reactor-a theoretical study*. Journal of Membrane Science, 2011. **375**(1-2): p. 124-133.

60. Shelepova, E.V., et al., *Mathematical modeling of the propane dehydrogenation process in the catalytic membrane reactor*. Chemical Engineering Journal, 2011. **176**: p. 151-157.

61. Didenko, L.P., et al., *Dehydrogenation of propane in a combined membrane reactor with hydrogen-permeable palladium module*. Petroleum Chemistry, 2013. **53**(1): p. 27-32.

62. Choi, S.W., et al., *Material Properties and Operating Configurations of Membrane Reactors for Propane Dehydrogenation*. Aiche Journal, 2015. **61**(3): p. 922-935.

63. Wu, J.C.S. and P.K.T. Liu, *Mathematical-Analysis on Catalytic Dehydrogenation of Ethylbenzene Using Ceramic Membranes*. Industrial & Engineering Chemistry Research, 1992. **31**(1): p. 322-327.

64. Kumar, S., T. Gaba, and S. Kumar, *Simulation of Catalytic Dehydrogenation of Cyclohexane in Zeolite Membrane Reactor*. International Journal of Chemical Reactor Engineering, 2009. **7**.

65. Harold, M.P., et al., *Catalysis with Inorganic Membranes*. Mrs Bulletin, 1994. **19**(4): p. 34-39.

66. Gokhale, Y.V., R.D. Noble, and J.L. Falconer, *Effects of Reactant Loss and Membrane Selectivity on a Dehydrogenation Reaction in a Membrane-Enclosed Catalytic Reactor*. Journal of Membrane Science, 1995. **103**(3): p. 235-242.

67. Tsai, C.Y., et al., *Modeling and simulation of a nonisothermal catalytic membrane reactor*. Chemical Engineering Communications, 1995. **134**: p. 107-132.

68. Shelepova, E.V., A.A. Vedyagin, and A.S. Noskov, *Effect of Catalytic Combustion of Hydrogen on the Dehydrogenation Processes in a Membrane Reactor. I. Mathematical Model of the Process*. Combustion Explosion and Shock Waves, 2011. **47**(5): p. 499-507.

69. Gobina, E., K. Hou, and R. Hughes, *Equilibrium-Shift in Alkane Dehydrogenation Using a High-Temperature Catalytic Membrane Reactor*. Catalysis Today, 1995. **25**(3-4): p. 365-370.

70. Koukou, M.K., N. Papayannakos, and N.C. Markatos, *Dispersion effects on membrane reactor performance*. Aiche Journal, 1996. **42**(9): p. 2607-2615.

71. Casanave, D., et al., *Zeolite membrane reactor for isobutane dehydrogenation: Experimental results and theoretical modelling*. Chemical Engineering Science, 1999. **54**(13-14): p. 2807-2815.

72. Ciavarella, P., et al., *Isobutane dehydrogenation in a membrane reactor - Influence of the operating conditions on the performance*. Catalysis Today, 2001. **67**(1-3): p. 177-184.

73. Gallucci, F., et al., *Co-current and counter-current configurations for ethanol steam reforming in a dense Pd-Ag membrane reactor*. International Journal of Hydrogen Energy, 2008. **33**(21): p. 6165-6171.

74. Staudt-Bickel, C. and W.J. Koros, *Olefin/paraffin gas separations with 6FDA-based polyimide membranes*. Journal of Membrane Science, 2000. **170**(2): p. 205-214.

75. Krol, J.J., M. Boerrigter, and G.H. Koops, *Polyimide hollow fiber gas separation membranes: preparation and the suppression of plasticization in propane/propylene environments*. Journal of Membrane Science, 2001. **184**(2): p. 275-286.

76. Bai, S., S. Sridhar, and A.A. Khan, *Recovery of propylene from refinery off-gas using metal incorporated ethylcellulose membranes*. Journal of Membrane Science, 2000. **174**(1): p. 67-79.

77. Gallucci, F., A. Basile, and F.I. Hai, *Introduction - A Review of Membrane Reactors*. Membranes for Membrane Reactors: Preparation, Optimization and Selection, ed. F. Gallucci and A. Basile. 2011: John Wiley & Sons, Ltd.

78. Prabhu, A.K. and S.T. Oyama, *Development of a hydrogen selective ceramic membrane and its application for the conversion of greenhouse gases*. Chemistry Letters, 1999(3): p. 213-214.

79. Stoitsas, K.A., et al., *Porous ceramic membranes for propane-propylene separation via the pi-complexation mechanism: unsupported systems*. Microporous and Mesoporous Materials, 2005. **78**(2-3): p. 235-243.

80. Tsuru, T., et al., *Permeation Properties of Hydrogen and Water Vapor Through Porous Silica Membranes at High Temperatures*. Aiche Journal, 2011. **57**(3): p. 618-629.

81. Khatib, S.J. and S.T. Oyama, *Silica membranes for hydrogen separation prepared by chemical vapor deposition (CVD)*. Separation and Purification Technology, 2013. **111**: p. 20-42.

82. Gallucci, F., et al., *Recent advances on membranes and membrane reactors for hydrogen production*. Chemical Engineering Science, 2013. **92**: p. 40-66.

83. Kikuchi, E., *Palladium/Ceramic Membranes for Selective Hydrogen Permeation*

and Their Application to Membrane Reactor. Catalysis Today, 1995. **25**(3-4): p. 333-337.

84. Violante, V., E. Drioli, and A. Basile, *Catalytic Ceramic Membrane Reactor Design for Hydrogen Separation from Inert-Gas Via Oxidation*. Journal of Membrane Science, 1995. **104**(1-2): p. 11-17.

85. McCool, B., G. Xomeritakis, and Y.S. Lin, *Composition control and hydrogen permeation characteristics of sputter deposited palladium-silver membranes*. Journal of Membrane Science, 1999. **161**(1-2): p. 67-76.

86. Giannakopoulos, I.G. and V. Nikolakis, *Separation of propylene/propane mixtures using faujasite-type zeolite membranes*. Industrial & Engineering Chemistry Research, 2005. **44**(1): p. 226-230.

87. Granato, M.A., et al., *Diffusion of propane, propylene and isobutane in 13X zeolite by molecular dynamics*. Chemical Engineering Science, 2010. **65**(9): p. 2656-2663.

88. Grande, C.A., et al., *Propane/propylene separation with Li-exchanged zeolite 13X*. Chemical Engineering Journal, 2010. **160**(1): p. 207-214.

89. Gutierrez-Sevillano, J.J., et al., *Analysis of the ITQ-12 Zeolite Performance in Propane-Propylene Separations Using a Combination of Experiments and Molecular Simulations*. Journal of Physical Chemistry C, 2010. **114**(35): p. 14907-14914.

90. Nair, S. and M. Tsapatsis, *Synthesis and Properties of Zeolitic Membranes*. Handbook of Zeolite Science and Technology, ed. S.M. Auerbach, K.A. Carrado, and P.K. Dutta. 2003, New York: Marcel Dekker, Inc.

91. Chu, C.T.W. and C.D. Chang, *Isomorphous Substitution in Zeolite Frameworks .1. Acidity of Surface Hydroxyls in [B]-Zsm-5, [Fe]-Zsm-5, [Ga]-Zsm-5, and [Al]-Zsm-5*. Journal of Physical Chemistry, 1985. **89**(9): p. 1569-1571.

92. Simmons, D.K., et al., *Gallosilicate Molecular-Sieves - the Role of Framework and Nonframework Gallium on Catalytic Cracking Activity*. Journal of Catalysis, 1987. **106**(1): p. 287-291.

93. Halasz, J., et al., *Indium and gallium containing ZSM-5 zeolites: Acidity and catalytic activity in propane transformation*. Catalysis Today, 1996. **31**(3-4): p. 293-304.

94. Hong, M., et al., *Ion-exchanged SAPO-34 membranes for light gas separations*. Microporous and Mesoporous Materials, 2007. **106**(1-3): p. 140-146.

95. Hong, M., et al., *Hydrogen purification using a SAPO-34 membrane*. Journal of Membrane Science, 2008. **307**(2): p. 277-283.

96. Agarwal, K., et al., *SAPO-34 assisted C3 separation: Modeling and simulation*. Microporous and Mesoporous Materials, 2010. **132**(3): p. 311-318.

97. van den Bergh, J., A. Tihaya, and F. Kapteijn, *High temperature permeation and separation characteristics of an all-silica DDR zeolite membrane*. Microporous and Mesoporous Materials, 2010. **132**(1-2): p. 137-147.

98. Gascon, J., et al., *Accelerated synthesis of all-silica DD3R and its performance in the separation of propylene/propane mixtures*. Microporous and Mesoporous Materials, 2008. **115**(3): p. 585-593.

99. Zhu, W., et al., *Shape selectivity in adsorption on the all-silica DD3R*. Langmuir, 2000. **16**(7): p. 3322-3329.

100. van den Bergh, J., et al., *Separation and permeation characteristics of a DD3R zeolite membrane*. Journal of Membrane Science, 2008. **316**(1-2): p. 35-45.

101. Zhu, W., F. Kapteijn, and J.A. Moulijn, *Shape selectivity in the adsorption of propane/propene on the all-silica DD3R*. Chemical Communications, 1999(24): p. 2453-2454.

102. Baerlocher, C. and L.B. McCusker. *Database of Zeolite Structures: http://www.iza-structure.org/databases/*.

103. Krishna, R. and J.A. Wesselingh, *Review article number 50 - The Maxwell-Stefan approach to mass transfer*. Chemical Engineering Science, 1997. **52**(6): p. 861-911.

104. Rao, M.B. and S. Sircar, *Nanoporous Carbon Membranes for Separation of Gas-Mixtures by Selective Surface Flow*. Journal of Membrane Science, 1993. **85**(3): p. 253-264.

105. Jeong, B.H., K.I. Sotowa, and K. Kusakabe, *Modeling of an FAU-type zeolite membrane reactor for the catalytic dehydrogenation of cyclohexane*. Chemical Engineering Journal, 2004. **103**(1-3): p. 69-75.

106. Krishna, R., *Multicomponent Surface-Diffusion of Adsorbed Species - a Description Based on the Generalized Maxwell-Stefan Equations*. Chemical Engineering Science, 1990. **45**(7): p. 1779-1791.

107. Kapteijn, F., et al., *Permeation and Separation Behavior of a Silicalite-1 Membrane*. Catalysis Today, 1995. **25**(3-4): p. 213-218.

108. Kapteijn, F., et al., *Permeation and Separation of Light-Hydrocarbons through a Silicalite-1 Membrane - Application of the Generalized Maxwell-Stefan Equations*. Chemical Engineering Journal and the Biochemical Engineering Journal, 1995. **57**(2): p. 145-153.

109. Krishna, R. and L.J.P. Vandenbroeke, *The Maxwell-Stefan Description of Mass-Transport across Zeolite Membranes*. Chemical Engineering Journal and the Biochemical Engineering Journal, 1995. **57**(2): p. 155-162.

110. Bakker, W.J.W., et al., *Temperature dependence of one-component permeation through a silicalite-1 membrane*. Aiche Journal, 1997. **43**(9): p. 2203-2214.

111. van de Graaf, J.M., F. Kapteijn, and J.A. Moulijn, *Modeling permeation of binary mixtures through zeolite membranes*. Aiche Journal, 1999. **45**(3): p. 497-511.

112. Kapteijn, F., Bakker, W.J.W., Zheng, G., and Moulijn, J.A., *Temperature and occupancydependent diffusion of n-butane through a silicalite-1 membrane*. microporous Materials, 1994. **3**: p. 227-234.

113. Bakker, W.J.W., et al., *Permeation characteristics of a metal-supported silicalite-1 zeolite membrane*. Journal of Membrane Science, 1996. **117**(1-2): p. 57-78.

114. Zhang, Y.W., et al., *Effect of alumina binder on catalytic performance of PtSnNa/ZSM-5 catalyst for propane dehydrogenation*. Industrial & Engineering Chemistry Research, 2006. **45**(7): p. 2213-2219.

115. Larsson, M., et al., *The effect of reaction conditions and time on stream on the coke formed during propane dehydrogenation*. Journal of Catalysis, 1996. **164**(1): p. 44-53.

116. Rebo, H.P., et al., *Application of the oscillating microbalance catalytic reactor: Kinetics and coke formation over Pt-Sn/Al2O3 in propane dehydrogenation*. Natural Gas Conversion V, 1998. **119**: p. 617-622.

117. Praserthdam, P., et al., *Determination of coke deposition on metal active sites of propane dehydrogenation catalysts*. Catalyst Deactivation 1997, 1997. **111**: p. 153-158.

118. Chen, M., et al., *Study in support effect of In2O3/MOx (M = Al, Si, Zr) catalysts for dehydrogenation of propane in the presence of CO2*. Applied Catalysis a-General, 2011. **407**(1-2): p. 20-28.

119. Tan, S., et al., *Propane Dehydrogenation over In2O3-Ga2O3-Al2O3 Mixed Oxides*. Chemcatchem, 2016. **8**(1): p. 214-221.

120. Gascon, J., et al., *Corrigendum to "Propane dehydrogenation over a Cr2O3/Al2O3 catcalyst: transient kinetic modeling of propene and coke formation" (vol 248, pg 105, 2003)*. Applied Catalysis a-General, 2005. **282**(1-2): p. 343-343.

121. Wan, B.Z. and H.M. Chu, *Reaction-Kinetics of Propane Dehydrogenation over Partially Reduced Zinc-Oxide Supported on Silicalite*. Journal of the Chemical Society-Faraday Transactions, 1992. **88**(19): p. 2943-2947.

122. Mowry, J.R., R.F. Anderson, and J.A. Johnson, *Process Makes Aromatics from Lpg*. Oil & Gas Journal, 1985. **83**(48): p. 128-131.

123. Imai, T., J.A. Kocal, and C.D. Gosling, *The Uop-Bp Cyclar Process*. Catalytic Science and Technology, Vol 1, 1991. **1**: p. 399-402.

124. Giannetto, G., R. Monque, and R. Galiasso, *Transformation of Lpg into Aromatic-Hydrocarbons and Hydrogen over Zeolite Catalysts*. Catalysis Reviews-Science and Engineering, 1994. **36**(2): p. 271-304.

125. Meriaudeau, P. and C. Naccache, *Dehydrocyclization of alkanes over zeolite-supported metal catalysts: Monofunctional or bifunctional route*. Catalysis Reviews-Science and Engineering, 1997. **39**(1-2): p. 5-48.

126. Fricke, R., et al., *Incorporation of gallium into zeolites: Syntheses, properties and catalytic application*. Chemical Reviews, 2000. **100**(6): p. 2303-2405.

127. Bhan, A. and W.N. Delgass, *Propane aromatization over HZSM-5 and Ga/HZSM-5 catalysts*. Catalysis Reviews-Science and Engineering, 2008. **50**(1): p. 19-151.

128. Rodrigues, V.D. and A.C. Faro, *On catalyst activation and reaction mechanisms in propane aromatization on Ga/HZSM5 catalysts*. Applied Catalysis a-General, 2012. **435**: p. 68-77.

129. Meriaudeau, P. and C. Naccache, *The Role of Ga2o3 and Proton Acidity on the Dehydrogenating Activity of Ga2o3-Hzsm-5 Catalysts - Evidence of a Bifunctional Mechanism*. Journal of Molecular Catalysis, 1990. **59**(3): p. L31-L36.

130. Bayense, C.R. and J.H.C. Vanhooff, *Aromatization of Propane over Gallium-Containing H-Zsm-5 Zeolites - Influence of the Preparation Method on the Product Selectivity and the Catalytic Stability*. Applied Catalysis, 1991. **79**(1): p. 127-140.

131. Buckles, G., G.J. Hutchings, and C.D. Williams, *Propane Conversion over Zeolite Catalysts - Comments on the Role of Ga*. Catalysis Letters, 1991. **8**(2-4): p. 115-124.

132. Meriaudeau, P. and C. Naccache, *H-Zsm-5 Supported Ga2o3 Dehydrocyclization Catalysts - Infrared Spectroscopic Evidence of Gallium Oxide Surface Mobility*. Applied Catalysis, 1991. **73**(1): p. L13-L18.

133. Meriaudeau, P., S.B.A. Hamid, and C. Naccache, *Propane Conversion on Ga-Hzsm-5 - Effect of Aging on the Dehydrogenating and Acid Functions Using Pyridine as an Ir Probe*. Journal of Catalysis, 1993. **139**(2): p. 679-682.

134. Meriaudeau, P. and C. Naccache, *Transformation of Propane over Ga/Hzsm-5 Catalyst - on the Nature of the Active-Sites for the Dehydrogenation Reaction*. Studies in Surface Science and Catalysis, 1993. **75**: p. 2431-2434.

135. Sun, Y.P. and T.C. Brown, *Catalytic cracking, dehydrogenation, and aromatization of isobutane over Ga/HZSM-5 and Zn/HZSM-5 at low pressures*. International Journal of Chemical Kinetics, 2002. **34**(8): p. 467-480.

136. Xu, B.J., et al., *Enhanced stability of HZSM-5 supported Ga2O3 catalyst in propane dehydrogenation by dealumination*. Catalysis Letters, 2007. **119**(3-4): p. 283-288.

137. Rodrigues, V.D., J.G. Eon, and A.C. Faro, *Correlations between Dispersion, Acidity, Reducibility, and Propane Aromatization Activity of Gallium Species Supported on HZSM5 Zeolites*. Journal of Physical Chemistry C, 2010. **114**(10): p. 4557-4567.

138. Inui, T., et al., *Selective Conversion of Propane into Aromatics on Platinum Ion-Exchanged Gallium-Silicate Bifunctional Catalysts*. Journal of the Chemical Society-Chemical Communications, 1986(7): p. 571-573.

139. Choudhary, V.R., et al., *H.Na-Gallosilicate (MFI) propane aromatization catalyst: Influence of H+ exchange on acidity, activity, and deactivation due to coking*. Zeolites, 1997. **18**(2-3): p. 188-195.

140. Choudhary, V.R., et al., *H-gallosilicate (MFI) propane aromatization catalyst: Influence of Si/Ga ratio on acidity, activity and deactivation due to coking*. Journal of Catalysis, 1996. **158**(1): p. 34-50.

141. Khodakov, A.Y., et al., *Investigation of the Different States of Gallium in Crystalline Gallosilicates with Pentasil Structure and Their Role in Propane Aromatization*. Zeolites, 1990. **10**(6): p. 603-607.

142. Giannetto, G., et al., *Conversion of Light Alkanes into Aromatic-Hydrocarbons .7. Aromatization of Propane on Gallosilicates - Effect of Calcination in Dry Air*. Journal of Catalysis, 1994. **145**(1): p. 86-95.

143. Choudhary, V.R., et al., *Acidity, catalytic activity, and deactivation of H-gallosilicate (MFI) in propane aromatization: Influence of hydrothermal pretreatments*. Journal of Catalysis, 1996. **158**(2): p. 537-550.

144. Choudhary, V.R., et al., *H-gallosilicate (MFI) propane aromatization catalyst - Influence of calcination temperature on acidity, activity and deactivation due to coking*. Applied Catalysis a-General, 1996. **136**(2): p. 125-142.

145. Meriaudeau, P., G. Sapaly, and C. Naccache, *Framework and Nonframework Gallium in Pentasil-Like Zeolite as Studied in the Reaction of Propane*. Journal of Molecular Catalysis, 1993. **81**(2): p. 293-300.

146. Bigey, C. and B.L. Su, *Propane as alkylating agent for alkylation of benzene on HZSM-5 and Ga-modified HZSM-5 zeolites*. Journal of Molecular Catalysis a-Chemical, 2004. **209**(1-2): p. 179-187.

147. Al-majnouni, K.A., et al., *High-Temperature Decomposition of Bronsted Acid Sites in Gallium-Substituted Zeolites*. Journal of Physical Chemistry C, 2010. **114**(45): p. 19395-19405.

148. Al-Yassir, N., M.N. Akhtar, and S. Al-Khattaf, *Physicochemical properties and catalytic performance of galloaluminosilicate in aromatization of lower alkanes: a comparative study with Ga/HZSM-5*. Journal of Porous Materials, 2012. **19**(6): p. 943-960.

149. Kwak, B.S. and W.M.H. Sachtler, *Effect of Ga/Proton Balance in Ga/Hzsm-5 Catalysts on C-3 Conversion to Aromatics*. Journal of Catalysis, 1994. **145**(2): p. 456-463.

150. Miyamoto, T., et al., *Acidic property of MFI-type gallosilicate determined by temperature-programmed desorption of ammonia*. Journal of Physical Chemistry B, 1998. **102**(35): p. 6738-6745.

151. Arean, C.O., et al., *Characterization of gallosilicate MFI-type zeolites by IR spectroscopy of adsorbed probe molecules*. Journal of Physical Chemistry, 1996. **100**(16): p. 6678-6690.

152. Krishnamurthy, G., A. Bhan, and W.N. Delgass, *Identity and chemical function of gallium species inferred from microkinetic modeling studies of propane aromatization over Ga/HZSM-5 catalysts*. Journal of Catalysis, 2010. **271**(2): p. 370-385.

153. Meriaudeau, P. and C. Naccache, *Gallium based MFI zeolites for the aromatization of propane*. Catalysis Today, 1996. **31**(3-4): p. 265-273.

154. Rahimi, N. and R. Karimzadeh, *Catalytic cracking of hydrocarbons over modified ZSM-5 zeolites to produce light olefins: A review*. Applied Catalysis a-General, 2011. **398**(1-2): p. 1-17.

155. Bayense, C.R., A.J.H.P. Vanderpol, and J.H.C. Vanhooff, *Aromatization of Propane over Mfi-Gallosilicates*. Applied Catalysis, 1991. **72**(1): p. 81-98.

156. Guisnet, M. and N.S. Gnep, *Aromatization of propane over GaHMFI catalysts. Reaction scheme, nature of the dehydrogenating species and mode of coke formation*. Catalysis Today, 1996. **31**(3-4): p. 275-292.

157. Nishi, K., et al., *Structure and catalytic properties of Ga-MFI in propane aromatization*. Applied Catalysis a-General, 2002. **223**(1-2): p. 187-193.

158. Vandamme, P.S., S. Narayanan, and G.F. Froment, *Thermal Cracking of Propane and Propane-Propylene Mixtures - Pilot-Plant Versus Industrial Data*. Aiche Journal, 1975. **21**(6): p. 1065-1073.

159. Sundaram, K.M. and G.F. Froment, *Modeling of Thermal-Cracking Kinetics .1. Thermal-Cracking of Ethane, Propane and Their Mixtures*. Chemical Engineering Science, 1977. **32**(6): p. 601-608.

160. Rosenbrock, H.H., *Some General Implicit Processes for Numerical-Solution of Differential-Equations*. Computer Journal, 1963. **6**(4): p. 329-&.

161. Moon, W.S. and S.B. Park, *Design guide of a membrane for a membrane reactor in terms of permeability and selectivity*. Journal of Membrane Science, 2000. **170**(1): p. 43-51.

162. Zehner, P. and Schlunde.Eu, *Influence of Thermal-Radiation and of Pressure on Heat-Transfer in Packings through Which No Fluid Is Flowing*. Chemie Ingenieur Technik, 1972. **44**(23): p. 1303-&.

163. Zehner, P. and Schlunde.Eu, *Heat-Conductivity of Perfused Sphere Fills at High-Temperatures*. Chemie Ingenieur Technik, 1972. **44**(15): p. 950-&.

164. Dong, J.H., Y.S. Lin, and W. Liu, *Multicomponent hydrogen/hydrocarbon separation by MFI-type zeolite membranes*. Aiche Journal, 2000. **46**(10): p. 1957-1966.

165. Kanezashi, M. and Y.S. Lin, *Gas Permeation and Diffusion Characteristics of MFI-Type Zeolite Membranes at High Temperatures*. Journal of Physical Chemistry C, 2009. **113**(9): p. 3767-3774.

166. Kanezashi, M., et al., *Gas permeation through DDR-type zeolite membranes at high temperatures*. Aiche Journal, 2008. **54**(6): p. 1478-1486.

167. Gascon, J., et al., *Practical Approach to Zeolitic Membranes and Coatings: State of the Art, Opportunities, Barriers, and Future Perspectives*. Chemistry of Materials, 2012. **24**(15): p. 2829-2844.

168. Kim, W.G. and S. Nair, *Membranes from nanoporous 1D and 2D materials: A review of opportunities, developments, and challenges*. Chemical Engineering Science, 2013. **104**: p. 908-924.

169. Harold, M.P. and C. Lee, *Intermediate product yield enhancement with a catalytic inorganic membrane .2. Nonisothermal and integral operation in a back-mixed reactor*. Chemical Engineering Science, 1997. **52**(12): p. 1923-1939.

170. Chan, P.P.Y., et al., *Modeling and simulation of non-isothermal catalytic packed bed membrane reactor for H2S decomposition*. Catalysis Today, 2000. **63**(2-4): p. 379-385.

171. Daramola, M.O., A.J. Burger, and A. Giroir-Fendler, *Modelling and sensitivity analysis of a nanocomposite MFI-alumina based extractor-type zeolite catalytic membrane reactor for m-Xylene isomerization over Pt-HZSM-5 catalyst*. Chemical Engineering Journal, 2011. **171**(2): p. 618-627.

172. Gobina, E., K. Hou, and R. Hughes, *Mathematical-Analysis of Ethylbenzene Dehydrogenation - Comparison of Microporous and Dense Membrane Systems*. Journal of Membrane Science, 1995. **105**(3): p. 163-176.

173. Shelepova, E.V., et al., *Mathematical modeling of the propane dehydrogenation process in the catalytic membrane reactor*. Chemical Engineering Journal, 2011. **176-77**: p. 151-157.

174. Zhu, J.W., et al., *A robust mixed-conducting multichannel hollow fiber membrane reactor*. Aiche Journal, 2015. **61**(8): p. 2592-2599.

175. Rahman, M.A., et al., *Development of a catalytic hollow fibre membrane micro-reactor for high purity H-2 production*. Journal of Membrane Science, 2011. **368**(1-2): p. 116-123.

176. Garcia-Garcia, F.R., et al., *Catalytic hollow fibre membrane micro-reactor: High purity H-2 production by WGS reaction*. Catalysis Today, 2011. **171**(1): p. 281-289.

177. Czuprat, O., et al., *Oxidative Coupling of Methane in a BCFZ Perovskite Hollow Fiber Membrane Reactor*. Industrial & Engineering Chemistry Research, 2010. **49**(21): p. 10230-10236.

178. Wu, Z.T., et al., *A Novel Inorganic Hollow Fiber Membrane Reactor for Catalytic*

Dehydrogenation of Propane. Aiche Journal, 2009. **55**(9): p. 2389-2398.

179. Israni, S.H., B.K.R. Nair, and M.P. Harold, *Hydrogen generation and purification in a composite Pd hollow fiber membrane reactor: Experiments and modeling*. Catalysis Today, 2009. **139**(4): p. 299-311.

180. Gimeno, M.P., et al., *Combination of a Two-Zone Fluidized Bed Reactor with a Pd hollow fibre membrane for catalytic alkane dehydrogenation*. Chemical Engineering Journal, 2009. **155**(1-2): p. 298-303.

181. Dowling, A.W., S.R.R. Vetukuri, and L.T. Biegler, *Large-scale optimization strategies for pressure swing adsorption cycle synthesis*. Aiche Journal, 2012. **58**(12): p. 3777-3791.

182. Couck, S., et al., *Adsorption and Separation of Light Gases on an Amino-Functionalized Metal-Organic Framework: An Adsorption and In Situ XRD Study*. Chemsuschem, 2012. **5**(4): p. 740-750.

183. Ribeiro, A.M., et al., *A parametric study of layered bed PSA for hydrogen purification*. Chemical Engineering Science, 2008. **63**(21): p. 5258-5273.

184. Hart, V.I., et al., *Proton-poor, gallium- and indium-loaded zeolite dehydrogenation catalysts*. Catalysis Letters, 1998. **53**(1-2): p. 111-118.

185. Goel, S., et al., *Synthesis and Catalytic Properties of Metal Clusters Encapsulated within Small-Pore (SOD, GIS, ANA) Zeolites*. Journal of the American Chemical Society, 2012. **134**(42): p. 17688-17695.

186. Wong, K.L., et al., *Subnanometer CdS Clusters Self-Confined in MFI-Type Zeolite Nanoparticles and Thin Films*. Langmuir, 2010. **26**(6): p. 4459-4464.

187. Choi, M., Z.J. Wu, and E. Iglesia, *Mercaptosilane-Assisted Synthesis of Metal Clusters within Zeolites and Catalytic Consequences of Encapsulation*. Journal of the American Chemical Society, 2010. **132**(26): p. 9129-9137.

188. Tittensor, J.G., R.J. Gorte, and D.M. Chapman, *Isopropylamine Adsorption for the Characterization of Acid Sites in Silica-Alumina Catalysts*. Journal of Catalysis, 1992. **138**(2): p. 714-720.

189. Parrillo, D.J. and R.J. Gorte, *Characterization of Acidity in H-Zsm-5, H-Zsm-12, H-Mordenite, and H-Y Using Microcalorimetry*. Journal of Physical Chemistry, 1993. **97**(34): p. 8786-8792.

190. Xu, W., et al., *Zeolite topology effects in the alkylation of phenol with propylene*. Applied Catalysis a-General, 2013. **459**: p. 114-120.

191. Kofke, T.J.G., R.J. Gorte, and G.T. Kokotailo, *Determination of Framework Concentrations of Gallium in [Ga]-Zsm-5*. Applied Catalysis, 1989. **54**(2): p. 177-188.

192. Zecchina, A., G. Spoto, and S. Bordiga, *Probing the acid sites in confined spaces of microporous materials by vibrational spectroscopy*. Physical Chemistry

Chemical Physics, 2005. **7**(8): p. 1627-1642.

193. Emeis, C.A., *Determination of Integrated Molar Extinction Coefficients for Infrared-Absorption Bands of Pyridine Adsorbed on Solid Acid Catalysts*. Journal of Catalysis, 1993. **141**(2): p. 347-354.

194. Biaglow, A.I., et al., *2-Propanamine Adsorption on a Fluid Catalytic Cracking Catalyst*. Journal of Catalysis, 1991. **129**(1): p. 88-93.

195. Ausavasukhi, A., et al., *Hydrodeoxygenation of m-cresol over gallium-modified beta zeolite catalysts*. Journal of Catalysis, 2012. **290**: p. 90-100.

196. Ausavasukhi, A., T. Sooknoi, and D.E. Resasco, *Catalytic deoxygenation of benzaldehyde over gallium-modified ZSM-5 zeolite*. Journal of Catalysis, 2009. **268**(1): p. 68-78.

197. Kosslick, H., et al., *Disruption of the Mfi Framework by the Incorporation of Gallium*. Journal of the Chemical Society-Faraday Transactions, 1993. **89**(7): p. 1131-1138.

198. Jones, C.W., K. Tsuji, and M.E. Davis, *Organic-functionalized molecular sieves as shape-selective catalysts*. Nature, 1998. **393**(6680): p. 52-54.

199. Jones, C.W., K. Tsuji, and M.E. Davis, *Organic-functionalized molecular sieves (OFMSs). II. Synthesis, characterization and the transformation of OFMSs containing non-polar functional groups into solid acids*. Microporous and Mesoporous Materials, 1999. **33**(1-3): p. 223-240.

200. Tsuji, K., C.W. Jones, and M.E. Davis, *Organic-functionalized molecular sieves (OFMSs) I. Synthesis and characterization of OFMSs with polar functional groups*. Microporous and Mesoporous Materials, 1999. **29**(3): p. 339-349.

201. Bayense, C.R., et al., *The Removal of Gallium from the Lattice of Mfi-Gallosilicates as Studied by Ga-71 Mas-Nmr Spectroscopy*. Journal of the Chemical Society-Chemical Communications, 1989(17): p. 1292-1293.

202. Bayense, C.R., et al., *Determination of Gallium in H(Ga)Zsm5 Zeolites by Ga-71 Mas Nmr-Spectroscopy*. Journal of Physical Chemistry, 1992. **96**(2): p. 775-782.

203. Takeguchi, T., et al., *Ga-71 NMR characterization of MFI-type Ga-silicate synthesized by the rapid crystallization method*. Catalysis Letters, 1997. **46**(1-2): p. 5-9.